UNIVERSITÀ
DEGLI STUDI
FIRENZE

Doctoral Programme in Industrial Engineering

Dottorato di Ricerca in Ingegneria Industriale

XXXIII

Advanced modeling and development of mathematical methods for real-time diagnosis on lithium-ion batteries and state prediction

ING/IND-14

Doctoral Candidate

Edoardo Locorotondo

Dean of the Doctoral Programme

Prof. Giampaolo Manfrida

Supervisors

Prof. Luca Pugi

Prof. Marco Pierini

Prof. Lorenzo Berzi

External referees

Prof. Davide Tarsitano

Prof. Mirko Marracci

.

Years 2017/2020

Desidero ringraziare il Dipartimento di Ingeneria Industriale dell'Università di Firenze, in particolare il gruppo Moving, per avermi accolto in questi tre anni di dottorato. Infine desidero ringraziare il Politecnico di Torino, l'Università di Pisa, il centro ricerche ENEA (Casaccia) e i partner del progetto Europeo OBELICS per la loro collaborazione, essenziale per lo sviluppo di questa tesi. Dedico questo lavoro di tesi ai miei supervisori: il professor Marco Pierini, il professor Lorenzo Berzi, e, in particolare, al mitico professor Luca Pugi.

Summary

The capability to assess and monitor the state of charge (SOC) and state of health (SOH) of lithium-based cells is a highly demanded feature for advanced battery management systems.
The main purpose of this thesis is to develop advanced models and methodologies to have a real-time diagnostic of battery state. In this regard, electrical, electrochemical, and aging characteristics have been analyzed, in order to develop accurate and low-computational cost models in the time and frequency domain.
In particular, a novel electrical lithium-based battery performance model with aging characteristics has been defined and validated through experimental tests. The virtual model developed and implemented in Simulink platform has an interesting peculiarity. Model parameters have been evaluated from experimental tests performed on several end-of-life (EOL) automotive cells, at different SOHs. Nowadays, there is a lack of reliable and accurate battery models to assess the applicability of EOL batteries, giving them a second-life in stationary applications. Consequently, the battery model developed in this work could simulate the performance of a real second-life battery system.
Moreover, this work has been presented a set of algorithms for the estimation of SOC, specifically deployed for lithium-ferrum-phosphate (LFP) batteries. The algorithms proposed are founded on state-observers model-based approach. Especially for LFP batteries, key factor is the introduction of a hysteresis property inside the battery voltage model for an adequate treatment of SOC estimation error.
Finally, an innovative SOH diagnosis method for lithium-based cells is proposed. Battery SOH can be detected by exploiting impedance measurements obtained by fast active electrochemical impedance spectroscopy test. Key factors are the following: first, the excitation on the battery has been generated by a novel electronic prototype. This prototype is made up of cheap facilities and can perform EIS tests with reduced time duration and low energy consumption. Second, the experimental EIS test has been shown the possibility to determine frequency points in which the impedance measurements dramatically change due to different cell SOH. As a consequence, these peculiar frequencies can be adopted as a reference for cluster separation and SOH determination.

Contents

List of Figures

List of Tables

Glossary

OBELICS	Optimization of scalaBle rEaltime modeLs and functIonal testing for e-drive ConceptS
GHG	Greenhouse Gas Emission
EU	European Union
ESS	Energy storage system
BESS	Battery energy storage system
ICEV	Internal combustion engine vehicle
EV	Electric vehicle
BEV	Battery electric vehicle
BEV	Hybrid electric vehicle
LIB	Lithium-ion battery
EOL	End of life
LTO	Lithium-titanate-oxide
LCO	Lithium-cobalt-oxide
LMO	Lithium-manganese-oxide
LFP	Lithium-ferrum-phosphate
NMC	Nickel-manganese-cobalt
NCA	Nickel-cobalt-aluminum
BMS	Battery management system
AC	Alternate current
DC	Direct current
CC	Constant current
CV	Constant voltage
ISO	International standard organisation
IEC	International electrotechnical commission
SAE	Society of automotive engineers
SAE	State of charge
SOE	State of energy
SOL	State of life
SOH	State of health
SOAP	State of available power
OCV	Open Circuit Voltage
KF	Kalman filter
NLKF	Non-linear Kalman filter

EEC	Electrical equivalent circuit
PDE	Partial differential equation
LTI	Linear and Time Invariant
MMSE	Minimum mean square error
EIS	Electrochemical impedance spectroscopy
SEI	Solid electrolyte interphase
R_Ω	Internal resistance
R_{CT}	Charge-transfer resistance
R_{SEI}	SEI resistance
R_{SEI}	SEI capacitance
C_{DL}	Double layer capacitance
PRS	Pseudo-random sequence
PRBS	Pseudo-random binary sequence
DOD	Depth of discharge
BUT	Battery under test
CFT	Curve fitting toolbox
LUT	Look up table
SOA	State of art
SISO	Single-input-single-output
ARX	Autoregressive exogenous model
PEM	Minimum error prediction
DOF	Degree of freedom
TI	Texas instrument
GPIO	General purpose input-output
SPI	Serial peripheral interface
I2C	Inter integrated circuit

Chapter 1

Introduction

Nowadays, the consumption of fossil fuels and the related increment of greenhouse gas (GHG) emissions have become major challenges to environmental pollution. Figure 1.1 shows the total GHG emissions by European countries. With the target to reduce the GHG emissions, it's noticeable that there was a huge decrease in Germany and in United Kingdom from 1990 to 2018, viceversa respect to Turkey and Spain. As shown in Figure 1.2, greenhouse gas emissions in 2018 were down by 21 % compared with 1990 levels, representing an absolute reduction of 1018 million tonnes of CO2-equivalents. This fact led to put the European Union (EU) on track to surpass its 2020 target, which is to reduce GHG emissions by 20 % by 2020 and by 40 % by 2030 compared with 1990 [1]. Currently, there are several solutions to reach this target. Electrical energy storage systems (ESS) may be a key element in a successful energy transition, reducing the fossilized and enabling the renewable supply energy systems. A variety of energy storage technologies are currently available in the market, from the classical mechanical energy storage (citing the most used pumped hydro storage), heat storage, chemical storage, and finally, electrochemical storage [2]. In particular, secondary rechargeable batteries are more considered in the automotive field. Referring to Figure 1.3, more and more attention from governments, industries and research institutions are focused on alternative sustainable solutions able to reduce the emission by the transportation sector. That is the substitution of the internal combustion engine vehicles (ICEV) with the battery electric vehicles (BEV). To ensure a minimum driving range a large, expensive battery is required for BEVs. According to [3], battery represents the 75% of EVs powertrain cost, which means that the adoption towards BEVs mainly depends on the willingness to pay for the extra cost of the battery. Secondary and rechargeable batteries belong to the family of electrochemical storages that store and release electric energy through chemical reactions.

Total greenhouse gas emissions by countries (including international aviation, excluding LULUCF), 1990 - 2018
(Million tonnes of CO2 equivalents)

	1990	1995	2000	2005	2010	2015	2018	Share in EU-27*
EU-27	**4 911.6**	**4 626.5**	**4 543.4**	**4 647.1**	**4.3**	**3.9**	**3 893.1**	**100.0%**
Belgium	149.6	157.4	154.4	149.9	0.1	0.1	123.6	3.2%
Bulgaria	102.5	75.5	59.8	64.7	0.1	0.1	58.6	1.5%
Czechia	199.6	158.5	151.2	150.0	0.1	0.1	129.4	3.3%
Denmark	72.6	80.5	73.6	69.3	0.1	0.1	51.3	1.3%
Germany	1 261.6	1 136.4	1 063.0	1 016.4	1.0	0.9	888.7	22.8%
Estonia	40.4	20.2	17.3	19.2	0.0	0.0	20.2	0.5%
Ireland	56.6	60.3	70.1	72.2	0.1	0.1	64.2	1.7%
Greece	105.8	112.0	129.0	139.1	0.1	0.1	96.1	2.5%
Spain	294.2	335.6	398.4	455.0	0.4	0.4	352.2	9.0%
France	556.9	553.7	567.2	570.7	0.5	0.5	462.8	11.9%
Croatia	32.4	23.0	25.9	30.2	0.0	0.0	24.4	0.6%
Italy	520.4	535.3	560.5	595.1	0.5	0.4	439.3	11.3%
Cyprus	6.4	7.9	9.3	10.2	0.0	0.0	9.9	0.3%
Latvia	26.6	13.1	10.6	11.6	0.0	0.0	12.2	0.3%
Lithuania	48.4	22.5	19.6	22.9	0.0	0.0	20.6	0.5%
Luxembourg	13.1	10.7	10.6	14.3	0.0	0.0	12.4	0.3%
Hungary	94.5	75.9	74.0	76.2	0.1	0.1	64.1	1.6%
Malta	2.8	3.0	3.1	3.2	0.0	0.0	2.7	0.1%
Netherlands	226.3	239.3	229.7	225.7	0.2	0.2	200.5	5.1%
Austria	79.4	80.7	82.0	94.4	0.1	0.1	81.5	2.1%
Poland	475.7	447.5	396.7	405.4	0.4	0.4	415.9	10.7%
Portugal	60.2	70.4	83.7	88.0	0.1	0.1	71.6	1.8%
Romania	248.8	187.9	143.6	151.8	0.1	0.1	116.5	3.0%
Slovenia	18.7	18.7	19.1	20.5	0.0	0.0	17.6	0.5%
Slovakia	73.6	53.4	49.3	51.4	0.0	0.0	43.5	1.1%
Finland	72.2	72.7	71.3	71.2	0.1	0.1	58.8	1.5%
Sweden	72.5	74.6	70.1	68.6	0.1	0.1	54.6	1.4%
United Kingdom	809.7	768.1	742.5	726.6	0.6	0.5	498.7	12.8%
Iceland	4.0	3.8	4.6	4.5	0.0	0.0	6.2	0.2%
Lichtenstein	0.2	0.2	0.2	0.3	0.0	0.0	0.2	0.0%
Norway	52.1	52.2	56.0	56.3	0.1	0.1	53.8	1.4%
Switzerland	57.3	56.8	58.0	59.1	0.1	0.1	52.1	1.3%
Turkey	219.9	248.6	300.4	340.5	0.4	0.5	533.0	13.7%

*Share in EU-27 total in year 2018

eurostat

Source: European Environment Agency (online data code: env_air_gge)

Figure 1.1: Total greenhouse gas emissions (including international aviation, excluding LULUCF), by country, 1990–2018 (million tonnes of CO2-equivalents), source: Eurostat: European Evironmental Agency

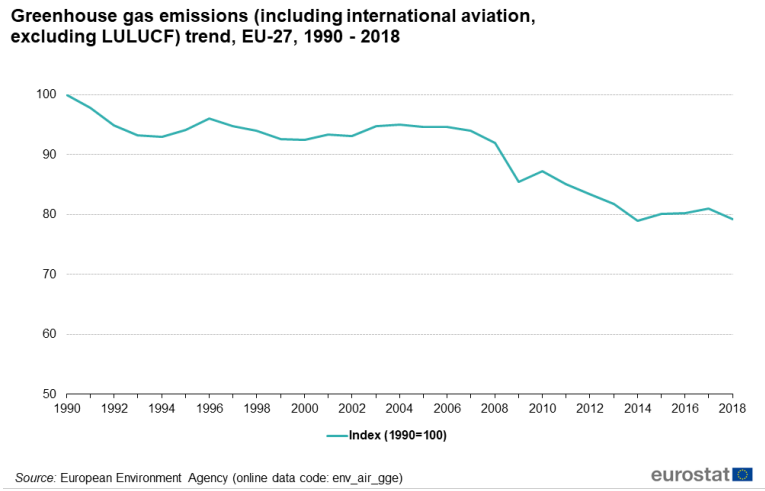

Figure 1.2: Total greenhouse gas emissions (including international aviation, excluding LULUCF) trend, EU-27, 1990–2018, source: Eurostat: European Evironmental Agency

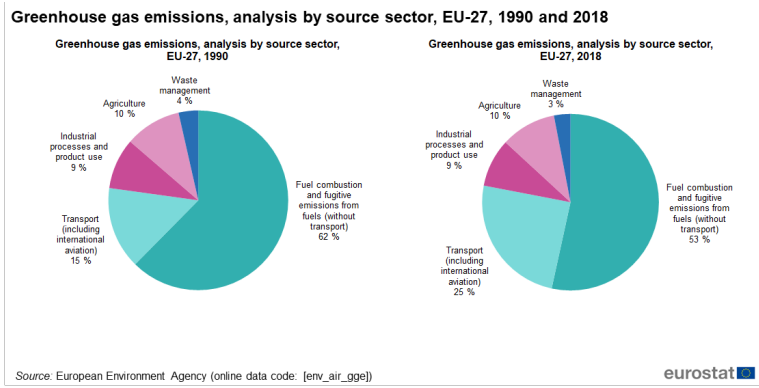

Figure 1.3: Greenhouse gas emissions, by source sector, EU-27, 1990 and 2018 (percentage of total), source: Eurostat: European Evironmental Agency

1.1 The role of lithium-ion batteries: cost, applications, future

Currently, the automotive market is still dominated by ICEV. However, the current market and technology trends are leading to the rapid growth and diffusion of EVs and HEVs, as can be observed in Figure 1.4. According to [5], the market share of ICEV is predicted to fall from 99% in 2015 to 68% in 2030. This evolution technology split in favor of electrification will result in an increasing demand for automotive batteries [4]. The inexhaustible study for new battery technologies continues to rage between research institutes, universities and the industry. Due to high power and energy density, as shown in [7] and Figure 1.5, lithium-ion battery (LIB) technologies have become more and more diffused not only in the field of portable electronics [6], but also in the automotive industry. First commercial cell was sold by Sony in 1991. The commercially available LIBs are creeping up on their theoretical maximum energy density of around 400-600 Wh/kg [8]. As previously mentioned, exciting market potential of LIBs concerns portable electronics and automotive field. Moreover, an increasing BEV and HEVs demand is foreseen. Therefore LIBs will benefit from cost and performance optimizations arising from a large scale production. According to [5] the limit of 100 dollars/kWh will be reached in 2025-2030 for several lithium-based batteries. To overcome this limit, the reuse of automotive LIBs after their end-of-life (EOL), giving them a second life, has been considered one of the promising solutions to satisfy the battery demand of various sectors. LIB is considered in EOL if its current capacity is at 85-80% of nominal value. Despite a noticeable decrease in battery performance in EOL, as depicted in [9], second-life batteries are still expected to be capable of storing, delivering substantial energy and meeting the requirements of less-demanding applications, where reduced performances are still acceptable [10][11]. Hence, there is the possibility to extend the market of LIBs, building and spreading 2nd life battery energy storage systems (BESS) to support the renewable supply energy systems. Moreover, car manufacturers will have the possibility to exploit the second use option in an attempt to expand their portfolio and enter in the stationary battery market. In cooperation with utility companies, they are launching several pilot projects of battery second-life, and first 2nd life BESS demonstrators are close

to realization. For example, the 3MWh BESS demonstrator in Amsterdam Arena. This storage system provides a more reliable and efficient energy supply and usage for the stadium, its visitors, neighbors and the Dutch energy grid. Combining Eaton power conversion units and the equivalent of 148 Nissan LEAF batteries, the energy storage system not only enables a more sustainable energy system, but it also creates a circular economy for electric vehicle batteries. Another important 2nd life BESS demonstrator will be built in Lunen (Germany). The most noteworthy feature of the project is that the LSS has been built from 1000 used battery modules from second generation "Smart for two" BEVs [12]. The summary of the 2nd life projects is presented in [13].

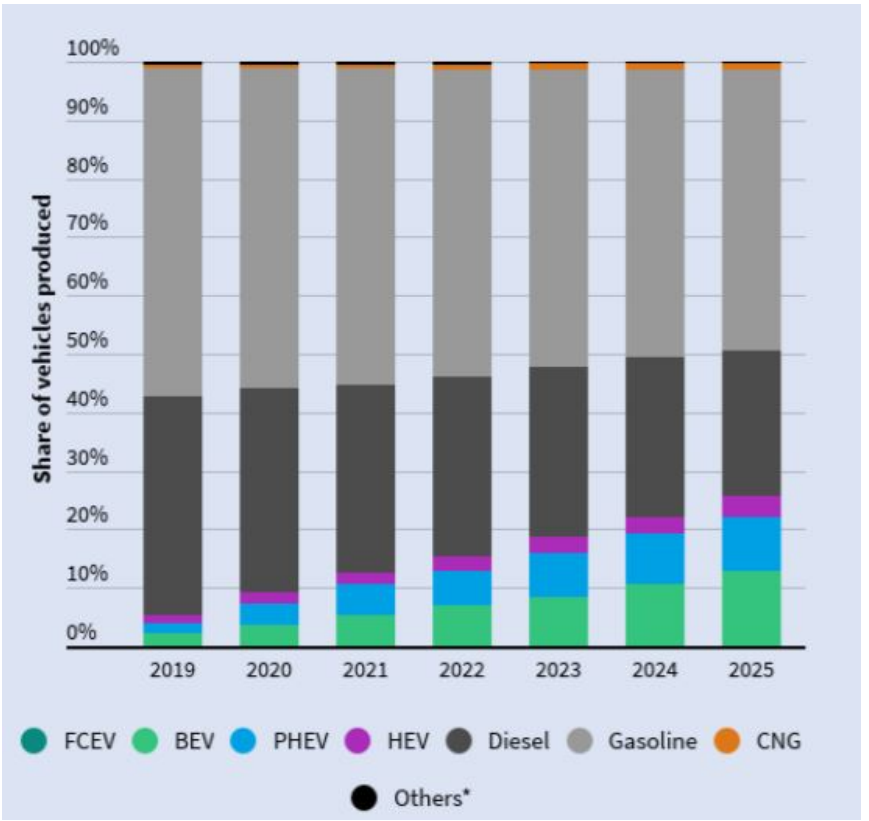

Figure 1.4: Evolution technology split of vehicles per type in Europe, Source: IHS Markit.

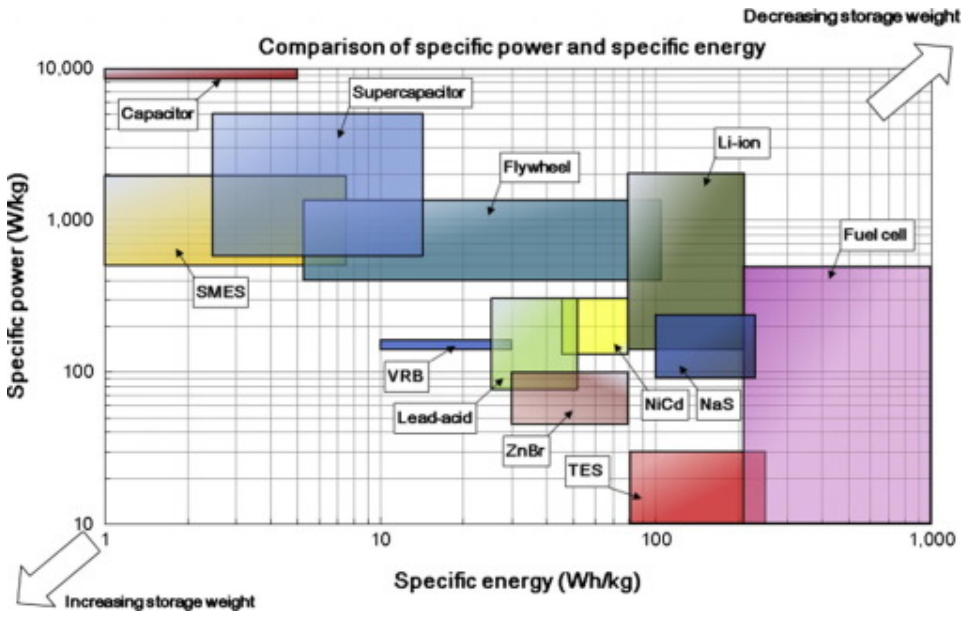

Figure 1.5: Comparison of specific energy and specific power, Source: Luo [7].

1.2 Lihium-ion cell chemistry

A lithium-ion cell typically comprises porous electrodes (anode and cathode), an insulating layer (separator) and an ionically conducting solution (electrolyte).
In a real cell, both electrodes are typically electroactive materials mixed with electrically conducting additives which are coated onto copper (anode) and aluminum (cathode) current collectors. The active material of electrodes serves as a host material in which lithium-ion particles can be intercalated from the electrolyte or they can be extracted. Electrolyte serves as catalyst to make a battery conductive by promoting the movement of lithium-ions (electrons are not allowed) from the cathode to the anode, or viceversa. Considering liquid electrolyte solutions, an electrically insulating layer, the so-called separator, is inserted between cathode and anode. It aims to prevent a short circuit in the case that liquid electrolyte will dry up for an abnormal condition, such as the increase of cell internal temperature.
A schematic illustration of a lithium-ion cell's functioning is depicted in Figure 1.6. The lithium-ion particle is an alkali metal that has the highest electrochemical potential (3.04V), which means that has the highest tendency to lose the only one valence electron. When lithium particles are part of an oxide methal, they are quite stable. Hence, the cathode material, the pole negative of battery, is composed of oxide methal. When the battery is charged by an external supply source, the valence electron of lithium particles is attracted by the supply voltage and arrives in the battery's anode, the positive part. At the same time, lithium-ion particles are intercalated in the anode towards the electrolyte. Battery is considered fully charged once that all lithium-ion particles are intercalated in the anode. The anode material is usually composed of graphite layers. It means that lithium particle is in an unstable state while is intercalated in the anode, and tends to go back in a stable state, hence in the cathode. Therefore, when an electrical load is connected

in the cell, the lithium-ion particles move to the cathode towards the electrolyte, while electrons flow towards the load, hence delivering current.
Currently, many research efforts allowed to optimize cathode and anode material in order to increase cell energy density. In this regard, small amounts of metals with high theoretical energy densities, such as silicon, is added in the graphite layers of anode. This lead to increase the overall energy density [6]. An alternative for the graphite material is the titanate-oxide [15].
Concerning the cathode, there are several solutions: the most suited cathode material is strongly dependent on the application itself. From Battery University website [15], several lithium-ion cathode based type are compared with respect to the most important feature which represents a single cell:

- LCO: Cobalt-Oxide material.
- LMO: Manganese-Oxide material.
- NMC: Nickel-Manganese-Cobalt-Oxide material.
- LFP: Ferrum-phosphate-Oxide material.
- NCA: Nickel-Cobalt-Aluminum-Oxide material.

Features of different cathode lithium-based chemistry, which hosts the lithium-ion particles, are depicted in Figure 1.7. Currently NCA, NMC, and LFP cathode-base cells are the most diffused as energy storage in automotive industry. Due to the specific energy, it is expected that the adoption rate of the LFP battery is decreasing, meantime the adoption rate of the NMC and NCA batteries, especially NMC, is constantly increasing. By observing Figure 1.8, the adoption rate of the NMC battery is expected to increase from 53% in 2019 to 64% in 2025 for EVs. Despite this, currently some battery industry companies prefer the LFP technology, which is the safest in the battery market. Always regarding the LIBs in automotive field, the efficiency and the safety of the battery packs are the main factors which must be fulfilled. Consequently, a unit electronic called Battery Management System (BMS) is usually employed, to ensure battery safety and to improve its performance in terms of efficiency, increasing its lifetime. According to this, the most important internal states of the battery pack have to be carefully monitored, whose related algorithms are included inside BMS. In the next section, an overview of specifications which characterize LIB and international design, safety and performance test are shown. Moreover, the most important battery safety and performance indicator are shown in the next section.

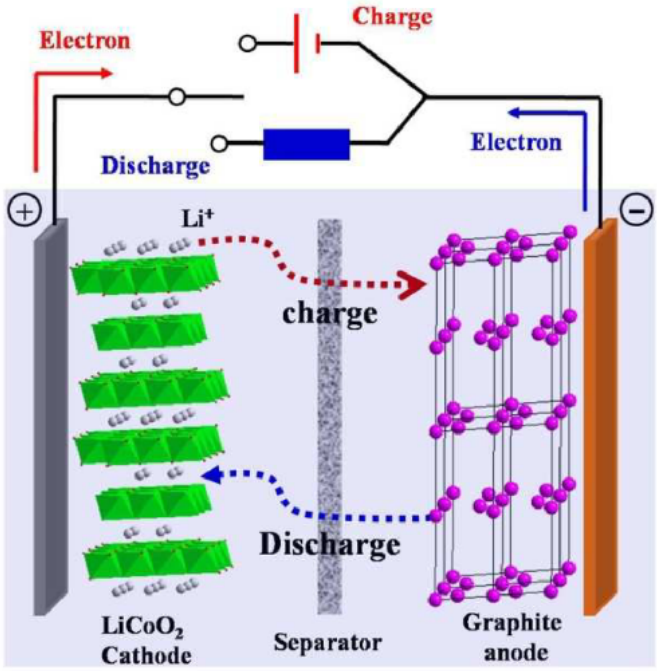

Figure 1.6: Illustration of the charge and discharge process in a lithium-ion cell. Source: Xu [14]

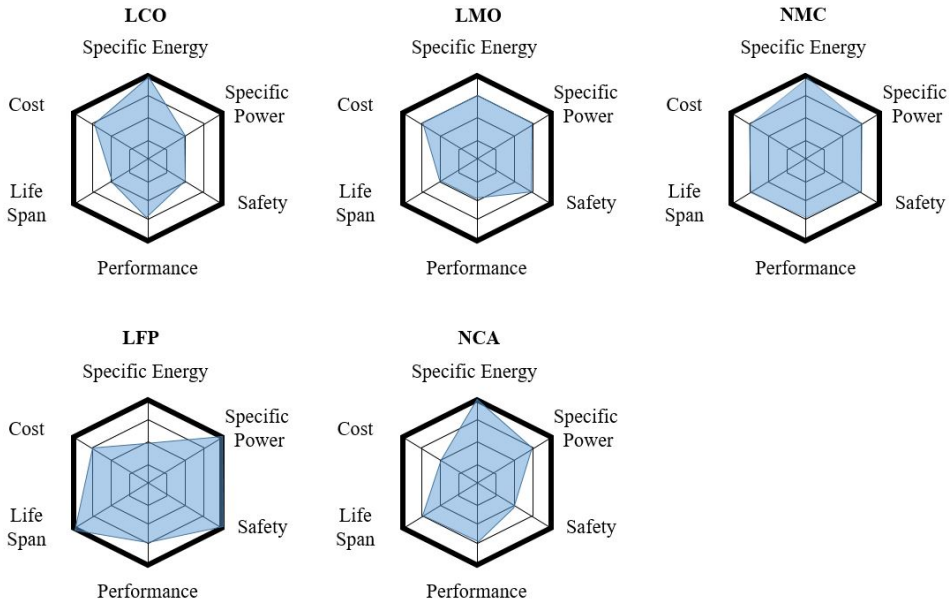

Figure 1.7: LIB cathode-base feature's comparison. Source: Battery University website (update 2019).

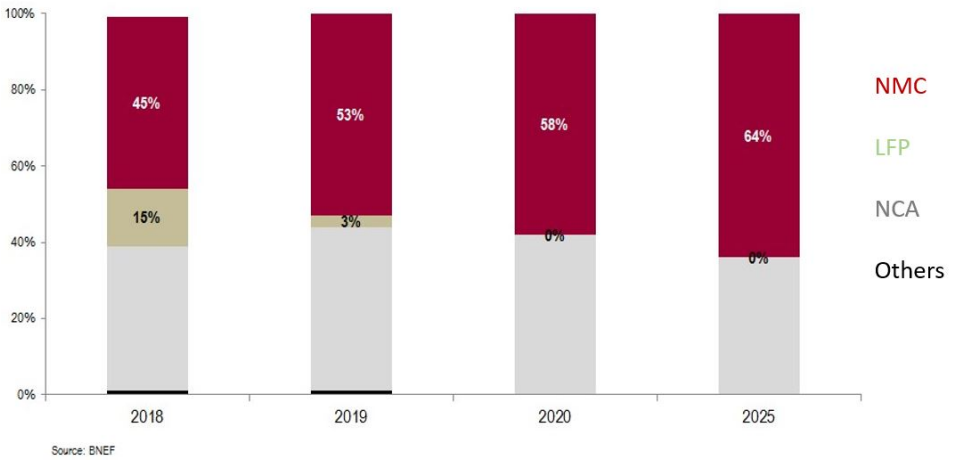

Figure 1.8: Adoption rate per chemistry in EVs battery market (global).

1.3 Battery performance and safety indicators

Single lithium-ion cell is characterized by the following general specifications:

- **Rated capacity (Ah)** is the amount of energy that can be withdrawn from it at a particular constant current, starting from a fully charged state.
- **Rate of discharge (C)** also known as C-rate. It is a measure of the rate at which a cell is discharged relative to its maximum capacity.
- **Nominal Voltage (V)** is the average voltage of the cell when charged.
- **AC Impedance (mΩ)** is the measure of battery impedance (sum of internal resistance and reactance) when battery is excited with a 1kHz-frequency sinusoidal current.
- **Energy Density (Wh/kg or Wh/dm^3)** is the amount of energy which battery can store per unit of weight or volume.
- **Power Density (W/kg or Wh/dm^3)** indicates the delivering/supplying capability of the battery per unit of weight or volume.
- **Self-discharge (% per days)** is a phenomenon in cells in which internal chemical reactions reduce the stored charge without any connection between the external circuit. The energy loss, per days, of all cell chemistries, increases at higher temperatures and aging.
- **Operating temperature range (°C)** is the range of ambient temperature within which a cell operate in. Depending on the cell operating condition, this specification ranges from a minimum operating temperature to a peak or maximum operating temperature, outside which, the cell may fail.
- **Lower voltage limit for discharge (V)** represents, for any normal usage, the lowest value to discharge the cell to. This threshold voltage does not include any discharged current specified.

- **Maximum discharge current in continuous (A or C-rate)** is the maximum current at which the battery can be discharged continuously.
- **Maximum peak discharge current (A or C-rate)** is the maximum current at which the battery can be discharged for pulses of a specified time duration (usually 10 or 30s).
- **Maximum voltage limit for charge (V)** represents, for a specified charging method, the maximum voltage to charge the cell.
- **Recommended charge current (A or C-rate)** represents, for a specified charging method, the continuous charge current to apply on the cell during the constant current charging phase.
- **Charging method** represents the procedure to charge the cell in order to increase the battery lifespan. The most common charging method applied for all battery chemistries is represented by a combination of constant current (CC, with a recommended charge current) and constant voltage charging phase (CV). By reaching the maximum charge voltage, CV charge control decreases continuously the current with constant voltage until the current was not more than a specified minimum charging current value.
- **Cycle life (n. of cycles)** refers to how many complete charges and discharges a cell can be used before it reaches the EOL. In automotive field, battery is considered in EOL if its rated capacity (Ah) is at 85-80% of the nominal capacity.
- **Discharge curves** are represented by graphs Ah/V, they show how the cell voltage is reduced with respect to the amount of energy that is withdrawn from a different constant discharge currents or room temperatures.
- **Mechanical characteristics** specify the dimensions (length, width, thickness), the weight and the shape of a cell.

Mechanical characteristics of a single cell are approved according to the international standard ISO PAS 16898 (22/07/2020 withdrawal of international standard). The ISO PAS 16898 specifies the shapes and dimensions for lithium-ion cells for integration into battery packs and systems used in electrically propelled road vehicles [17]. Three different cell designs are being developed and produced today: cylindrical, prismatic and pouch cells (Figure 1.9). Cylindrical cells (in several formats: 18650, 21700, 26650) have been the most used in the past, especially in portable electronics. Their container is dense and resistant, withstanding some inner pressure without deformation. The disadvantages of cylindrical cells are the low capacity of a single cell. Hence the cells are assembled in series and in parallel with a weld. This does not allow the replacement of a single cell but requires the replacement of an entire module with more invasive and expensive interventions. Moreover, cylindrical cells show a lower heat transport from inner cell parts to the outside [16]. Prismatic cells are from the construction point of view similar to cylindrical cells. Their container is dense and resistant. Usually, prismatic cells have screw terminals, this simplifies assembly and makes it easy to replace a single cell. Moreover it's possible to develop a single cell with high capacity. Nevertheless, due to the container thickness, the energy density of a prismatic cell is lower

than the other types. Pouch cells can be an important alternative to replace the cylindrical and prismatic types, due to the higher energy density per unit of volume and weigth. This benefit is due to their very fine thick container. Nevertheless, the container is very delicate, therefore easily damaged compared to high mechanical pressures. Moreover the quality of the welding is an issue even after several years of ongoing development.
Electrical characteristics of a single cell are evaluated and approved by performing and safety testing, according to several international standards. At a worldwide level, standardization is mainly under the competence of two institutions: the international electrotechnical commission (IEC), founded in 1906, and the international organization for standardization (ISO), founded in 1946. Compare to IEC, which is work on electric components and electric supply infrastructure, ISO considers an electric vehicle, as a whole. The main LIB standards developed by these two standards are as follow:

- **ISO/NP PAS 16898:** This standard focuses on electrically-propelled road vehicles battery system design. It checks for the requirements on dimensions for lithium-ion cells for vehicle propulsion [17].

- **ISO 12405:** Specifies test procedures for LIB packs and systems, to be used in electrically-propelled road vehicles. ISO 12405 consists of the following parts, under the general title "Electrically-propelled road vehicles — Test specification for lithium-ion traction battery packs and systems":

  - **Part 1: High power applications (2012):** This part of ISO 12405 specifies test procedures for LIB packs and systems. The specified test procedures enable the user to determine the essential characteristics of performance, reliability, and abuse of LIB packs and systems [17]. This part was withdrawn in 2018 and replaced by ISO 12405-4.
  - **Part 2: High energy applications (2012):** This part specifies the performance tests for high energy LIB packs and systems [17]. This part was withdrawn in 2018 and replaced by ISO 12405-4.
  - **Part 3: Safety performance requirements (2014):** The specified test procedures enable the user to determine the essential characteristics of the safety performance of LIB packs and systems. This part was withdrawn in 2019 and replaced by ISO 6469-1.
  - **Part 4: Performance testing (2018):** This part specifies test procedures for the basic characteristics of performance, reliability and electrical functionality for the battery packs and systems for either high-power or high-energy application. Performance testing on cell level is specified in IEC 62660.
  - **ISO 6469-1: Safety specification part 1- Rechargeable energy storage systems (2019):** This part specifies safety requirements for rechargeable energy storage systems of electrically propelled road vehicles for the protection of persons.

- **IEC62660:** This standard is to specify performance testing for automobile traction lithium-ion cells (single cell) and batteries.

- **Part 1 (2018): Performance aspects:** This part of IEC 62660 specifies performance and life testing of secondary lithium-ion cells used for propulsion of electric vehicles [17].
- **Part 2 (2018): Safety aspects:** This part specifies the reliability and abuse testing for lithium-ion cells for electric vehicle application [17].
- **Part 3 (2016): Safety requirements:** This part specifies test procedures (described in IEC 62660-2) and acceptance criteria for safety performance of secondary lithium-ion cells, cell blocks and modules [17].

Overcited standards cover three main aspects of LIBs applied in EVs: design, performance and safety aspects. Figure 1.10 illustrates the standards of batteries with respect to these three aspects. Table 1.1 gives the general overview of the different test standards which are covered by ISO 12405 and IEC 62660. Further international organisation, such as the Society of Automotive Engineers (SAE) had developed performance and safety standard test for automotive LIBs (SAEJ2929 and SAEJ2380 [17]). Finally, national bodies, as Japanese Industrial Standards Commette (JISC), Chinese industry standards (QC/T), Indians, Korean, Americans etc. Deep reviews of international and national testing standards of LIBs in automotive industry are reported in [17]-[19].

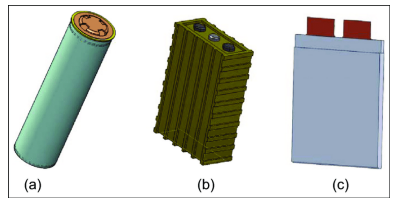

Figure 1.9: Various cell designs: (a) cylindrical, (b) prismatic and (c) pouch. Source [16].

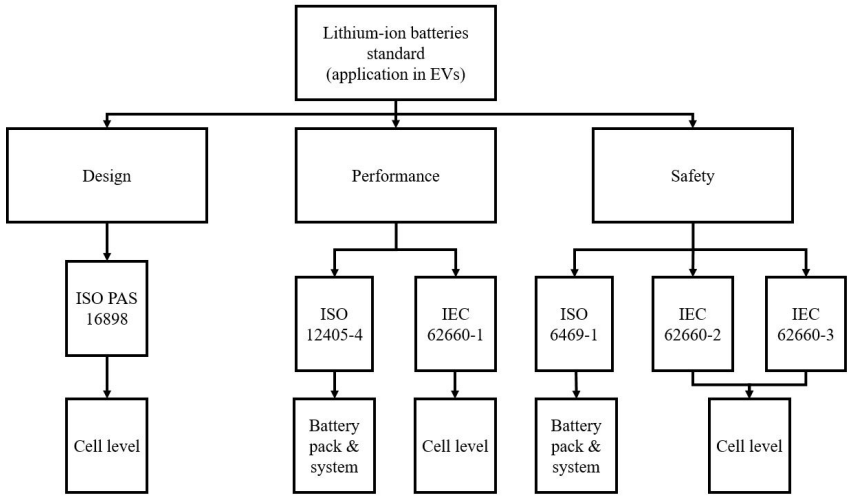

Figure 1.10: International standards of EVs LIB.

Standard	Year	Content	Battery Level	Test
ISO 12405-4	2018	Performance test	Battery pack	Energy and capacity at room temperature Energy and capacity Power and internal resistance No load SOC loss SOC at storage Cranking power at low temperature Cranking power at high temperature Energy efficiency Cycle life
IEC 62660-1	2018	Performance test	Cell	Capacity Power Energy Storage test-Charge retention Storage life test Cycle life (BEV) Cycle life (HEV) Energy efficiency
ISO 6949-1	2019	Safety test	Battery pack	Vibration Mechanical shock Dewing Thermal cycling Simulated vehicle accident Inertial load at vehicle crash Contact force at vehicle crash Water immersion Exposure to fire Short circuit Overcharge protection Overdischarge protection Loss of thermal control/cooling
IEC 62660-2	2018	Performance test	Cell	Vibration Mechanical shock Crush High temperature enedurance Temperature cycling External short circuit Overcharge Forced discharge

Table 1.1: Various test standard covered by ISO 12405 and IEC 62660 [17]

All safety and performance indicators are evaluated referring to the international standards overcited in laboratory. In order to preserve the battery performances on-board the EVs and during lifetime and enable safe and reliable operation of the battery pack, BMS is usually employed. The BMS consists of hardware and software for battery management including, among others, algorithms determining battery internal states, hence the safety and performance indicators. These algorithms monitor continuously battery internal states based on current, voltage and temperature (ambient or surface) measurements. Since batteries are complex electrochemical devices with a distinct non-linear behavior depending on various internal and external conditions, their monitoring is a challenging task. The most cited internal states, not directly measurable of LIBs are the following ones:

- **Capacity (Ah), internal impedance (Ω), internal temperature (°C):** They are considered internal states because they are not directly measurables.
- **State of charge (SOC, %):** corresponds to the ratio between the stored battery capacity and the nominal one.
- **State of energy (SOE, %):** is a straightforward description of the available energy state of batteries [20]. SOE is the ratio between the stored battery energy and the nominal one.
- **State of life (SOL, %):** considers the capacity degradation over time due to the normal charging-discharging operating conditions, by considering modification in battery capacity or internal resistance [21].
- **State of health (SOH, %):** considers the battery performance degradation over time due to unexpected events, always by considering the variation of battery capacity or internal resistance.
- **State of available power (SOAP, W)):** considers the current maximum available power of the battery, depending on battery current condition (SOC, SOH and internal temperature).

As previously mentioned, battery internal states are estimated by current, voltage and temperature measurements. The mathematical methods for a single battery internal state estimation could depend by several battery internal states estimate [22]. A typical interaction and information flow among individual methods within of the battery monitoring system is shown in Figure 1.11. It's important to specify that the estimation of different battery internal states are performed on different time-scales, assuming that the evolution of state of charge shows short-time variations than SOH or SOL. By Figure 1.11, it's noticeable that all battery internal states depend on the estimation of battery internal resistance and battery capacity. A large variety of mathematical methods and algorithms for the monitoring of battery internal states overcited are developed and presented in scientific and technical literature. Critical review and comparison of battery SOC and SOH methods are presented in [22]-[24]. The aim of the PhD thesis consists of the development of novel methods for monitoring battery internal states, focusing, in the first part on battery SOC estimation and, in the second part, on SOH estimation. A depth review of the SOC and SOH state-of-art methods is presented in the next section, and, by the lacks found in literature, the contribution of this PhD thesis is presented, concluding the introduction.

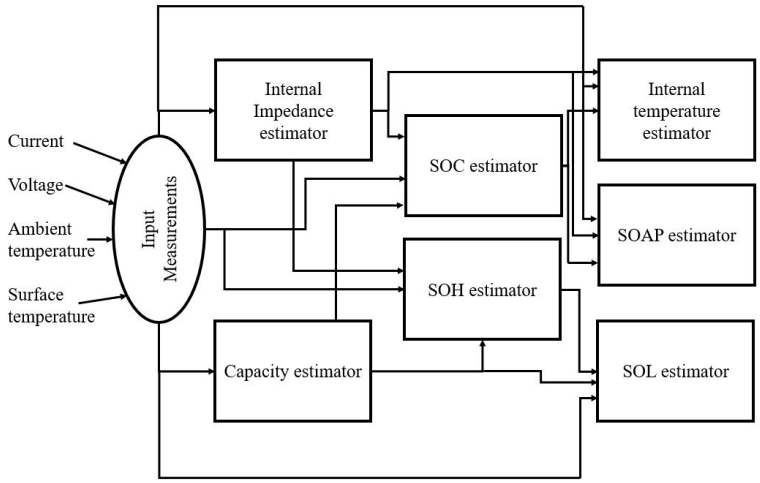

Figure 1.11: Typical block system aiming to monitor battery internal states.

1.4 Literature review

The increasing number and variety of papers available in the literature show the raising interest about monitoring battery. Research of new methodologies to predict accurately battery states and capable in embedded systems is an attractive challenge task.

1.4.1 SOC estimation methods

Concerning SOC estimation, there are a wide range of approaches proposed in literature. Generally, these methods can be classified in four categories:

- **Ampere-hour counting method:** At the time istant t, the evaluation of the SOC is in according to time-continuous equation (1.1), calculating the integral of the current delivered/absorbed by the battery.

$$SOC(t) = SOC(0) - \left[\frac{1}{3600 C_{nom}} \int_0^t i(\sigma) d\sigma\right] \times 100 \tag{1.1}$$

  When the maximum available capacity C_{nom} of battery and initial SOC is known, and its current i can be measured precisely, equation (1.1) gives in output an accurate calculation of the variation of the SOC. This method requires very low computational cost and low-cost current sensors. However it shows many drawbacks: first, initial SOC and maximum capacity must be known. For LIB, the battery capacity depends on the battery conditions at the end of discharge, on the current rates during the complete discharging process (short-time discharge history), and finally, on the temperature [25]. Finally, the measurement errors of battery current from random disturbances, such as noise and temperature drift, are inevitable. For these reasons, this method could be unreliable in many scenarios.

- **OCV-based methods:** Open circuit voltage (OCV) is the difference of electrical potential when battery is disconnected from any circuits. The SOC

of battery has a direct mapping relationship with OCV. Figure 1.12 shows an example of OCV-SOC relationship for different LIB chemistries. This method requires low computational cost. However this method can be used when EVs or HEVs are in rest phase for at least half-hour, in which battery voltage reaches its stationary condition. Hence this method cannot be used when EVs are driven. Then, the OCV-SOC relationship assumes a flat curve in the middle of the SOC window range for LFP batteries, as shown in Figure 1.12. Moreover, as demonstrated in [27], there is a difference between charging and discharging OCV-SOC curves, due to the hysteresis behavior which LFP batteries have. Hence, it's so difficult to predict SOC based on only OCV information, especially for LFP cathode type.

- **Data-driven methods:** Data-driven methods use the input-output experimental data of the real dynamic system to develop a virtual model. These methods include the application of fuzzy logic, statistical and machine learning approach, by considering battery system as a black-box model. Hence, since these models do not require an accurate battery model, it leads to a reduction of the computational cost of the algorithm. Nevertheless, the state estimation accuracy of this method depends only on the experimental data acquired on battery. An immense amount of measured data history is needed in order to train the black box battery model. Finally, the training data should completely cover all the possible battery operating conditions for a good state estimation. Battery state behaviors depend on many external factors, such as temperature, aging, current rate, etc. Hence, it's difficult to obtain a good robustness of this method with respect to different mission profiles or scenarios.

- **Model-based observers:** The main idea of this approach is to estimate the internal states by the battery current, voltage and temperature measurements, employing a battery mathematical model. Model-based observer is realized by battery voltage and current measurements acquired online and by a priori knowledge of a battery model. These models will be presented in the next chapter. Respect to data-driven methods, these methods do not require an immense amount of measured data history for a good battery state accuracy. The calibration and the identification of model parameters can be carried out offline, through lab tests, or online. Since these methods require an accurate model for a good state estimation, the main drawback is the trade-off to obtain a high accuracy with high computational efforts.

Requiring few data to identify the model of battery, and being a closed-loop method, model-based approach is preferred to estimate battery SOC.
Beyond the chosen battery model, which is discussed in the next chapter, it is important to choose the state estimation criterion. Concerning non-linear models, Luenberger [28], sliding mode [29], extended [30] and unscented [31] Kalman filter approach [33]-[37] are the most used as model-based observers in literature. The Kalman filter belongs to the Bayesian filter's family: the state estimation is computed by a model affected by additive noise (process noise) and by considering observations obtained by a network of sensors affected by additive noise (measurement noise). In this work additive process and measurement noises are considered as Gaussian white noises with zero mean and appropriate covariances. Given the last assumption, Kalman filter (KF) is the best estimator in the sense of mini-

mum mean square error (MMSE) for state estimation of linear and time-varying dynamic systems. However, an accurate battery model is represented by non-linear differential equations. Hence, several types of non-linear Kalman filters (NLKFs) techniques will be tested and evaluated in the Chapter 3.

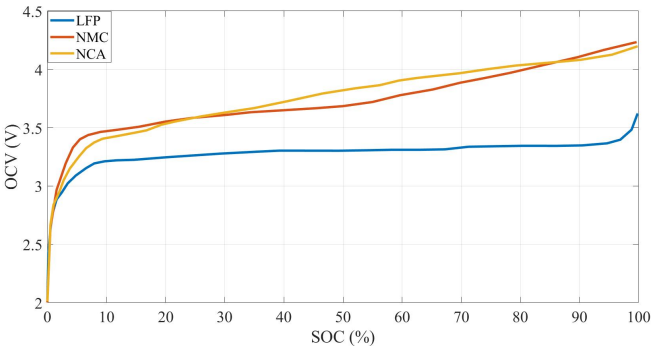

Figure 1.12: OCV of the investigated cells in [26].

1.4.2 SOH estimation methods

Battery SOH is a metric to evaluate the capacity fade and/or power fade after anomalous or failure events. The capability of the battery to store energy (measured in current capacity Ah) and provide a certain power decreases over the battery life because of aging or unexpected events. Despite the importance of battery SOH analysis, it still does not a consensus in the literature on how the SOH should be determined. One of the most common SOH parameter assessment is the comparison of the current evaluated capacity with standard cycle with respect to the initial capacity [23]. The development of improved battery SOH monitoring methods is still one of the main research topics in the field of LIBs in the automotive field. With the possibility to have in feedback battery SOH, the electronic unit (BMS) can dynamically regulate battery packs current in order to maintain it continuously in safe operating conditions and prolonging its lifetime. Hence, SOH diagnostic method should be incorporated on-board the EV, in the BMS.
Generally, different approaches for SOH estimation are proposed in literature and can be classified into three categories:

- **Data-driven methods:** the state estimation is computed directly from data, through a block-box model build by a training data-set. It requires low computational efforts. However, obtaining an effective training data-set, considering the complete operating conditions of the battery, is difficult.
- **Model-based methods:** the model of the system is first derived from experimental data, under lab test, or online calibrated, then the state estimation is computed-based on the model. As previously mentioned, it does not require an immense training data-set. However, it requires high computational efforts for state estimation.
- **Electrochemical impedance spectroscopy (EIS) test methods:** Active EIS introduces an external excitation, in current, to the battery, by

using a well-designed current reference. Monitoring the current input and voltage response, the battery impedance is computed in the frequency band interested. The main advantage of this method is that EIS provides detailed information about the battery chemical-physical changes properties and different aging mechanisms [38]-[40]. However, EIS is considered an expensive, complex, and very time-consuming method.

Model-based methods estimate the state evolution of the battery while presenting limited physical meaning in its parameters. This mismatch between model parameters and physical-chemical properties of the battery can be filled by using EIS test. Battery SOH monitoring based on impedance information, extrapolated by EIS test, is discussed in current research of several secondary battery types [40]-[42] and other energy storage systems [43]-[45]. Concerning this promising method, there is a need to investigate the correlations between impedance information, battery SOH and aging mechanism. Moreover, it is important to investigate the frequency range suitable for the analysis, and the implementation methods to make it easy to use. The aging mechanism can be studied using electrical circuit equivalent models, whose parameters are well identified by fitting impedance data in a defined frequency band. Usually, the Randles circuit models [46] are used to fit impedance data. Phenomena induced by cell structure and by its modification over time include: inductive behaviors, film formation, charge-transfer resistance and double-layer capacitance on the electrode-electrolyte interface, and diffusion processes in the active materials of the electrodes. According to literature [47][48], such phenomena can be investigated by adopting EIS.
Several research works in [38]-[53] confirm a monotonous increase of ohmic resistance (R_Ω) with battery degradation. To demonstrate the robust correlation between R_Ω and SOH, experiments are carried out at different battery operating conditions: in [49][50] at different battery SOC, considering fixed room temperature; in [51][52] at a different rate of discharge; finally at different room temperature in [40][53]. Research work in [54] confirms a correlation between the increase of the resistance charge transfer (R_{CT}) between electrodes with the aging cycles considering different temperature and SOC. In [55], the growth of the solid electrolyte interphase (SEI) film resistance (R_{SEI}) is identified and correlated with battery SOH. Finally, the increase of double-layer capacitance (C_{DL}) with aging is considered in [38][40]. The set of parameters $[R_\Omega, R_{CT}, R_{SEI}, C_{DL}]$ defines one of the possible configurations adopted to simulate battery impedance in frequency domain. More details are described and depicted in Section 2. The parameters cited are identified by using non-linear best-fitting algorithms, for example, the most commonly used Levenberg-Marquardt method. However, these algorithms are the high computational efforts and an accurate choice of initial parameter values. This factor represents a drawback when algorithm is implemented in embedded systems. Other research works propose data-driven methods for post-processing impedance estimation. Data-driven algorithms, applied for SOH estimation, can be considered as non-probabilistic such as artificial neural networks [56], support vector machine [57], and probabilistic method, for example by using Gaussian process regression approach [58]. Other research works show significant results since they determine single frequency points in which the impedance measurements dramatically change due to different cell SOH. Recent study [59] analyzes the increment of measured 100 mHz real battery impedance with aging by testing four different lithium battery chemistry; in [60], the 316 Hz impedance shows negligible change respect to

battery SOC and changes dramatically during overcharge. As a consequence, these peculiar frequencies can be adopted as a reference for cluster separation. These last methods could be a good idea to perform a fast estimation of battery SOH-based on EIS test. However, for the development of an original method, it is fundamental to understand how to perform impedance identification with a simple EIS test procedure and capable for embedded systems and on-board the EV. Therefore, a depth review of the EIS test state-of-art methods is carried out and presented in the next section.

1.4.3 In-situ electrochemical impedance spectroscopy test

The idea is to develop an approach that allows to estimate the impedance of the battery with acceptable accuracy by applying EIS tests. Main requirements that must satisfy the EIS test are the following:

- Reduced EIS test time and battery energy consumption.
- Robust and reliable.
- Simplicity in hardware and software realization, then low-cost.
- Adaptable for embedded systems.

Rapid and online impedance measurements based on active EIS are proposed in the literature in the last years. Classical EIS test consists of applying a set of frequency-controlled sine waves, in current, to the battery under test. However, this method requires long-time test procedures and expensive facilities. Research works [61]-[68] propose different types of "broadband" current signal excitation for EIS identification in a set of frequencies at the same time. By using broadband signals, it is possible to measure a set of desired frequency with reduced test time. One of the most popular broadband excitation signals used is the multi-sine: this signal is a sum of sines which frequency corresponds to the desired discrete set of frequencies measured, with random phase. The multi-sine excitation approach offers more accurate EIS measurements [61], considering a large set of phase patterns [62], and various advantages in the detection of non-linear behaviors [63]. Pseudo-random sequence (PRS) signals are attractive alternatives, due to their low complexity, reduced test time, and good accuracy [64]-[68]. The PRS family signals are periodic sequences that switch between two or three logic levels [64], so they show a simple hardware implementation. More details about the two-logic PRS, the so-called pseudo-random binary sequences (PRBS), are depicted in [65]; the EIS measurement accuracy, by comparing PRBS with other broadband signals, has been evaluated in [66]; in [67] PRBS has been used for tracking of EIS in a large time horizon; in [68] the PRBS has been implemented and generated by a motor controller. Despite the multi-sine signal could provide accurate impedance measurements, the PRBS offers a more simple hardware implementation, which is fundamental for real-time system state monitoring.

1.5 Contribution of the work

Nowadays, SOC estimators based on NLKF observer techniques have been well studied by many authors in literature: recent studies, as [30][31], design SOC estimators with different KF types. SOC estimators have been evaluated at different operating conditions, like temperature [35], load C-rate current and different cell chemistry [36]. In [30]-[37], authors evaluate the robustness of a few configurations of SOC estimators, validated through experimental tests. However, there is a lack of works which compare the performance of a wide configuration of SOC estimators through the model-based approach, in particular KF approach.
Literature analysis shows an extensive investigation of battery SOH estimation [9][22][23], based on active EIS test [38]-[68]. Many research studies have defined some condition indicators, in the frequency domain, to directly quantify SOH. Despite this, the identification of these parameters has been obtained by high computational effort algorithms or with expensive facilities. Most of these studies are limited for an application in real-time targets, making believe that EIS is a bit to academic for a commercial application. The main contributions of this PhD thesis are subdivided into three main aspects:

- The SOC estimation accuracy of a wide range of configurations, i.e. eight different model-based observers, is evaluated: all these variants may present changes in the Kalman Filters used (i.e. Extended or Unscented), in the battery modeling (presence of a hysteresis model or not) or in the battery model parameters evaluation (online or offline). The comparison of these variants has been performed in a systematic approach: SOC estimators performances are evaluated by matching the reference, measured SOC with simulated data, considering also additional disturbances, i.e. different initial condition of estimated SOC, additive measurements and modeling noise levels, finally by changing also the sampling frequency [69].

- Proposed battery model, based on the 2nd-order electrical equivalent Thevenin circuit model, is calibrated by using a laboratory test setup which is realized in this work. Battery model chosen is well-known in literature. Nowadays, there is a lack of investigation of the battery performances when it is after the EOL in automotive field. This work provides more information as possible about battery performance after EOL, analyzing strengths and weaknesses during charge and discharge phase. Performed activities are based on real experimental data from testing four lithium-ion batteries of the same manufacturer but at different SOH. Finally, a battery virtual model is realized and implemented in Matlab/Simulink [70][71].

- This work proposes a development of a novel methodology to diagnose battery SOH by fast EIS measurements [65], addressed to embedded applications. This was achieved by realizing a low cost, low energy consumption, and low test time hardware PRBS generator [72]. A large number of experimental EIS tests are performed at four EOL cells with different SOHs [73]. Impedance measurements on cells under test are extracted by performing EIS tests at various SOCs and different excitation current amplitudes. By experimental results, it's possible to obtain a reliable correlation between SOH and impedance measurements. To achieve this, peculiar frequency points, in which the impedance measurements dramatically change at

different cell SOH, will be obtained. This was possible by clustering the set of cell impedances, measured at different SOH, in rectangular areas defined in Nyquist diagrams (SOH clusters) [74].

The remainder of this paper is structured as follows. Section II describes the state-of-art battery model used in literature and novel models proposed in this PhD thesis. Section III describes SOC estimation based on several model adaptive Kalman filters. Section IV describes the novel method proposed for a real-time evaluation of battery SOH, based on impedance measurements obtained by fast EIS test.

Chapter 2

Battery modeling

Various battery models, previously presented in the literature, are discussed in this chapter. The most commonly used battery models including the electrochemical, data-driven and based on electrical equivalent circuit models are compared in [75][76], focusing on their strengths and weaknesses. In this PhD thesis, particular attention is dedicated to the electrical equivalent circuit (EEC) battery model-based. These types of models should solve trade-off between accuracy and computational complexity in simulating electrical battery behaviors. Time-domain, frequency-domain models and parametrization techniques are presented in the next section. Finally, a novel automotive EOL battery model, so ready for a possible second use, based on EEC model with aging behavior is presented and implemented in Simulink platform. Model parameters are extracted by testing cells with different aging levels obtained in controlled testing conditions.

2.1 Which battery model to use? An overview

The battery models presented in literature mainly fall into the following three main categories:

- EEC models [9][77]
- Black box models or data-driven approach [78]-[80]
- Electrochemical models [81][84]

By using data-driven approach, battery is considered as a black-box model. Several battery physic behaviors, such as electrical, thermal, mechanical and aging can be represented as probabilistic models: Markov process [21], Gaussian process [58], Hammerstain-Wiener systems [78] are proposed in literature. Otherwise, non-probabilistic models, such as neural network [79], support vector machine [80] are more considered. Although the data-driven approaches have good performance to represent non-linear phenomena problems, they are easily influenced by training data-sets, as previously mentioned. It is important to consider that the chemical-physical properties and performance of a battery depend on a wide variety of external and internal factors: SOC, SOH, current C-rate, direction of current and temperature. Hence, this approach needs a large data-set to obtain an accurate prediction of battery state.

Model-based approach, i.e. the knowledge of internal working structure of the process represented by mathematical models, is a technique more and more diffused to represent battery physic behaviors. Battery can be modeled by using lumped parameters, in particular by using EEC models, or by partial differential equation (PDE), building an accurate electrochemical battery model. Many EEC battery models presented in literature does not take into account the internal phenomena which affect battery performance and safety. In electrochemical models, lithium concentration and its electrical potential dynamics are analysed to have an accurate description of the physical-chemical processes of the battery. Usually, electrochemical models that are used on the engineering level mostly rely on the standard Newman's approach. In the research work [81], the anode and cathode of the cell are represented as porous electrodes composed of numerous spherical particles, and the spaces between particles are filled with the electrolyte, as shown in Figure 2.1. The concentration and potential distribution of the lithium-ion in the electrolyte liquid phase, and in the solid phase of the electrode material particles (spherical), are described by a two-dimensional model. The mentioned model is composed of several coupled PDEs, so as to comprehensively examine the main reaction and side reaction rates inside the cell. Since the Newman's model [81] contains a large number of PDEs, it is necessary to simplify this model from the perspective of implementation of real time systems. Reduced-order electrochemical battery model is proposed in [82]. Research work [83] proposes a coupled electrochemical-mechanical battery model. Another drawback of the Newman's model consists of lack to capture some of nanoscale phenomena. As nanoscale phenomena that indeed drive electrochemical and transport phenomena as well as determine the extent of side reactions, hotspots, shocks and fractures are not captured adequately. Hence, the evolution of lithium concentration and distribution can only be predicted very roughly. In OBELICS project, advanced modeling framework inspired by Newman's approach is proposed [84]. This technique is characterized by a more consistent virtual representation of the electrode topology. Although exist in literature scalable and reduced electrochemical models addressed to real-time systems, a large number of unknown variables need to be identified by using expensive facilities and specific tests. Consequently, it is needed to simplify the model even more, considering any boundary conditions and accept a slight decrease in terms of accuracy in the estimate. Electrical lumped parameter battery models can represent a simplification of electrochemical models.

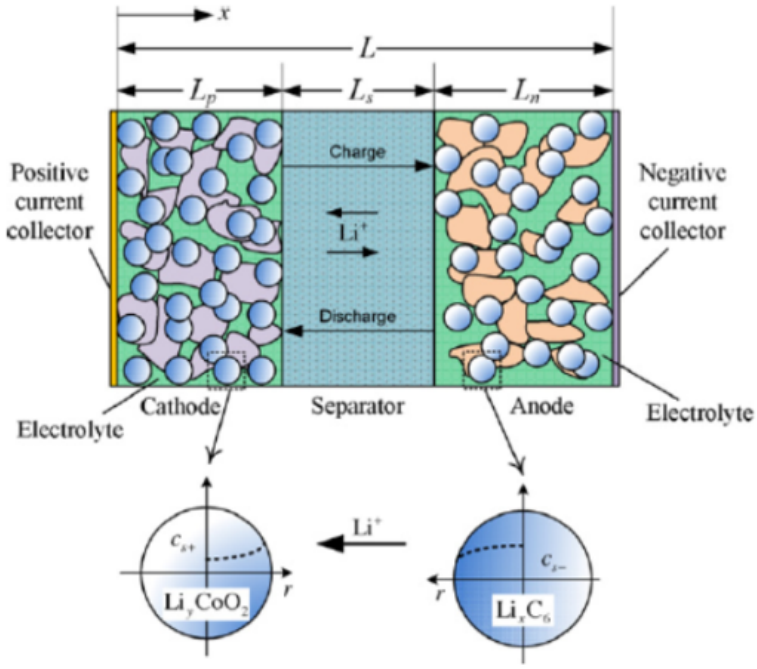

Figure 2.1: Electrochemical model rapresentation according to Doyle-Newman's approach [82].

2.2 Electrical equivalent circuit (EEC) battery model based

The EEC models are the most commonly used in real-time applications, due to their simplified model structure and easy to be identified. EEC models use electrical components to mimic the battery electrical, thermal and mechanical behaviors. In literature, the EEC models can be divided into two groups:

- **Integral-order models:** usually used to represent battery behaviors in time-domain.
- **Fractional-order models:** usually used to represent battery behaviors in frequency-domain.

2.2.1 Integral-order EEC models

Battery model based on EEC is composed of passive elements, such as resistors, capacitances, inductors and of active elements, such as diodes, voltage and current generators. Depending on model accuracy and computational efforts, various EEC battery models have been proposed in literature and are explained as follows.
Battery is a real voltage supply, hence, it could be represented by an ideal voltage generator (OCV) in series with an ideal resistance (R_{int}), as shown in Figure 2.2. As noticeable in every battery data-sheet, voltage depends on state of charge (SOC).

$$OCV = f(SOC) \tag{2.1}$$

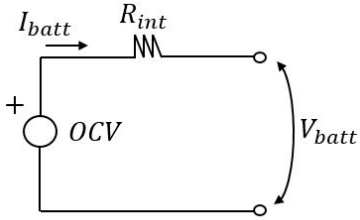

Figure 2.2: Classical Thevinin's circuit representing battery voltage response with input current.

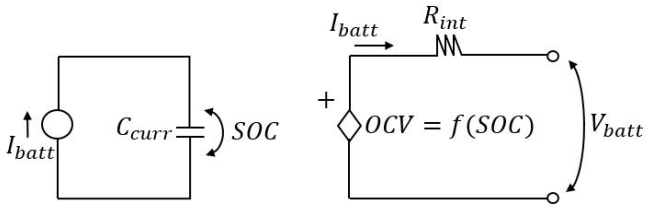

Figure 2.3: Battery model with OCV-SOC dependence.

An example of OCV-SOC relationship is shown in Figure 1.12 for different lithium-ion cell-based types. Battery SOC can be calculated by using Ampere-hour counting method, referring to Eq. (2.1). Therefore, a second Thevenin circuit is proposed and it's shown in Figure 2.3. The OCV depends on SOC value, which is represented by the voltage measured on the left circuit. This last circuit is a fiction electric network: the capacitance is not dimensionally equivalent to the real ones. Moreover *SOC* variable is a dimensionless value in the range [0,100], numerically equal to the cell's SOC itself. The OCV-SOC curve doesn't change at different temperatures. Research work [33] demonstrated that there is a slight difference (10 mV) between OCV-SOC curves measured at room temperature range [-10,50] °C. On the other hand, the OCV-SOC curve changes its value with aging, as it will be seen by the experimental test results shown in the next sections. During the charging phase, a cell behaves in a different way from the discharge, and viceversa, along the charge and discharge curves. In [85] it is noticeable the OCV difference between charging and discharging curves, due to the hysteresis behavior which battery has, especially for LFP cathode type. This is because diffusion of lithium-ion particles occurs differently during charging and discharging phase. Concerning hysteresis phenomena representation in EEC based models, two parallel voltage generators, one for charging and the other for discharging, are used. To use the correct generator, two diodes are inserted in series with the generators, so as to allow conduction only to the diode directly polarized, as shown in Figure 2.4. In this last circuit, a novel resistance R_{self} is inserted in parallel with voltage generators. R_{self} denotes the battery self-discharge resistance. Self-discharge phenomena represent the battery energy loss, per days, due to internal chemical reactions of the battery during the rest phase. In the circuit shown in Figure 2.4, when the battery is disconnected by electrical load, a part of current flow into the self-discharge resistance R_{self}, hence a part of battery SOC is proportionally lost.

R_{self} is evaluated with the highest values for LIB. Hence the effects of R_{self} can be normally neglected when analysing short time tests and can be observed only when considering very long time-span.
Referring to battery models shown in Figure 2.2-2.4, the Thevenin models connect in series a number N of parallel RC groups, describing the dynamic characteristics of the battery. Since battery is disconnected by electric load, the voltage increases its value similar to the charging of a capacitor (ohmic-capacitive effect). The most common models found in literature present one RC group, as in [77][86], two RC groups, as in [27][85], three RC groups, as in [87] and a more generic N-RC groups, as in [88] and shown in Figure 2.5.
Increasing the number N of RC groups, it's possible to analyze and represent various dynamics of battery voltage, enhancing the model accuracy. However, given the relatively low complexity required by automotive online control algorithms, no more than two RC groups are adopted for most applications.
Battery model considered in 2.5 could be classified as a linear and time-invariant (LTI) dynamic system. However, an accurate battery model should have several non-linear properties. OCV is related with SOC by non-linear features, having a flat or linear portion in the middle of SOC window, and exponential trend at the extreme of SOC window in lithium batteries as LFP [85], NMC [89], NCA [90] types. Moreover, the hysteresis behavior, especially detected in LFP cell, is represented by non-linear equations. Finally, external and internal factors, such as temperature, SOC and aging impact on circuits elements in Figure 2.5 like OCV, R_{int}, R_1, C_1,...,R_N, C_N.

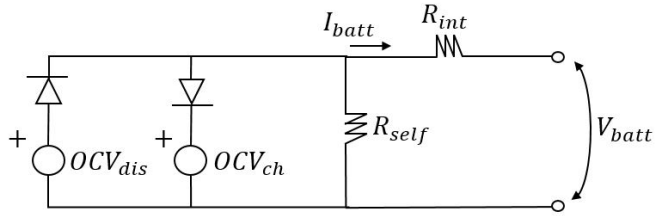

Figure 2.4: Battery model with OCV dependence with current sign (charging, discharging phase).

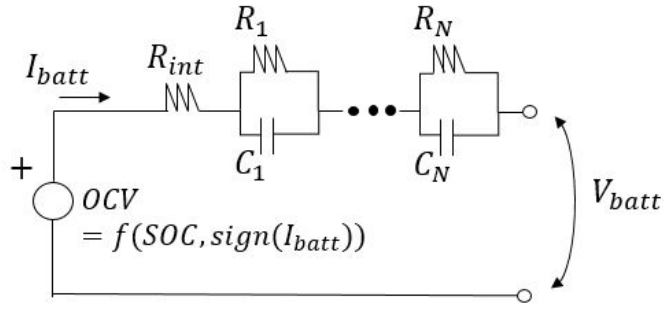

Figure 2.5: Battery model represented by N-order Thevenin circuit.

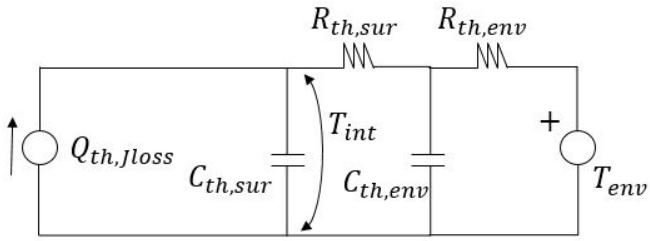

Figure 2.6: Thermal battery model based on ECC).

Considering the influence of the battery model parameters by temperature, some papers have dealt with the simultaneous real-time estimation of both the battery thermal and electrical behaviors. The development of a thermo-electrical model based on coupled ECC models is discussed in references [33][91]. Since thermal and electrical dynamics represent exchanges of energy flows, battery thermal behaviors can also be represented by using electrical circuit components. This is possible associating the temperature difference to the potential difference of two sources on a conducting body. Hence, the heat flow exchange between two sources can be associate with the electrical current flow. An example of a lumped thermal battery model based on ECC is represented in Figure 2.6. In [92] the equivalence of thermal electrical and electro-mechanical is discussed. The internal core temperature T_{int} is evaluated by the internal heat generation, which is approximated by a concentrated source of Joule loss in the battery core. The internal heat generation due to Joule loss is represented by an ideal current generator $Q_{th,Jloss}$. Heat exchange dynamics between the core and the surface are modeled by heat conduction over a thermal resistance, $R_{th,sur}$, and by thermal capacitance $C_{th,sur}$. The same circuit is represented to simulate the heat exchange between surface and surrounding temperature, given the parameters $R_{th,env}$ and $C_{th,env}$. Another methodology to define a battery thermo-electrical model is based on the use of 2-D look-up tables [77] to be calibrated offline, which calculates battery model parameters related to the actual SOC and surrounding temperature.
Considering the influence of the aging behaviors on battery model parameters, it's important to distinguish the concept of cycling aging and calendar aging of a battery. The cycling aging or cycle life is connected to the period of use of the battery based on charging/discharging cycles. Instead, the calendar aging is linked to the storage phase. Battery is in rest conditions and not in use, but, despite this, it suffers from an irreversible loss of capacity, hence, it is subject to degradation [93]. In this PhD thesis, focus is dedicated to the study of the performance of the battery with cycling aging. To have a complete analysis of the aging electrical parameters of the battery, it's fundamental to perform cycle life tests at different room temperatures, depth of discharge (DOD), and current C-rates. Recalling the last one operating condition, fast charging is one of the most important factors which impact on battery degradation [94]. Based on these influence factors, a complete cycle life model has been developed for LFP cell [9], which is able to predict the battery cyclability accurately. Other interesting cycle life models build for different chemistries, such as LFP, NMC and NCA are represented in [21][53][59]. All the cycle life battery models cited are evaluated considering the capacity rated in the range of [80,100]%. Currently, there is a lack of investigation of the performances of

the EOL batteries for a possible second use. In the next section, the first innovative contribution of this PhD thesis is shown: an electrical lithium-ion battery performance model for second life applications is identified, based on experimental data, and build in Simulink platform. The novelty of this work consists of the analysis and the identification of an EOL battery, analysing strengths, weaknesses. After post-processing of experimental data, it will be possible to understand if the battery could be used for less-demanding applications, such as stationary applications, where reduced performances are still acceptable.

2.3 20 Ah NMC pouch cell (EIG) model based on EEC with aging

In this section, EOL battery performances are analyzed in terms of energy stored and power availability. Battery under test is a Li[NiCoMn]O2-based Cathode type (briefly called NMC) pouch cell, having a nominal capacity of 20 Ah and voltage 3.65 V [95]. A set of four EOL, or second life, NMC cells of the same manufacturer, but at different SOH is considered for experimental tests. The characterization tests considered are according to the battery standard tests described in the OBELICS works [17][18]. These tests are the most important towards the modeling of a second life battery model, analysis of the performances, and the aging. Characterization tests on the batteries are performed by using a customized battery laboratory test bench, which has been realized in this PhD activity. The scope of this section is to provide more information as possible about battery performance after EOL. To achieve this scope, the second life battery virtual model, with aging property, is realized and implemented in Simulink. The battery model is based on an electrical equivalent Thevenin circuit, in which parameters are extracted by an appropriate parameter identification algorithm during the characterization tests. Hence, this section provided a battery performance model that could be simply built in some simulation platforms, analyzing battery second use in some less-demanding applications.

2.3.1 Battery cell under test

As mentioned previously, the battery under test is a lithium polymer NMC-cathode pouch cell type, having a nominal capacity of 20 Ah and 3.65V, coming from the EIG manufacturer [95]. A picture of the battery cell under test is shown in Figure 2.7. The main mechanical and electrical characteristics of this cell are shown in Table 2.1, while the operating conditions are shown in Table 2.2.
To build an electrical battery performance model with aging behaviors, a set of five EIG cells is considered. One of the five cells is considered as at the beginning of life (cell #0, the fresh cell). The other four cells have been cycled until they have reached EOL (SOH$<$85%), and beyond. The EOL cells (#3, #4, #5, #8) were subjected to 4 different cycle life tests. Tests were composed by constant-current (CC) and, finally, constant-voltage (CV) charging current rate C/2; followed by discharging phases, separated with rest period, at a room temperature of 35°C. A summary of these cycle life tests is presented in Table 2.3. Cycle life tests were carried out in ENEA research center from 2015 to 2017. More details about these tests are shown in [96][97] and in Figure 2.8. Afterward, the cells have not been used for about 2 years, and have been stored in the same conditions (in a not

thermally controlled environment). This is a good idea to analyse the realistic effects of battery degradation due to continuous use and long period of rest.

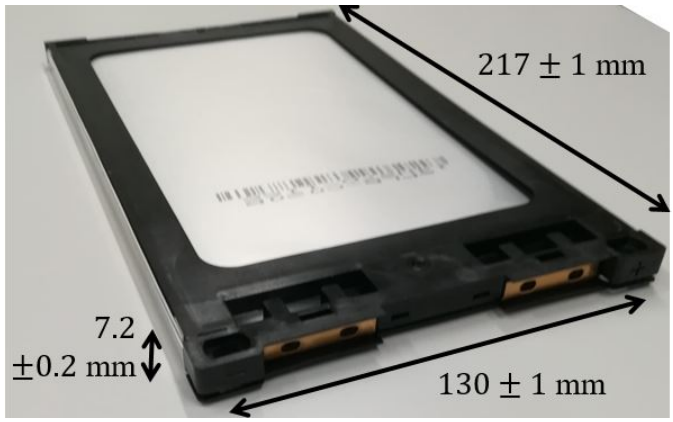

Figure 2.7: EIG C020 lithium polymer battery cell.

Mechanical		**Electrical**	
Length	217.0 ± 1 mm	Nominal voltage	3.65 V
Width	130.0 ± 1 mm	Nominal capacity	20 Ah
Thickness	7.2 ± 0.2 mm	Specific Energy	170 Wh/kg
Weight	426 g	Energy density	360 Wh/L
		Specific power (DOD 50%, Pulse 10 s)	2300 W/kg
		Power density (DOD 50%, Pulse 10 s)	4600 W/L
		AC impedance (1kHz)	<3 mΩ

Table 2.1: Main characteristics of EIG C020 cells

Charging phase		**Discharging phase**		**Temperature**	
Standard Charging method	CC/CV	Lower voltage limit for discharge	3.0 V	Operating temperature	-30°C/ +55°C
Max voltage limit	4.15 V	Lower voltage limit	2.5 V	Operating temperature in charging phase	+0°C/ +40°C
Recommended charge current	C/2	Max discharging current (continuous)	5C	Storage temperature	-30°C/ +55°C
		Max peak discharge current	10C		

Table 2.2: Operating conditions of EIG C020 cells

Battery n.	Discharge C-Rate	DOD	Performed number of cycles	Last capacity estimated
#0	/	/	/	20.00 Ah
#3	3	80-20%	2550	15.14 Ah
#4	5	80-20%	2000	15.09 Ah
#5	1	90-10%	2400	12.91 Ah
#8	3	90-10%	1600	15.48 Ah

Table 2.3: Cycle life test performed at ENEA research center [96].

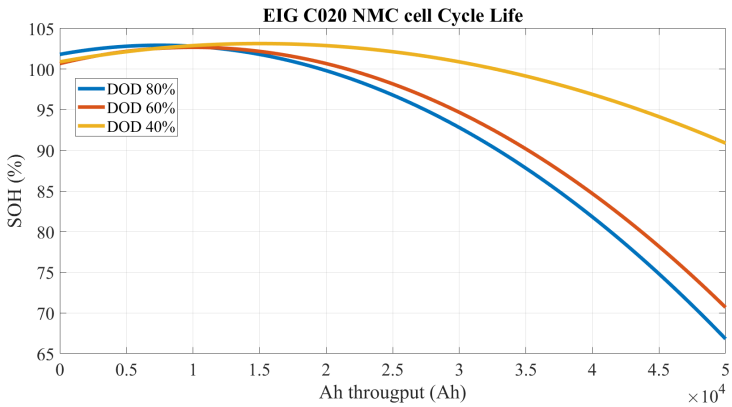

Figure 2.8: EIG C020 lithium polymer battery cell.

2.3.2 Laboratory test setup

Characterization tests on the five cells overcited are performed by using a customized battery laboratory test bench developed in the University of Florence. This test bench was builded to achieve some goals of this PhD activity. A picture and a schematic of the laboratory setup is shown in Figure 2.9 and 2.10.
The idea consists of the development a switched electronic load/feeder which performs continuous charging/discharging cycles on the battery under test. This battery test bench is made up by an electronic load (Rigol DL3021) and by an electronic feeder (DSC-Electronics DP15-60H), which characteristics are summarized in Table 2.5. The overcited instruments control the battery in current and give to the user the possibility to programm customized charging/discharging test, for example, driving cycle test, at minimum step time of 1 s. Charging and discharging current profile can be programmed on the Rigol and DSC by host PC using Labview platform. Battery current, voltage, surface temperature and surrounding temperature are acquired by the DSPACE MicroLabBox DS1202 at different sample times: 0.1 s for voltage and current acquisition and 60 s for temperature. In particular, battery current measurement is performed by using a shunt sensor, class 0.5 and full scale 40 A. Then, the signal measurement is processed by an analogic circuit, essentially composed by an instrumentation amplifier (INA 128). Battery voltage measurement is performed by using the 16bit ADC of DSPACE. The informations about voltage and sensor's accuracy are shown in 2.4.

Parameter	Symbol	From	Value
Shunt sensor's accuracy	$e_{sh,V}$	Data-sheet	375 uV
Shunt sensor's gain	K_{sh}	Data-sheet	1875 uV/A
Current measurement uncertainty from shunt sensor	$e_{sh,A}$	$\frac{e_{sh,V}}{K_{sh}}$	200 mA
INA128 offset voltage	$b_{ina,V}$	Data sheet	10 uV
offset current measurement error (shunt coupled with INA128)	$b_{ina,A}$	$\frac{b_{ina,V}}{K_{sh}}$	5.33 mA
INA128 gain voltage error	$G_{ina,\%}$	Data-sheet	0.05%
DSPACE 16bit ADC offset voltage	$e_{16bit,V}$	Data-sheet	3 mV
DSPACE 16bit ADC gain voltage error	$G_{16bit,\%}$	Data-sheet	0.15%

Table 2.4: Measurement instrument's accuracy and evaluation of impedance measurement's uncertainty.

The maximum and minimum drop voltage estimation measured on nominal impedance R_{nom} is approximately given by the current excitation I_{nom} and by following equations:

$$V_{max,err} = e_{16bit,V} + (1 + \frac{G_{16bit,\%}}{100})(1 + \frac{G_{ina,\%}}{100})(I_{nom} + e_{sh,A} + b_{ina,A})R_{nom} \quad (2.2)$$

$$V_{min,err} = -e_{16bit,V} + (1 - \frac{G_{16bit,\%}}{100})(1 - \frac{G_{ina,\%}}{100})(I_{nom} - e_{sh,A} - b_{ina,A})R_{nom} \quad (2.3)$$

it is assumed that the impedance value of battery under test is around [1,10] m/$Omega$ and the battery is excited with a nominal current of 10A. Drop voltage obtained is around [10,100] mV. By using (2.2) and (2.3) impedance uncertainty is obtained:

- **1 mΩ measured at 10 A:** Nominal voltage: 10 mV, max. voltage estimation error: 13.21 mV, min. voltage estimation error: 6.77 mV, relative error: 32.0%.

- **10 mΩ measured at 10 A:** Nominal voltage: 100 mV, max. voltage estimation error: 105 mV, min. voltage estimation error: 95 mV, relative max. error: 5.0%.

The DSPACE MicroLabBox control the charging/discharging phase switching the appropriate power circuit, hence the appropriate contactors (SW60P Albright). To guarantee a sufficient power excitation, the 12 V relay module channel, interfaced to Arduino, is employed between the DSPACE and the contactors. Further instrumentation mentioned is depicted in Figure 2.11. In conclusion, the DSPACE device saves measurement data and manages the charging and discharging circuit, controlled by Host PC via Ethernet, through a code developed in Simulink platform.

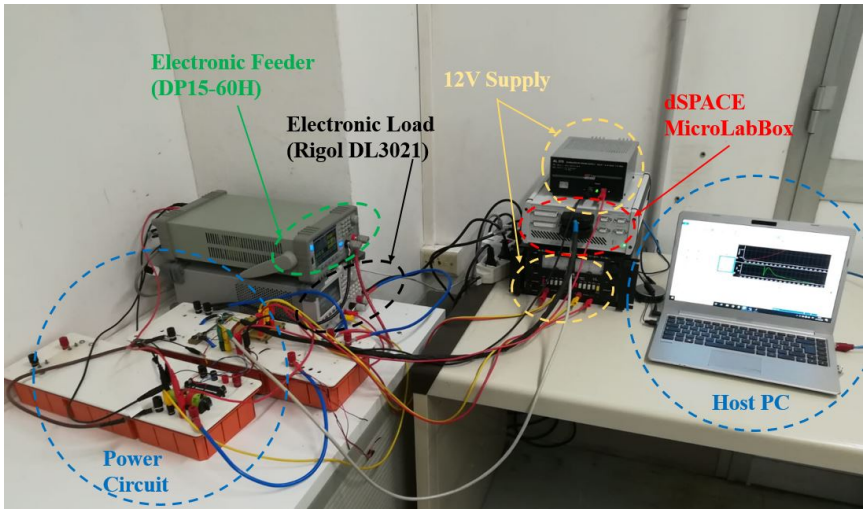

Figure 2.9: Laboratory test setup: picture.

Rigol DL3021		**DSC Electronics DP15-60H**		**DSPACE MicroLabBox**	
Max power	200 W	Max power	900 W	Processor	2 GHz dual-core and user--programmable FPGA
Max voltage	150 V	Max voltage	150 V	Analog Input	8 differential 14-bit (10 Msps) channels
Max current	40 A	Max current	60 A	Analog Output	16 16-bit (1 Msps) channels
Channels	1	Channels	1	Digital pins	48

Table 2.5: Brief description of the laboratory equipment used

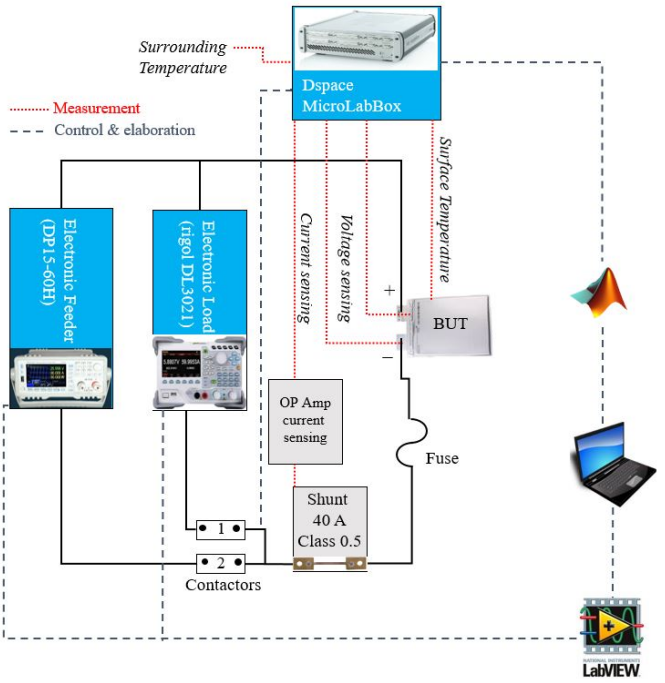

Figure 2.10: Laboratory battery test setup: schematic.

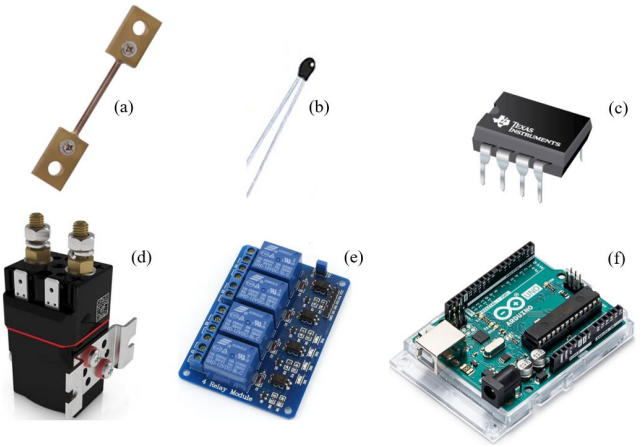

Figure 2.11: Further components which makes up the battery test bench. (a) Shunt sensor (40A, 75 mV), (b) radial NTC thermistor, (c) Instrumentation amplifier INA 128, (d) SWP60 Albright contactor, (e) 12 V relay module four channel, (f) Arduino uno.

2.3.3 Test methodology

The battery cells were characterized by a set of subsequent performance tests, which aim to collect the necessary data to parametrize the battery EEC model described in Figure 2.5. Since the cells in EOL show different capacity values, every battery is excited with a different current amplitude. Moreover, in this part of work the C-Rate current 1C value refers to the maximum available capacity of the cell in the EOL state, 16 Ah, which corresponds to the 80% of SOH. This assumption is taken because second life applications, as shown in [10]-[12], require low discharging current performance, in order to maintain a long service time. The following characterization tests are performed on batteries:

- **Preconditioning test:** The preconditioning test is made up of three full charge/discharge cycles at fixed C-rate current C/4 (i.e. 4 A), interspersed with a pause of 1 h between discharging and charging phase. The charging phase is performed considering the CC and CV phase. A 14 h rest is undertaken that one cycle is completed.

- **Capacity test:** In the capacity test, battery maximum stored capacity and coulombic efficiency are estimated. The capacity of the battery represents one of its most important parameters. Indeed, it not only provides an indication of the battery energy stored, but its value is necessary to define the most important battery internal states, such as SOC and SOH. A nominal capacity is always given by the manufacturer, however this value decreases with aging or unexpected events. The capacity test is made up of three full discharge/charge cycles, maintaining a charging C-Rate of C/3 (first in CC mode, finally in CV mode), changing the discharge C-Rate of C/2, C/3 and C/4. This is because battery capacity extracted during discharging phase depends on the discharging C-rate current imposed, as shown in every battery datasheet. Rest time values are equals to preconditioning test.

- **Pulse test:** This test allows the analysis of the performance of the battery in terms of power efficiency. Moreover the proper identification of the EEC model parameters (Figure 2.5) by exciting the battery with charging/discharging current pulses. In order to have an accurate model, pulses must be performed across the whole battery SOC range, and testing the overcited EOL cells at different SOHs. Pulse test procedure is described as following. When the battery is fully charged, it is excited by a series of fourteen C/2 discharged current pulses, separated by 30min of rest period. Each pulse discharges the 7% of battery capacity, until the lower threshold voltage is reached (3.0 V). Then, after a rest of 14 h, pulse charging test is performed, which is set as discharge pulse test, reaching the higher threshold voltage (4.15 V) in CV mode.

The characterization tests are automatically performed by laboratory test bench shown in Figures 2.9, 2.10, and controlled by host PC. As mentioned previously, charging and discharging current profiles are given by the DSC Electronics DP15-60H Rigol DL3021, which are controlled by host PC using Labview sotware platform. An example of the user interface created in the host PC is shown in Figure 2.12. The DSPACE MicrolabBox controls the power circuit thanks to a real time model, which is build in Simulink R2017a (RTI-DSPACE) and then deployed to the hardware. The test protocol real-time model is depicted in Figure 2.13. By using

ControlDesk platform, battery tester control panel is developed, in order to choose and customize the characterization test setup, as shown in Figure 2.14. Preconditioning, capacity and pulse test are automatized test clicking on Automatic test and setting the appropriate options. Manual test consists of switching on manually charging or discharging power circuit by using the options in the control panel.

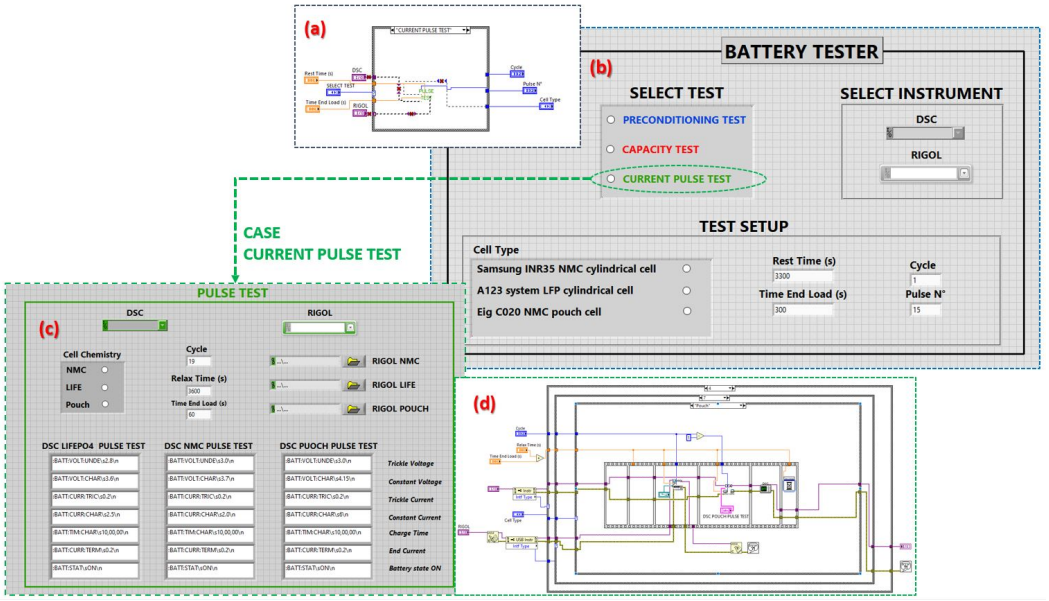

Figure 2.12: Framework of the battery lab test bench control panel in Labview: (a) Main block diagram and (b) control panel; (c) Pulse test control panel and (d) block diagram.

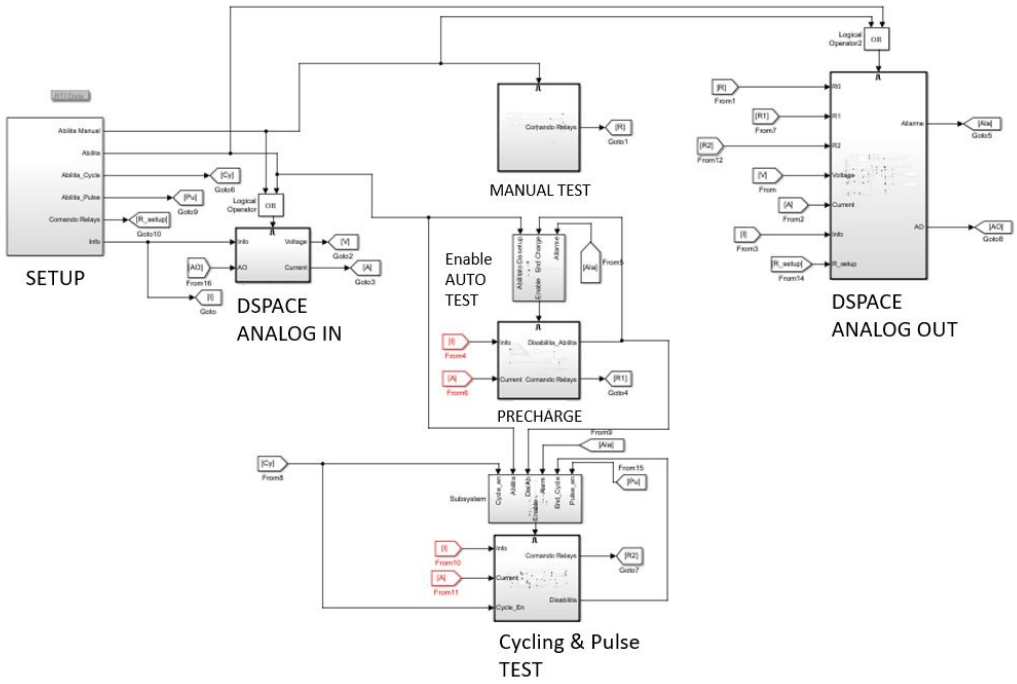

Figure 2.13: Framework of the battery lab test bench control in Simulink, ready to deploy in the DSPACE device.

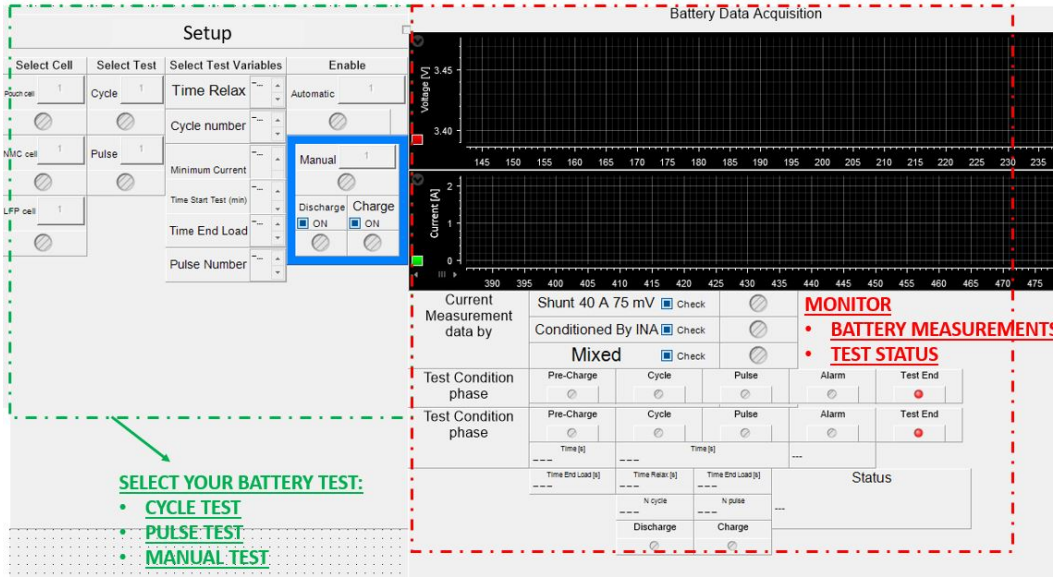

Figure 2.14: Battery test bench control panel.

2.3.4 Models parameter extraction

Battery model adopted in this work is a 2^{nd}-order Thevenin EEC represented in Figure 2.15.
Given an input current I_{batt}, the battery voltage response is calculated by the following differential system equation:

$$\begin{cases} \dot{v}_1 &= \dfrac{v_1}{R_1 C_1} - \dfrac{I_{batt}(t)}{C_1} \\ \dot{v}_2 &= \dfrac{v_2}{R_2 C_2} - \dfrac{I_{batt}(t)}{C_2} \\ V_{batt} &= OCV - v_1 - v_2 - R_{int} I_{batt} \end{cases} \tag{2.4}$$

Where v_1 and v_2 denote the voltage drop across the capacitors C_1 and C_2. As mentioned previously, circuit parameters change their value at different battery operating conditions and internal states, such as various SOC and SOH.
The SOC corresponds to the ratio of the stored battery capacity (the cumulate current supplied/delivered by the battery) with respect to the current battery capacity (C_{curr}). This assumption is in according to Ampere-counting method (equation (1.1.)). In this PhD thesis, SOH value is based on a comparison of the current capacity evaluated with a standard cycle (C_{curr}) with the nominal capacity at the beginning of life (C_{nom}). The SOC and SOH evolutions are represented by the following system equations:

$$\begin{cases} \dot{SOC} &= -\dfrac{I_{batt}}{3600 C_{curr}} \times 100 \\ SOH &= \dfrac{C_{curr}}{C_{nom}} \times 100 \end{cases} \tag{2.5}$$

In this section, it's depicted how to estimate the battery circuit parameters (OCV, $C_{curr}, R_{int}, R_1, R_2, C_1, C_2$) of the models (2.4) and (2.5) by characterization tests. In the capacity test, it's possible to evaluate battery capacity and determine the relative SOH. An example of complete capacity test performed by the laboratory battery test bench is shown in Figure 2.16, where, giving the appropriate current profile, the battery voltage is observed. Considering the adoption of the generator convention in the battery model shown in Figure 2.15, the discharging phase is associated to negative sign of the current, viceversa to the charging phase.

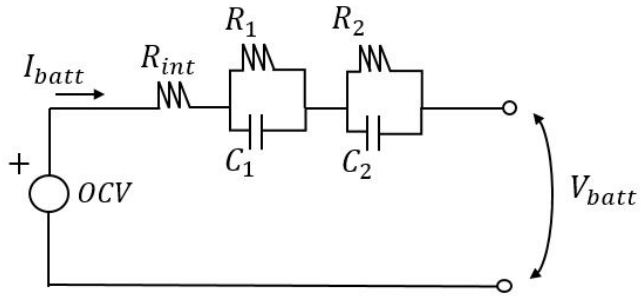

Figure 2.15: Battery model represented by 2°-order Thevenin circuit.

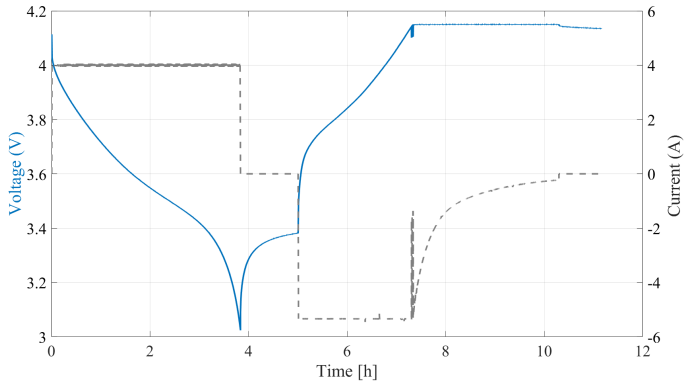

Figure 2.16: Capacity test.

Using the Ampere-counting method, battery capacity C_{curr} is in according to (2.6), calculating the integral of battery current during the test. The capacity is separately evaluated in charging or in discharging phase:

$$C_{curr} = \frac{1}{3600} \int I_{batt}(\sigma) d\sigma \tag{2.6}$$

Performing the pulse test, battery is excited with discharging or charging constant current. An example of complete discharging pulse test performed by laboratory battery test bench is shown in Figure 2.17. Each pulse discharges or charges 7 % of the battery cell SOC, until the minimum or the maximum threshold voltage is reached (3.0 V, 4.15 V). Pulses are separated by 30 minutes of rest period.
Open circuit voltage and impedance parameter values are extracted by observing voltage relaxation in the rest phase, as noticeable in Figure 2.18. The internal resistance R_{int} value is acquired from the sudden drop voltage $V_{batt,drop}$ due to current pulse amplitude I_{pulse}:

$$R_{int} = \frac{V_{batt,drop}}{I_{pulse}} \tag{2.7}$$

The second extracted parameter is the the open circuit voltage OCV, obtained as the last voltage value acquired in the rest period. RC-group parameters (R_1, R_2, C_1, R_2) are estimated by fitting the voltage relaxation curve observed in the rest period, recalling the model (2.4):

$$OCV - V_{batt} = v_{1,drop} e^{-t/\tau_1} + v_{2,drop} e^{-t/\tau_2} \tag{2.8}$$

Where τ_i denotes the time constant of the i^{th} RC group considered.
The fitting process is carried out in Matlab, using the curve fitting toolbox (CFT), where parameters $v_{1,drop}$, $v_{2,drop}$, τ_1 and τ_2 are extracted using the bounded-parameter Trust-Region algorithm. Finally, R_1, R_2, C_1, R_2 parameters are calculated in according to the following equations:

$$R_i = \frac{v_{i,drop}}{I_{pulse}} \tag{2.9}$$

$$C_i = \frac{\tau_i}{R_i} \tag{2.10}$$

The presented procedure is performed both for the pulse discharging and pulse charging tests. The extracted parameter datasets for the novel second-life battery model are tabulated in the entire SOC range and SOH of [85-50] % by testing the cells overcited.

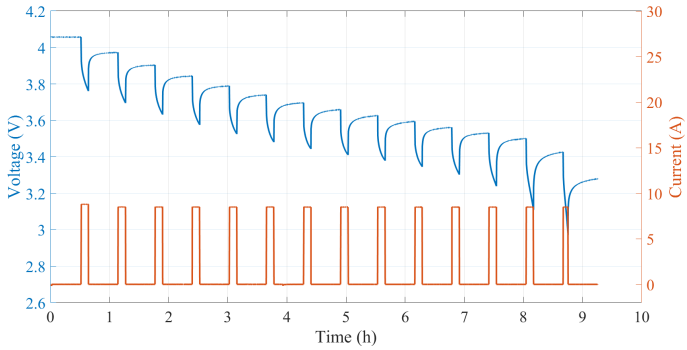

Figure 2.17: Discharging pulse test.

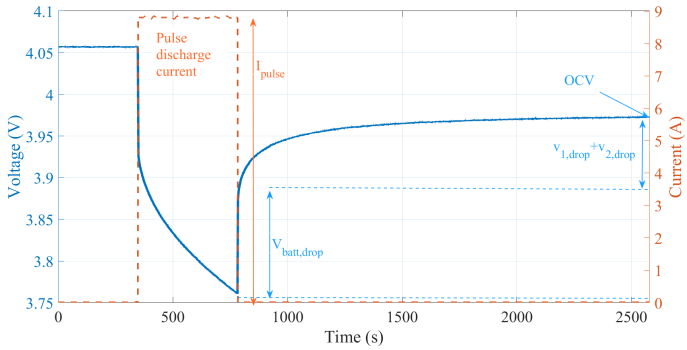

Figure 2.18: Model parameters extraction procedure for a discharging pulse.

2.3.5 Model implementation

The aim of this work consists of the development of a virtual electrical battery model with aging: given an input current, battery model estimates the evolution of battery voltage and SOC. Voltage and SOC evolution are based on time-continous system equations (2.4) and (2.5). Model parameters change their values at various SOCs and SOHs and sign of the current. Hence, 3-D look-up tables (LUTs) are needed to correlate model parameters. The calibration of the 3-D LUTs is performed by characterization tests depicted in the previous subsection. In summary, electrical battery model with aging is defined by the following differential system equation:

$$\begin{cases} \dot{SOC} & = & -\dfrac{I_{batt}}{3600 C_{curr}} \times 100 \\ \\ \dot{v}_1 & = & \dfrac{v_1}{R_1 C_1} - \dfrac{I_{batt}(t)}{C_1} \\ \dot{v}_2 & = & \dfrac{v_2}{R_2 C_2} - \dfrac{I_{batt}(t)}{C_2} \\ \\ OCV & = & f_{ocv}(SOC, SOH, sign(I_{batt})) \\ R_{int} & = & f_{R_{int}}(SOC, SOH, sign(I_{batt})) \\ R_1 & = & f_{R_1}(SOC, SOH, sign(I_{batt})) \\ R_2 & = & f_{R_2}(SOC, SOH, sign(I_{batt})) \\ C_1 & = & f_{C_1}(SOC, SOH, sign(I_{batt})) \\ C_2 & = & f_{C_2}(SOC, SOH, sign(I_{batt})) \\ \\ V_{batt} & = & OCV - v_1 - v_2 - R_{int} I_{batt} \\ \\ \text{subject to} & & \\ \text{set} & & C_{curr},\ SOC(0) \\ SOH & = & \dfrac{C_{curr}}{C_{nom}} \end{cases} \tag{2.11}$$

As mentioned in last sections, cells under test are in EOL. The batteries's history and cycle life is shown in Table 2.3 and in Figure 2.8. More details are illustrated in [96]. However the cells have not been used for about 2 years, and have been stored in the same conditions (in a not thermally controlled environment). It's reasonable that the current rated capacity could not correspond to the last capacity estimated two years ago. Hence, the SOH considered in this model is fixed to its setup value before simulation is running. To implement the battery model in a microcontroller, time-continuous system (2.11) is discretized at the sample time T. Defining time istant $t_k = kT$, for $k = 0, 1, 2, ..., N$, system (2.11) is transformed in a time-discrete system by using Eulero approximation:

$$\dot{x} \sim \frac{x(t_{k+1}) - x(t_k)}{t_{k+1} - t_k} = \frac{x(t_{k+1}) - x(t_k)}{T} \tag{2.12}$$

Considering $x_k = x(t_k)$, time-discrete battery model is defined as follows:

$$\begin{cases} SOC_{k+1} & = & SOC_k - \dfrac{I_{batt,k}T}{3600C_{curr}} \times 100 \\ \\ v_{1,k+1} & = & v_{1,k}e^{-T/\tau_{1,k}} - R_{1,k}I_{batt,k}(1-e^{-T/\tau_{1,k}}) \\ v_{2,k+1} & = & v_{2,k}e^{-T/\tau_{2,k}} - R_{2,k}I_{batt,k}(1-e^{-T/\tau_{2,k}}) \\ \\ OCV_k & = & f_{ocv}(SOC_k, SOH, sign(I_{batt,k})) \\ R_{int,k} & = & f_{R_{int}}(SOC, SOH, sign(I_{batt,k})) \\ R_{1,k} & = & f_{R_1}(SOC_k, SOH, sign(I_{batt,k})) \\ R_{2,k} & = & f_{R_2}(SOC_k, SOH, sign(I_{batt,k})) \\ C_{1,k} & = & f_{C_1}(SOC_k, SOH, sign(I_{batt,k})) \\ C_{2,k} & = & f_{C_2}(SOC_k, SOH, sign(I_{batt,k})) \\ \\ V_{batt,k} & = & OCV_k - v_{1,k} - v_{2,k} - R_{int,k}I_{batt,k} - R_{int,k}I_{batt,k} \\ \\ \text{subject to} & & \\ \text{set} & & C_{curr},\ SOC(k=0) \\ SOH & = & \dfrac{C_{curr}}{C_{nom}} \end{cases} \tag{2.13}$$

In conclusion, after model parameters identification, battery system model (2.13) can be implemented on a simulation platform or in embedded systems. In the next section, experimental test on EOL batteries are shown and results obtained during capacity and pulse test are discussed. Finally, the battery model (2.13) is build and implemented in Simulink. The identified model is validated, in terms of voltage accuracy, by comparison between experimental and simulated data.

2.3.6 Results & discussion

The overcited test procedure was performed on the five EIG cells cited in Table 2.3. All the tests were carried out by using the laboratory battery test bench setup shown in Figure 2.9 in a not thermally controlled environment. Considering all the test performed and by measuring the room temperature, the mean and the maximum value obtained are respectively 22°C and 24°C. Concerning cell surface temperature, maximum temperature observed during the tests is 27°C.
Capacity test is composed by three charging/dischaging cycles with a discharging constant current of C/4, C/3 and C/2. The charging phase is composed by a CC charging with C/3, followed by CV charging, as illustrated in Figure 2.16. The capacity test cycles have been exploited in order to evaluate the rated capacity of the five cells. Referring to the maximum cell capacity stored in the complete C/3 charging phase, capacity of the five cells is extracted and represented in Table 2.6. The user can evaluate the coulombic efficiency by cycling batteries with different discharging current rates (C/4, C/3 and C/2). The parameter η_c denotes the coulombic efficiency, i.e., the ratio between the capacity extracted in discharging phase, at a specified C-Rate, and the capacity extracted in the standard charging phase:

$$\eta_c = \frac{C_{discharge,spec\ c-rate}}{C_{standard\ charge}} \tag{2.14}$$

Battery n.	Capacity extracted (C_{curr})	SOH
#0	20.17	100%
#3	16.07	80%
#4	17.14	85%
#5	12.38	60%
#8	10.60	50%

Table 2.6: Capacity evaluated of the five EIG cells.

Results of the battery coulombic efficiency are calculated and shown in Table 2.7, in according to (2.14). It's noticeable that the coulombic efficiency of EOL cells, with respect to the fresh cell, strongly decreases when battery discharge C-Rate increases.
Capacity test results showed interesting features by observing the voltage curve on the five cells with different SOHs, during charging and discharging phase. From results obtained in Figure 2.19, two points are highlighted. Firstly, it's noticeable a rise with aging of the CV charging phase duration. This fact is noticeable by comparing the fresh cell #0 (lower CV phase) with cell #3-#5 (higher CV phase) and cell #8 (highest CV phase duration), in according to results shown in [59] for NMC chemistries. Secondly, an increase with aging of the difference between voltage charging and discharging phase curves, due to an increase of the internal resistance with aging.
Pulse charge and discharge tests were performed, following the procedure illustrated in the previous sections. These tests have been exploited in order to extract the circuit parameters ($OCV, R_{int}, R_1, R_2, C_1, C_2$) of the battery model (2.13). As mentioned before, battery model (2.13) is implemented in Simulink, and finally, voltage model accuracy is observed by the comparison between voltage simulated and experimental data. Figure 2.20 shows the pulse charge/discharge test on cell #4 (above), and the voltage absolute error (below), defined as the difference between the measured and the simulated voltage. Results shown in Figure 2.20 denote that the battery model estimates accurately the voltage evolution when the battery SOC is in the range [10,90] %. However, at the extreme of battery SOC window, the absolute error increases, especially at the lowest SOC values. This is due to non-linear behavior that battery has at the extreme of SOC.

n.	Charge capacity	Capacity C/2 test		Capacity C/3 test		Capacity C/4 test	
	(Ah)	(Ah)	η_c %	(Ah)	η_c %	(Ah)	η_c %
#0	20.17	19.56	97.0	19.60	97.2	19.95	98.9
#3	16.07	14.71	92.5	15.09	93.9	15.96	99.3
#4	17.14	15.40	89.9	16.65	97.1	16.90	98.6
#5	12.38	11.55	93.3	11.85	95.7	12.34	99.7
#8	10.60	8.84	83.4	9.99	94.3	10.28	97.0

Table 2.7: Capacity test: Ah extracted in discharging phase and coulombic efficiency

The results of battery model identification, hence the circuit parameters extracted, are shown in the Figures 2.21, 2.22 and 2.23.
Internal resistance is extracted at different SOC, SOH, and current sign, as shown in Figure 2.21. It's noticeable an increase of R_{int} at the extreme of SOC, while remains constant in the middle of SOC window. The charging or discharging phase doesn't influence on the R_{int} value. Instead, internal resistance increases during the aging process. By Figure 2.21, the mean evaluated resistance of the new cell is 5.92 mΩ: it's evident an increase at least 200 % of the internal resistance of the EOL cells with respect to the fresh cell. Moreover, it's noticeable an increase of 470 % of the cell at SOH=50 % with respect to the fresh cell and 200% of the cell at SOH=85 %. There is a huge difference in internal resistance between battery at 60 % and 50 % of SOH. The internal resistance is inversely proportional to the battery power efficiency. By results obtained, it's possible to suggest that EOL batteries could be considered as energy storage for stationary applications, which require low performance, in terms of low charge/discharge current C-Rate. Indeed, the performance of EOL lithium batteries can be comparable to the lead-acid batteries. Moreover, results obtained in Figure 2.21 suggest that an acceptable SOH range of battery is [80,60]%.. Results in Figure 2.22 depicts a noticeable difference between OCV discharge and charge curve due to hysteresis for NMC chemistry, in according to results shown in [27] for LFP based. As previously mentioned, in this work the OCV value is evaluated as the battery voltage measured after 30 min of rest. An accurate measurement requires at least 1h of rest time. However, due to the pandemic period and rules in the laboratory, it was needed to accelerate the pulse test time duration.
Finally, an increase of OCV voltage curve during the aging process is observed, especially in charging phase. Thus an increase of the two RC-groups resistance is observed, as shown in Figure 2.23.
This work was presented in the EEEIC International Conference on Environment and Electrical Engineering in the year 2020 [70].

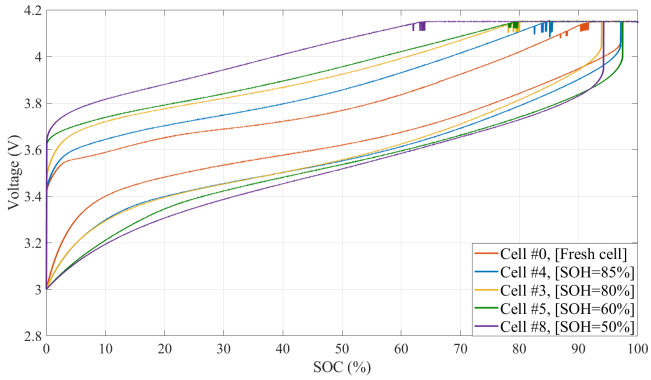

Figure 2.19: Voltage vs. capacity curve for EIG cell at several SOH during charging and discharging phase.

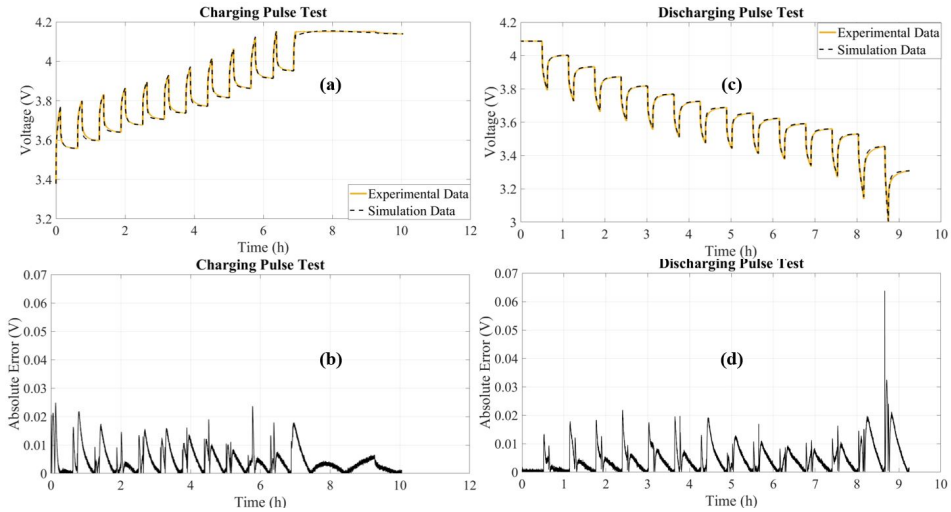

Figure 2.20: Comparison between voltage simulated and experimental data: (a) Pulse discharging test and (b) absolute error; (c) Pulse charging test and (d) absolute error.

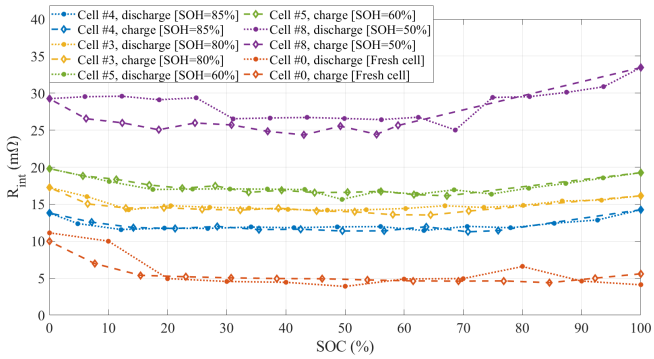

Figure 2.21: Internal resistance extraction of EIG cells at different SOHs, during charging and discharging phase.

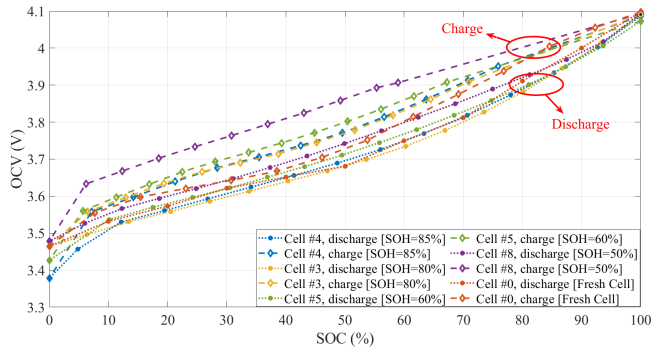

Figure 2.22: Open circuit voltage extraction of EIG cells at different SOHs, during charging and discharging phase.

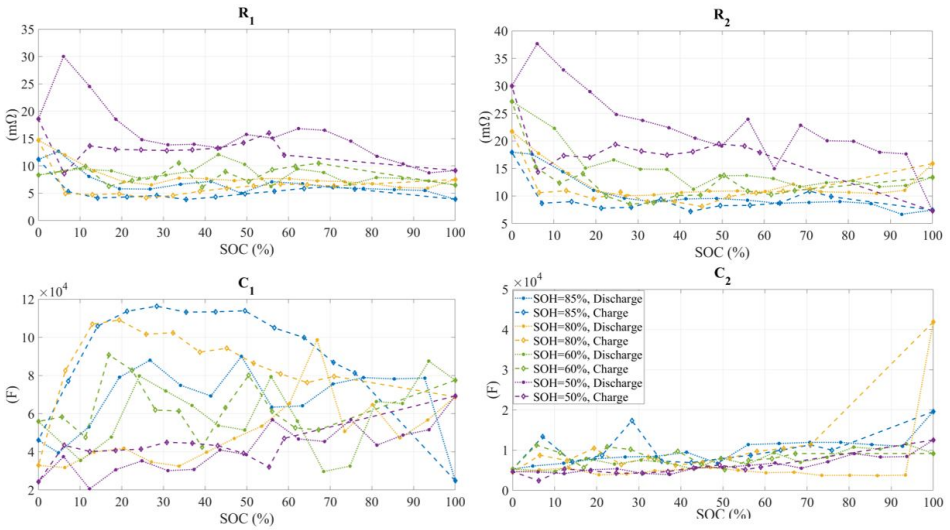

Figure 2.23: RC-group parameters extraction of EIG cells at different SOHs, during charging and discharging phase.

2.3.7 The use of retired batteries (2nd life) in stationary applications: green mobile networks

As mentioned in the introduction, the large expansion of renewable energies such as wind and photovoltaics, and the increase of the BEVs, which means a large scale production of lithium batteries, lead to consider the idea to use retired automotive batteries as support to renewable energies. The reuse of these batteries, giving them a second life, in less demanding applications has given the possibility to car and battery manufacturers to expand their portfolio and enter in new markets. From the previous experimental tests, the second life battery model is built and implemented in Simulink. This model was used in the OBELICS project: the goal of this work is to understand if the use of second life lithium batteries returns a positive credit in terms of economic cost and enviromental impact.
The object of the study is a mobile communication station, made up of a cluster of radio-base stations. The model is defined and developed in this PhD activity, for the OBELICS project [98]. The main characteristics of this model are the following:

- The system requires energy 24 hours per day, at the step time of 30 min.
- The system is typically equipped with back-up systems (e.g. battery, inverter, chargers).
- The daily user's data traffic profile per unit of area (Mbps/km^2) is provided by an Italian mobile operator [99].
- The evolution of technology makes it possible to optimize energy consumption by switching on and off an appropriate number of stations [99] and by using new transmission criteria for MIMO antennas [100].

The complete scenario is represented in Figure 2.24. It's based on the energy performance analysis of a system including a cluster of base stations, a BESS, a

photovoltaic generation unit; the system is grid-connected. Due to appropriate AC/DC and DC/DC converters, power flux is possible in a bidirectional way from and to the grid. The energy produced by PV can be used directly or stored in the battery. A preliminary analysis of the benefits of the use of second life batteries in terms of environmental impact. The CO2 emission variability due to electric energy generation in Italy is provided by Terna [101], depending on day hour and year period.
Results obtained from the defined scenario are presented in [102]. They include energy balance expected costs, concerning the reuse of EIG EOL batteries, assumed based on the Italian scenario. More details about this work are provided in the OBELICS project, Work-package 7 [98].

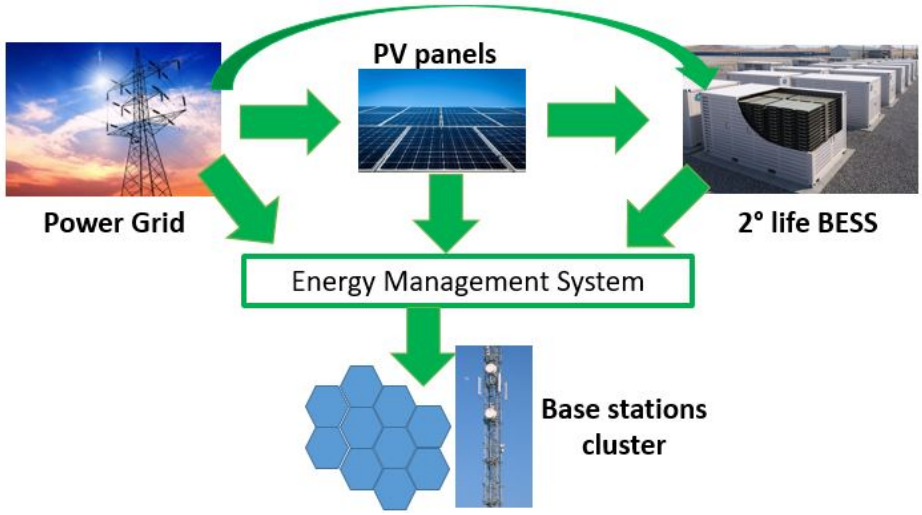

Figure 2.24: The mobile access network plant.

2.4 Fractional-order EEC models

Frequency response analysis is the technique whereby a sinusoidal excitation input is applied to measure the output response of a transfer function. In this study, battery system is considered as a linear and time-invariant (LTI) system. Since batteries show several non-linear behaviors, this analysis is performed by exciting the battery with low-energy consumption. This means that the frequency response test is performed with a series of frequency-controlled sinusoidal current amplitudes and reduced test time duration, ensuring battery LTI property. Frequency response test in the battery system is called in literature electrochemical impedance spectroscopy (EIS) test. The general principle of impedance spectroscopy is to apply a sinusoidal signal I_{batt} in current on the battery: measuring its voltage response V_{batt}, battery impedance Z_{batt} is computed by the equation:

$$Z_{batt}(t) = \frac{V_{batt}(t)}{I_{batt}(t)} = \frac{V sin(\omega t + \varphi_{batt})}{I sin(\omega t)} \tag{2.15}$$

V and I are respectively the voltage and the current amplitude, ω is the angular frequency, φ_{batt} is the phase shift. Current is maintained with low amplitudes in order to preserve the validity of LTI model assumption. In the frequency domain, it is possible to separate the impedance Z_{batt} in a real part $\mathbf{Re}(Z_{batt})$ and in an imaginary part $\mathbf{Im}(Z_{batt})$ using the following equation:

$$\begin{aligned} &Z_{batt}(j\omega) = \mathbf{Re}(Z_{batt}(j\omega)) + j\mathbf{Im}(Z_{batt}(j\omega)) = \\ &= |Z_{batt}(j\omega)|cos(\varphi_{batt}(j\omega)) + j|Z_{batt}(j\omega)|sin(\varphi_{batt}(j\omega)) \end{aligned} \tag{2.16}$$

Where impedance magnitude $Z_{batt}(j\omega)$ and phase shift $\varphi_{batt}(j\omega)$ are calculated as follows:

$$\begin{aligned} |Z_{batt}(j\omega)| &= \sqrt{\mathbf{Re}(Z_{batt}(j\omega))^2 + \mathbf{Im}(Z_{batt}(j\omega))^2} \\ \varphi_{batt} &= tan^{-1}\left(\frac{\mathbf{Im}(Z_{batt}(j\omega))}{\mathbf{Re}(Z_{batt}(j\omega))}\right) \end{aligned} \tag{2.17}$$

Usually, real and imaginary values of impedance are represented in the Nyquist plot as shown in Figure 2.25. Description of battery impedance by using Nyquist plot is preferred with respect to Bode plot because it will be simple to notice how the battery model parameters affect the impedance curve. The y-axis is referred to the negative imaginary part of the impedance. Indeed, battery impedance assumes ohmic-capacitive behavior in the large part of interested frequencies. Frequency-domain battery model can be represented by using electrical circuit components. In the next section, more details about the circuit components and configuration are reported. By performing EIS test, physical and chemical properties of the battery can be observed in well defined frequency bands. The previous modeling in time-domain allows the user to describe the electrical behavior of the battery while presenting limited physical meaning in its parameters. This mismatch between time-domain modeling and physico-chemical properties of the battery may be observed from experimental EIS test.

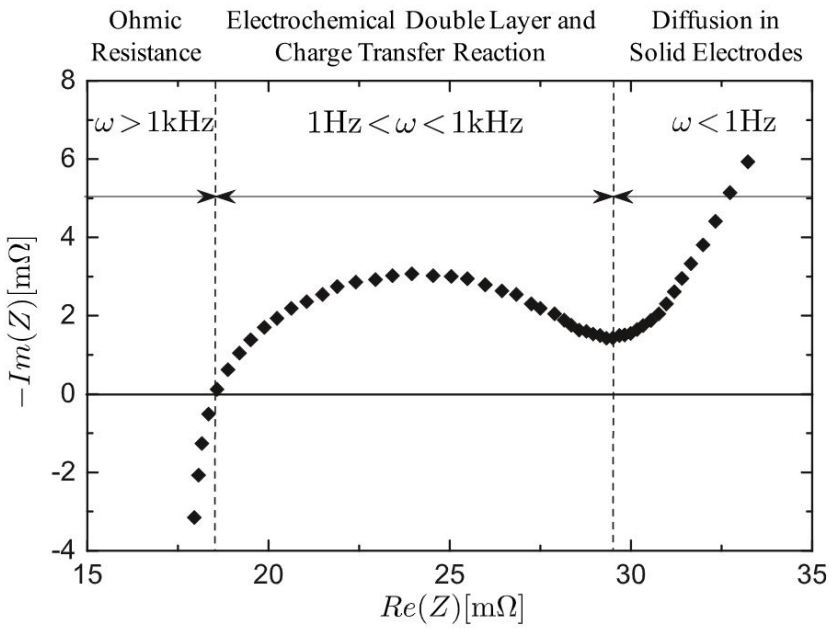

Figure 2.25: Nyquist plot of a typical lithium-ion battery and separation of three well identifiable dynamic internal processes detected in three well separated frequency bands [103].

2.4.1 Constant phase elements

Recalling the Figure 2.25, it's noticeable that in the frequency interval Hz÷kHz battery impedance curve shows a semi-ellipses arc. One of the methods which could be used to fit the semi-ellipses impedance arc is the following circuit configuration: a resistance R_0 in series to a RC block (R_1 in parallel to C_1). Despite this configuration can represent a semi-circle arc in Nyquist plot, it misses the degree of freedom (DOF) which can depress the semi-circle arc. Since increasing the number of RC-blocks in series should produce a better fit to the semi-ellipses curve, it will also increase complexity in the model identification due to the increment of the number of parameters. This issue can be overcome by using a special equivalent circuit element, the so-called, in literature, constant phase elements (CPEs) [46][103]. Transfer function of the CPE is represented by the following equation:

$$Z_{CPE}(j\omega) = \frac{1}{(j\omega)^{\alpha} Q} \tag{2.18}$$

CPE is usually used to describe the electrical properties of double layer capacitors, that occur on electrochemical energy storage systems, between the electrodes and electrolytes. Transfer function (2.18) is similar to the capacitance transfer function, except for the parameter $\alpha \in$ [-1,1] which is called depression factor. It represents the aforementioned DOF, as well as the constant phase $\alpha \times \pi/2$. Thanks to the CPE, it's possible to fit in Nyquist plot semi-ellipses arcs, hence, semi-circle arcs depressed by the assessment of α parameter. It's noticeable by (2.18) that the CPE should be represented as a non-ideal capacity (if $\alpha \in$ (0,1)) or non-ideal inductance (if $\alpha \in$ (-1,0)). Indeed CPE can represent perfectly a capacitance (α

= 1), resistance (α = 0) or an inductance (α = -1) parameter. In the circuits of Figure 2.26 (above) it's noticeable that the complex impedance of an ideal capacity component (CPE with $\alpha = 1$) describes only a semi-circle with a radius equivalent to $R_1/2$ and shifted of R_0 by the origin point. Decreasing the depression factor α, it's possible to obtain semi-ellipses arc decreasing the focal distance, as noticeable in Figure 2.26.

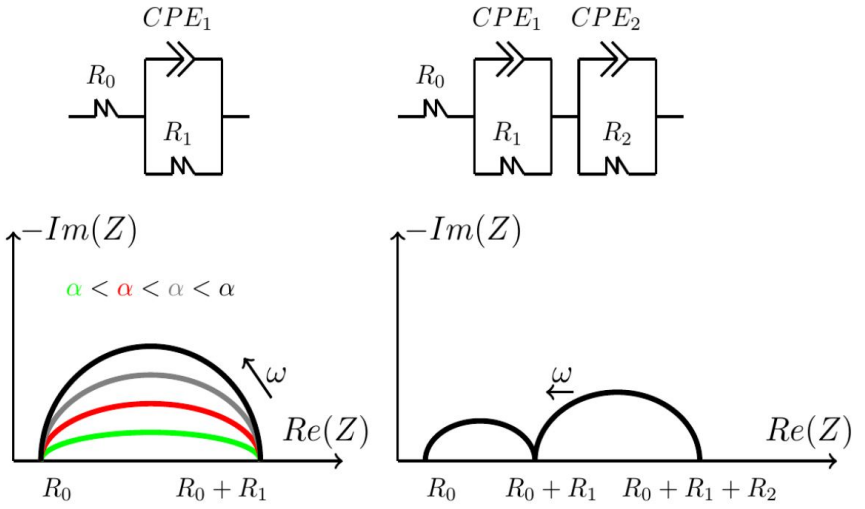

Figure 2.26: EEC with CPEs and their frequency characteristics in Nyquist plots.

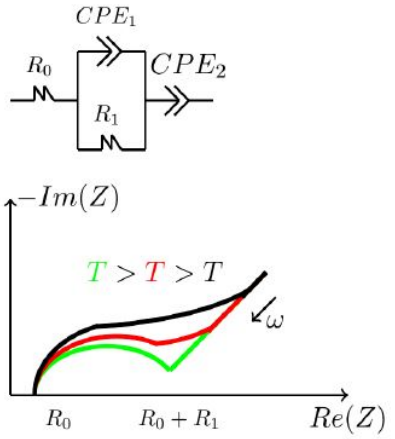

Figure 2.27: New circuit configuration with CPEs to fit semi-ellipses arc joint to straight line.

Moreover, considering a circuit configuration realized by a series of two R-CPE blocks, two semi-ellipses arcs are represented if the two CPEs differ at least one order of magnitude.
Circuit configuration depicted in Figure 2.27 fits a semi-ellipse joint with straight

line of slope equivalent to $\alpha_2 \times \pi/2$. In particular, defining $\tau_1 = R_1Q_1$, $\tau_2 = R_1(Q_1 + Q_2$ and $T = \tau_2/\tau_1$, impedance line become more blunt with increasing T [46]. Referring to the Figure 2.25, battery impedance curve is represented by a straight line at low frequency. This curve can be represented by using a CPE in series. In the case of $\alpha = 0.5$ (slope 0.5), CPE is also called Warburg element. Finally, battery impedance curve in high frequency band assumes ohmic-inductive behavior, which can be represented by using inductance in series with a resistance. CPEs are fundamental to build battery impedance model and obtain an accurate simulation of battery voltage response in frequency domain. However, it's not trivial to transform an EEC with CPEs in time-domain and run the model in simulation platforms. The Laplace anti-transform of the CPE corresponds to the following formula:

$$\mathcal{L}^{-1}\left\{\frac{1}{s^{\alpha}Q}\right\} = \frac{t^{\alpha-1}}{\Gamma[\alpha]Q} \tag{2.19}$$

Where the Gamma function $\Gamma[\alpha] = (\alpha - 1)!$ and the symbol ! denotes the factorial operation. In this PhD research, a part of the time was dedicated to develop a time-domain battery model based on EEC with CPEs (fractional EEC models). Starting from the Laplace anti-transform of the CPE shown in equation (2.19), time-domain EEC models used on battery modeling (R-CPE blocks) were reported in [71], and presented in RTSI conference, in 2019 in Florence. Considering that the input excitation current was a continuous current signal, it was decomposed into a train of square or trapezoidal wave signals of step time T, as shown in Figure 2.28. Time-continuous current decomposed by square or trapezoidal waves. The time-domain voltage response of battery model with CPEs is calculated, based on (2.17). Model's accuracy and run speed are evaluated by comparing experimental and simulation results [71]. Similar studies were carried out in [104][105].

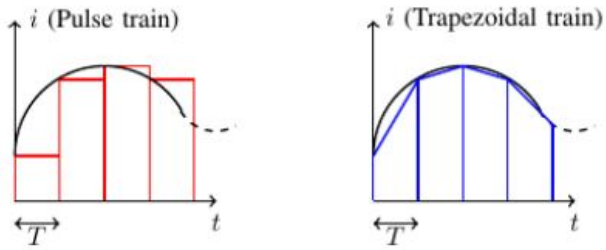

Figure 2.28: Different methods for decomposition of time-continuous signals.

2.4.2 Battery modeling in frequency domain

In this PhD thesis, the battery impedance curve taken into consideration is depicted in Figure 2.30. The difference respect to the Nyquist plot shown in Figure 2.25 consists of the consideration of two jointed semi-ellipses arcs. The shape of this impedance curve is observable during battery lifetime, as noticeable in [38][47][59]. Spectroscopy analysis allows to investigate different internal processes in the battery defined in well known and separated frequency bands. The evolution of battery chemical-physical property variations due to aging can be studied by using electrical circuit equivalent models. Its parameters are well identified by fitting impedance data in a defined frequency band. Before analyzing these internal processes in detail, it's important to recall the operating principle of a generic lithium battery. In principle, an electrochemical cell provides a potential by electrically exploiting the difference between electrochemical potentials of anode and cathode. Both electrodes in the battery system are electronic conductors of a different electrical potential due to different electrochemical potential: this last potential is given by the amount of lithium particles stored. As a designed feature, the concentration of lithium particles intercalated in the anode is always higher than in the cathode. Lithium particles are strongly attracted by cathode. In order to reach an equilibrium of electrochemical potential, but are blocked by the electrolyte layer, which doesn't allow the electron transfer. Hence, when anode and cathode are closed by external circuit, the resulting difference in electrochemical potentials between the electrodes acts as the driving force for electrochemical reactions. This leads to enabling spontaneous transfer of lithium-ion particles from the anode, reaching the intercalation into the cathode by passing to the electrolyte. Discharging process works like this and it is illustrated in Figure 2.29.

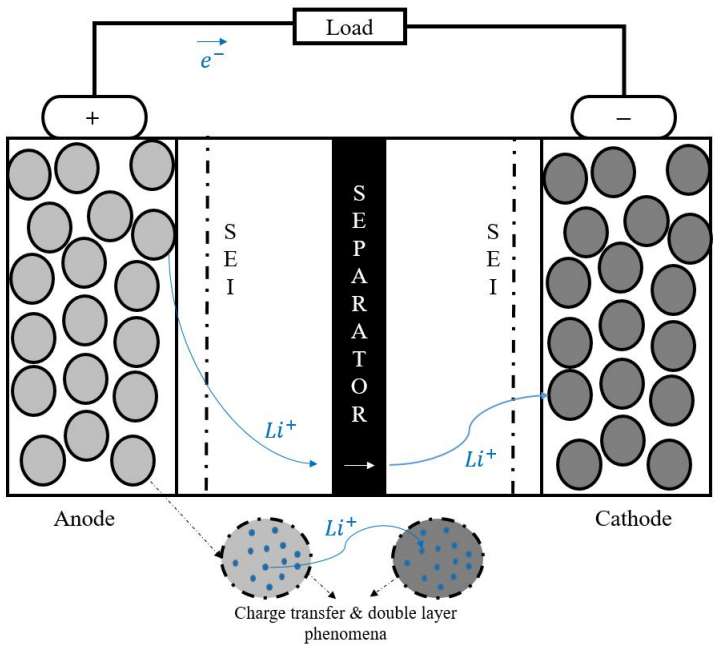

Figure 2.29: Schematic describing the discharge process and lithium-ion transfer.

The process of absorbing a lithium-ion particle (Li^+) into an active material of electrode is referred to as intercalation or lithiation, while the process of releasing a Li^+ into the electrolyte is called de-intercalation or de-lithiation. The transfer of lithium-ion particles, electrons, from anode towards the cathode and viceversa can be represented by a series of electrochemical process. In this PhD thesis, focus is the modeling and the parametrization of equivalent circuits which well describes the several internal processes which define the transfer of lithium-ion particles. In literature, five noticeable different frequency intervals are investigated and parametrized with circuit components, as noticeable in Figure 2.25: every band represents a particular battery internal process, explained as follows, starting by low frequencies:

- **Diffusion processes ($<$ 1 Hz):** As noticeable in the previous section, battery voltage response was in delay with respect to input current due to mass and charge transport limitations. This ohmic-capacitive effect is the reason which leads to the voltage relaxation effect when battery is disconnected by the load. Since the particles involved in the reactions have a mass and are physically diffusing through electrodes and electrolytes, limitations to mass diffusion have to be taken into consideration [40]. This effect can be investigated by EIS test, analyzing the low frequencies. By Figure 2.30, the impedance curve at low frequencies is drawn by a straight line. Indeed experimental impedance data can be fitted by a straight line, hence by using a series CPE. Usually, researchers consider the infinite Warburg element transfer function, referring to equation (2.18) with fixed $\alpha = 0.5$ [53][106].

- **Charge transfer resistance and double layer capacitance ($f \in [1, 1000]$ Hz, first semi-ellipses arc):** As highlighted in Figure 2.29, charge-transfer resistance and double layer capacitance phenomena occurs in the electrodes-electrolyte interface. The charge-transfer phenomena is represented by the first semi-ellipses arc of impedance curve as shown in the Figure 2.30. Lithium particles, passing by electrode surface, are subjected to a change of their electrical potential, like a series resistance. Charge-transfer resistance is often attributed to the Butler-Volmer kinetics of the reaction [108]. In the lifetime, charge transfer resistance increases in the anode due to the contractions/expansions related to the charge/discharge cycles, which crack it and increase the exchange surface (interface) with the electrolyte. The electrochemical double layer phenomena forms at the interface of an electrical conductor and an ionically conducting electrolyte. this is due to the local charge inhomogeneities, which occur as soon as a cell is first assembled and the components come into contact [106]. The double layer behaviors are usually represented by a constant phase element, of which capacitance is proportional to its interface area.

- **Solid electrolyte interphase film formation ($f \in [1, 1000]$ Hz, second semi-ellipses arc):** Upon first assembly of lithium cell, a passivating solid electrolyte interphase (SEI) layer forms at the electrode surface. This additional layer prevents the direct contact between electrode and electrolyte. This is crucial for a long term performance of the battery and stable charge transfer reactions over the entire electrode surface. For this reason is fundamental to perform the first charging/discharging cycles on a new cell with limited and strictly controlled current amplitudes. In the previous experi-

ment preconditioning test were performed to the new cells, in order to grow this passivation film. When lithium particles go through this layer, their electrical potential changes as similar to a RC block. In the Nyquist plot shown in Figure 2.30, this phenomena is represented by the second semi-ellipses arc of impedance curve and fitted by using R-CPE block.

- **Ohmic resistance ($>$ 1 kHz, zero-crossing impedance):** It represents the value of battery internal resistance at a single particular point, the zero-crossing frequency. This last frequency is assessed when imaginary part of impedance is null. The current delivered/supplied by the battery comes with voltage drop due to current collectors, active materials of the electrodes, electrolyte and separator [47].
- **Inductive behaviors ($>$ 1 kHz):** At the highest frequency, an inductive behavior is observed due to reactance of battery connectors and instrument measurements.

In literature exist more circuit configurations which fit impedance curve and give informations about the change of the overcited internal processes of battery. The most common circuit used for battery impedance modeling are also called Randles circuits [108], and are shown in Figure 2.31. In this PhD, the first configuration is used, where transfer function is represented as follows:

$$Z_{model}(j\omega) = j\omega L + R_{\Omega} + \frac{R_{SEI}}{(j\omega)^{\alpha_{SEI}} R_{SEI} Q_{SEI}} + \frac{R_{CT}}{(j\omega)^{\alpha_{DL}} R_{CT} Q_{DL}} + \frac{1}{\sqrt{(j\omega)} Q_W} \tag{2.20}$$

Experimental EIS test were performed on the five EIG cells with different SOH. Results concerning circuit's parameter identification are reported in the paper [73] presented in EEEIC conference (2020). In recent years, the use of CPEs for fitting battery impedance is quite widespread in the literature. However, some recent studies criticize its use, presenting limited physical meaning in its parameter and high computational efforts in its voltage response, simulation running. A valid impedance identification method suggested in the literature is the use of RC "ladder networks", fitting measured battery impedance with serially connected parallel-coupled pairs of resistor and capacitor [109]. This last method will be again mentioned in Chapter 4 when the accuracy of the impedance measurements and Kramers-Kronig validity-test method will be discussed.

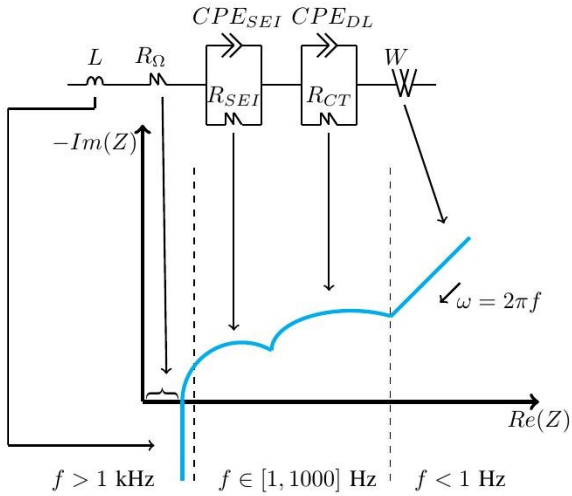

Figure 2.30: Reference impedance curve of lithium cells in a wide frequency range and battery Randles model.

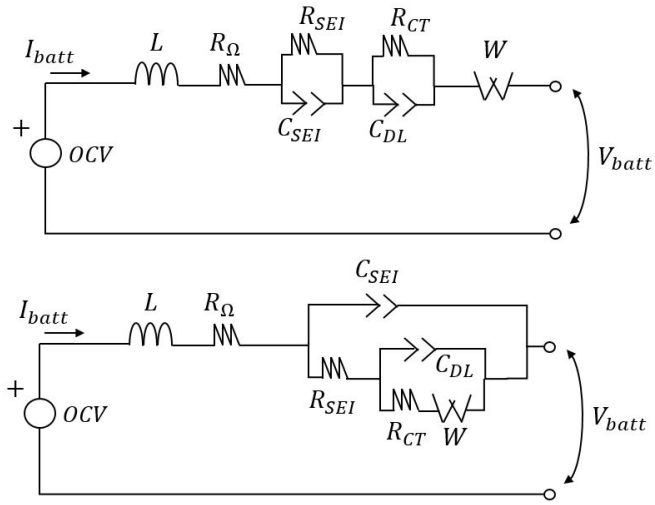

Figure 2.31: EEC used for the modeling of the measured impedance data after EIS test is performed.

Chapter 3

Online state of charge estimation based on model adaptive Kalman filters

Monitoring and prediction of battery SOC is a challenging task in automotive field, in particular in the research and development of innovative BMS. The development of new methodologies concerning SOC estimation is more and more considered in literature. Recalling the introduction, many SOC algorithms are developed through the use of model-based observers [27]-[37]. This section presents a set of model-based algorithms for the estimation of state of charge, specifically deployed for lithium batteries. These algorithms require a priori knowledge of a battery model. Battery model types presented in literature were discussed in Section 2. The models can be developed having different levels of accuracy, also including the possibility to correctly represent the hysteresis voltage behaviour of the selected lithium cells. Furthermore, different identification methods of the battery model parameters may also be considered, considering tabulated parameters, discussed in the previous section, or online parametrization tools. Recalling the model-based approach, being a closed-loop method, state of charge estimation is estimated through the Kalman filter approach, which minimizes the prediction error. General algorithm's block system is represented in Figure 3.1. A wide configuration of SOC estimators based on non-linear Kalman filters (NLKFs) approach has been accurately evaluated through experimental tests performed on a LFP cell. It will be noticeable that the addition of a hysteresis model will be fundamental for this chemistry, in terms of SOC prediction accuracy. One of the algorithms presented is a novelty of the SOC estimator's state of art. To verify the robustness of the proposed algorithms, some disturbances were introduced. Moreover the evaluation is conducted at different SOC initial conditions and sampling times. This work was published by the Journal of Systems and Control engineering [69], in the year 2020.

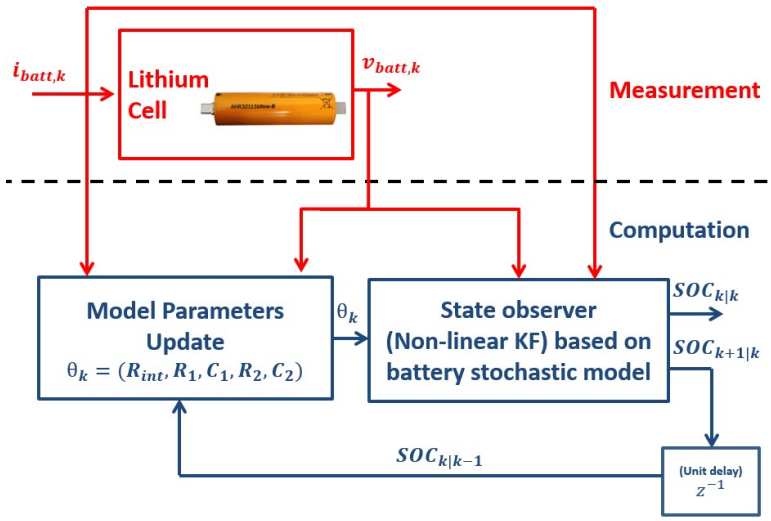

Figure 3.1: Model adaptive NLKF technique for battery SOC estimation.

3.1 Model adaptive non-linear Kalman filter: algorithm

3.1.1 Electrical battery model

The first proposed mathematical battery model refers to the classic 1^{st} or 2^{nd}-order Thevenin EEC shown in the Figure 2.15. Model parameters $R_{int}, R_1, R_2, C_1, C_2$ were calibrated in the entire SOC window. Hence, battery model adopted in this work is defined by the following system equation:

$$\begin{cases} SOC_{k+1} = SOC_k - \dfrac{I_{batt,k}T}{3600C_{curr}} \times 100 \\ \\ v_{1,k+1} = v_{1,k}e^{-T/\tau_{1,k}} - R_{1,k}I_{batt,k}(1 - e^{-T/\tau_{1,k}}) \\ v_{2,k+1} = v_{2,k}e^{-T/\tau_{2,k}} - R_{2,k}I_{batt,k}(1 - e^{-T/\tau_{2,k}}) \\ \\ OCV_k = f_{ocv}(SOC_k, SOH, sign(I_{batt,k})) \\ R_{int,k} = f_{R_{int}}(SOC, SOH, sign(I_{batt,k})) \\ R_{1,k} = f_{R_1}(SOC_k, sign(I_{batt,k})) \\ R_{2,k} = f_{R_2}(SOC_k, sign(I_{batt,k})) \\ C_{1,k} = f_{C_1}(SOC_k, sign(I_{batt,k})) \\ C_{2,k} = f_{C_2}(SOC_k, sign(I_{batt,k})) \\ \\ V_{batt,k} = OCV_k - v_{1,k} - v_{2,k} - R_{int,k}I_{batt,k} \end{cases} \tag{3.1}$$

As mentioned in the previous section, the model (3.1) is non-linear, due to the OCV-SOC relationship (f_{ocv}). Moreover, battery system is time-varying in the state-space $x_k = [SOC_k, v_{1,k}, v_{2,k}]$. The OCV-SOC curve extracted by a LFP cell is shown in Figure 3.2.
It's noticeable a slight difference between the charging and discharging OCV curves, which is due to hysteresis behavior. The hysteresis effect is caused by thermodynamic entropic effects, mechanical stress and other chemical effects in the electrode, during lithium particle insertion/extraction [110]. The hysteresis behavior occurs mainly in LFP cell [27]. By Figure 3.2 it's detectable that LFP cell's OCV curves show a relatively flat behaviour for values of the SOC range [10,90] %, while for extreme charge and discharge condition, a strong sensitivity of OCV with respect to SOC is recognizable. This last observation leads to infer a weak correlation between OCV and SOC for a large range of SOC values, which represents one of the most critical aspects of SOC estimation. Small differences in voltage measurements may consist of large differences of SOC. Therefore an accurate OCV-SOC curve calibration is needed for the final implementation of the battery model, based on 2^{nd}-order Thevenin equivalent circuit. Otherwise, this aspect can be mitigated by the introduction of the hysteresis property inside the battery model. More details will be reported in the next subsection.
As mentioned in the Section 2, model circuit parameters ($R_{int}, R_1, R_2, C_1, C_2$) vary with SOC, aging, temperature variations. In particular, temperature has a big impact on battery internal resistance, hence battery power efficiency. In the research work [37] (presented in EEEIC Conference, 2018) it was possible to identify the internal resistance of LFP battery packs on-board electric vehicles at different environment temperature. Results obtained in my previous work [37], demonstrated that internal resistance increases its value when temperature decreases and at low SOC. Moreover, as noticeable in [9] and in my previous work [70], circuit parameters change their value with aging, especially internal resistance increases with battery capacity degradation. In order to update the battery model with current battery operating conditions, tabulated circuit parameters (LUT) are required, or online calibration algorithms, based on the online parameter identification theory [32], could be used.

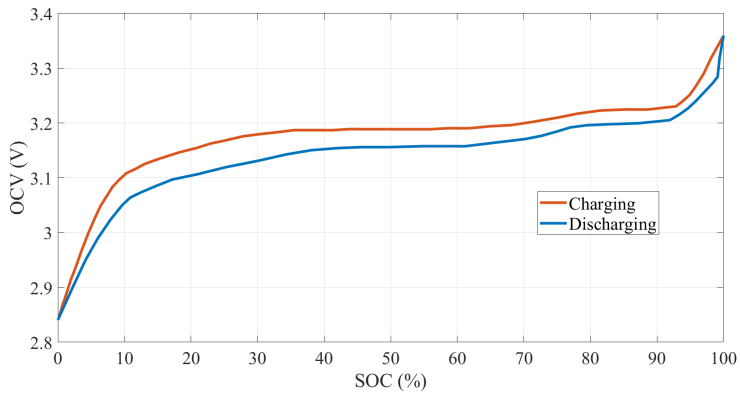

Figure 3.2: OCV-SOC curve of a LFP cell calibrated during pulse test.

3.1.2 Algorithms tested

The model-based approach, illustrated in Figure 3.1, represents the concept for SOC estimation adopted in this PhD thesis. SOC is estimated by voltage and measurement data, by a priori knowledge of the battery model, and by a criteria which minimizes the SOC prediction error, in this case Kalman filter approach. The battery model, adopted in the following algorithms, is represented by the time-discrete system (3.1), where T represents the sample time and k represents the step time instant kT, for $k = 0, 1, ..., N$.
In this section, different methods for battery model update, Kalman filtering approaches and battery voltage models are described and analysed to find the best SOC estimator. The first analysis is carried out on the different methodology of battery model update. The two different algorithms are represented in Figures 3.3 and 3.4, and are, respectively, called SOC-NLKF with tabulated model parameters and SOC-NLKF with online parameter identification. Circuit parameters can be updated at every step k in two different ways:

- **SOC-NLKF with tabulated model parameters:** the set of parameters $(R_{int}, R_1, R_2, C_1, C_2)$ is calibrated offline with entire SOC interval [0,100] % under laboratory tests at constant temperature (20°). Then one-dimensional (1D) look-up-tables (LUT) are realized for each parameter. Schematic of this approach is represented in Figure 3.3.

- **SOC-NLKF with online parameter identification method:** the set of parameters $(R_{int}, R_1, R_2, C_1, C_2)$ are recursively estimated online using a method of parameter identification for a particular class of models and prediction criterion. Schematic of this approach is represented in Figure 3.4.

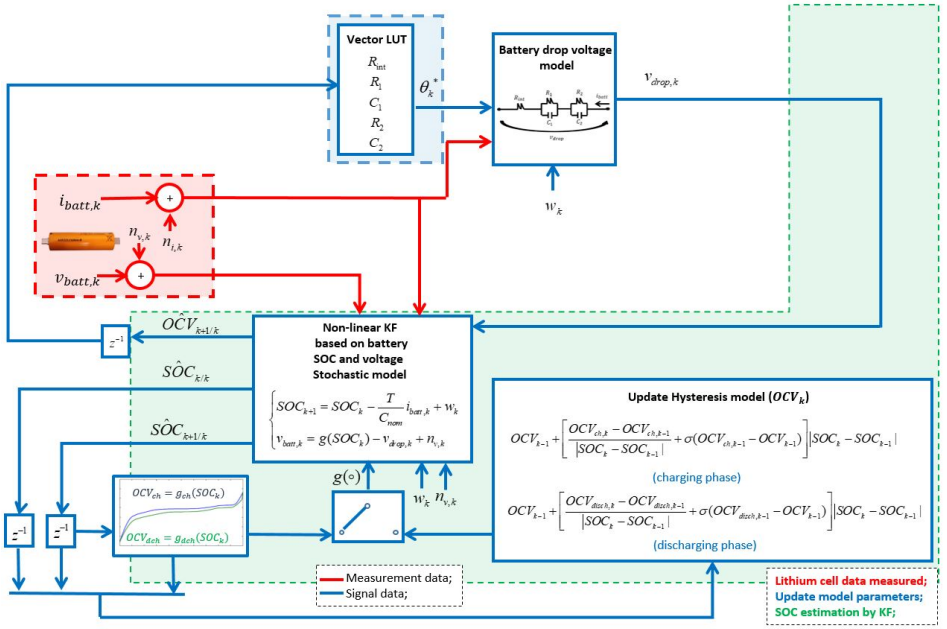

Figure 3.3: SOC estimation based on NLKF, tabulated model parameters.

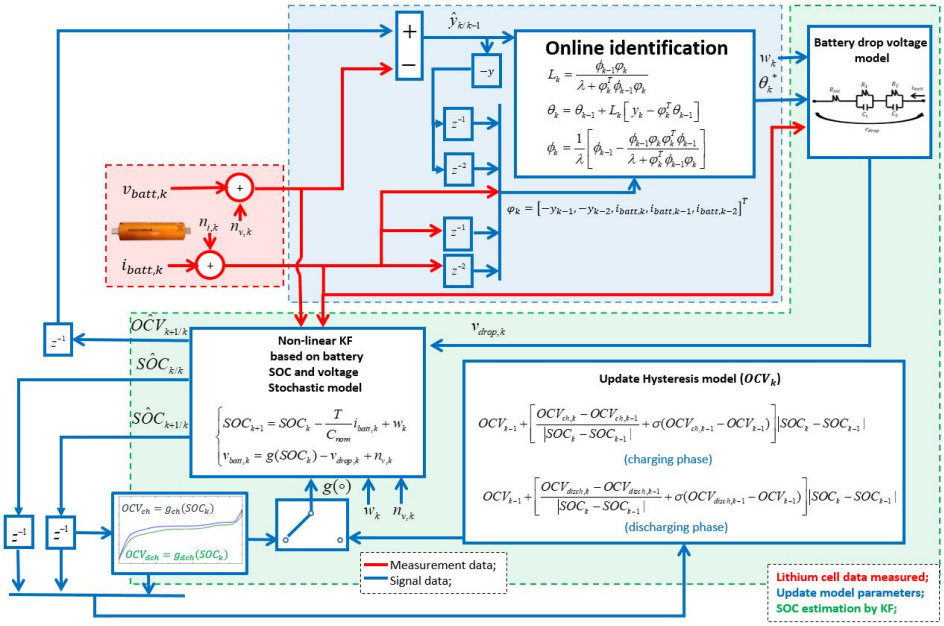

Figure 3.4: SOC estimation based on NLKF, online parameter identification tool.

Proposed algorithm for online parameter identification considers a black-box autoregressive exogenous model (ARX), using a minimum error prediction (PEM) criterion for identification [32]. Given the input battery current and the difference between OCV and voltage as output, the drop voltage model of battery system (3) can be simply transformed in the single-input-single-output (SISO) ARX model. Finally, the algorithm chosen for online battery parameter identification is the recursive least square with forgetting factor (RLSFF) [32]. Using this identification method, circuit parameters $\theta = R_{int}, R_1, R_2, C_1, C_2$, collected in the vector θ, are recursively estimated minimizing the following cost index:

$$J_k^{\lambda}(\theta) = \sum_{t=0}^{k} \lambda^{k-t} \left(v_{drop,t} - \varphi_t^T \theta_t\right)^2 \tag{3.2}$$

Where $v_{drop,t} = OCV_t - V_{batt,t}$ is the drop voltage observation, of which calculation is discussed later; φ_t^T denotes the transponse of the linear regression vector φ_t, which contains battery voltage and current measurement data. The cost index in equation (3.2) is the sum of the squares of prediction errors calculated at step k, and in previous instances, which are weighted by the parameter $\lambda \in [0,1]$, called the forgetting factor. The forgetting factor λ gives exponentially less weight to older error samples. In this way, the algorithm identifies the vector of circuit parameters θ minimizing the more recent cost terms when the forgetting factor λ is smaller, adapting it to actual operating conditions of the battery. The recursive equations of the online parameter identification algorithm (RLSFF) are shown as

follows:

$$\begin{aligned} L_k &= \frac{\phi_{k-1}\varphi_k}{\lambda + \varphi_k^T \phi_{k-1}\varphi_k} \\ \theta_k &= \theta_{k-1} + L_k \left[v_{drop,k} - \varphi_k^T \theta_{k-1} \right] \\ \phi_k &= \frac{1}{\lambda} \left[\phi_{k-1} - \frac{\phi_{k-1}\varphi_k\varphi_k^T\phi_{k-1}}{\lambda + \varphi_k^T\phi_{k-1}\varphi_k} \right] \end{aligned} \tag{3.3}$$

Typical λ values are 0.995, 0.99 and 0.98. It's noticeable in the RLSFF algorithm that the identification of battery model parameters θ_k is given by the previous update θ_{k-1} and by the weighted difference between the battery drop voltage observed $v_{drop,k}$ and the drop voltage estimated by the ARX model $\varphi_k^T\theta_{k-1}$. This difference corresponds to the parameters estimation error, which is weighted by the gain L_k. If the parameter estimation error is null, the current estimate θ_k is in perfect agreement with the previous estimate θ_{k-1}. The gain L_k provides a measure of the correlation between the vector θ_k to be estimated and the current drop voltage observation. Hence, L_k depends by voltage sensor accuracy and the current estimate error covariance matrix ϕ_k.
Two different approaches for battery model update are mentioned in this section.
As discussed in the previous section, battery SOC, which can be calculated with the Ampere-hour method (3.1), affects the battery voltage value because OCV depends on SOC.
The stochastic model, on which the KF will be based to estimate battery SOC, is represented in a discrete-time and stochastic state-space dynamic system:

$$\begin{cases} x_{k+1} &= x_k - \left[\dfrac{T}{36C_{curr}} \quad 0 \right] u_k + w_k \\ y_k &= f_{ocv}(x_k) - [0 \quad 1] u_k + n_{v,k} \end{cases} \tag{3.4}$$

Here, the state variable x_k denotes the battery SOC ($x_k = SOC_k$). The system input vector u_k collects the battery current measurement $I_{batt,k}$ and the battery drop voltage estimated $v_{drop,k}$. This last value is the output given by the update of circuit impedance parameters at step k (see Figures 3.3, 3.4). The output y_k of the system corresponds to the battery voltage measurement $V_{batt,k}$. Process and measurement noises are represented by variables w_k and $n_{v,k}$, respectively, considered as Gaussian white noises with zero mean and covariances of Q_k and R_k. The Kalman filter (KF) estimates battery SOC based on stochastic model (3.4). KF observer is the best estimator in the sense of minimum mean-square error (MMSE) for linear time-varying dynamic systems. However, the battery SOC model in equation (3.4) is non-linear due to the OCV-SOC relationship, $f_{ocv}(\cdot)$. Therefore, it's needed to consider the use of non-linear KF (NLKF) estimators. Two different NLKF techniques are evaluated in my algorithms proposed, that is, the extended KF (EKF) or the unscented KF (UKF). The two different approaches use the state correction and state prediction algorithms as in the linear KF. The battery voltage measurement $y_k = V_{batt,k}$ is used to correct the predicted state in step $k-1$, $x_{k/k-1} = SOC_{k/k-1}$, and the covariance predicted $P_{k/k-1}$ predicted in the previous step. Hence, the update of the battery SOC and its covariance

estimation error are performed according to the following equations:

$$\begin{aligned} K_k &= P_{k/k-1}C_k^T\left(R_k + C_k P_{k/k-1} C_k^T\right)^{-1} \\ x_{k/k} &= x_{k/k-1} + K_k\left[y_k - \left(f_{ocv}(x_{k/k-1}) - [0 \;\; 1]u_k\right)\right] \\ P_{k/k} &= P_{k/k-1} + K_k\left(R_k + C_k P_{k/k-1} C_k^T\right) K_k^T \end{aligned} \tag{3.5}$$

The EKF algorithm, linearizing the original non-linear system (3.4) around the current estimate $x_{k/k-1}$, computes the linearized battery voltage model matrix C_k as the following Jacobian:

$$C_k = \frac{\partial}{\partial x} f_{ocv}(x_{k/k-1}) \tag{3.6}$$

Instead, the UKF algorithm computes the first and the second moments of the random variable $OCV = f_{ocv}(x)$ applying the unscented transform (UT), referring to [111]. In this case, the UKF state correction algorithm is performed according to the following equations:

$$\begin{aligned} &\left[y_{UT,k/k-1}, P_{y,UT,k/k-1}, P_{yx,UT,k/k-1}\right] = \\ &= UT\left(x_{k/k-1}, P_{k/k-1}, f_{ocv}(x_{k/k-1}) - [0 \;\; 1]u_k\right) \\ K_k &= P_{yx,UT,k/k-1}\left(R_k + P_{y,UT,k/k-1}\right)^{-1} \\ x_{k/k} &= x_{k/k-1} + K_k\left(y_k - y_{UT,k/k-1}\right) \\ P_{k/k} &= P_{k/k-1} + K_k\left(R_k + C_k P_{y,UT,k/k-1} C_k^T\right) K_k^T \end{aligned} \tag{3.7}$$

Finally, there is no difference by EKF and UKF algorithm in the calculation of battery SOC prediction, because SOC evolution is represented by a linear model. SOC and covariance estimation error prediction algorithm are performed according to the following equations:

$$\begin{aligned} x_{k+1/k} &= x_{k/k} - \left[\frac{T}{36C_{curr}} \quad 0\right] u_k \\ P_{k+1/k} &= P_{k/k} + Q_k \end{aligned} \tag{3.8}$$

Thus, in the following, the attention will be dedicated on the battery voltage model (3.4). The function f_{ocv} relates battery SOC with OCV. In this section, two different methods for the OCV evaluation are proposed: the first method consists of the representation of the function f_{ocv} in a discontinuous form, depending on the sign of battery current (charging or discharging phase):

$$f_{ocv} = \begin{cases} g_{ch}(SOC_k) &= \sum_{j=1}^{n_p}\left(\alpha_j SOC_k^j\right) + \alpha_0, \quad \text{charging} \\ g_{dch}(SOC_k) &= \sum_{j=1}^{n_p}\left(\beta_j SOC_k^j\right) + \beta_0, \quad \text{discharging} \end{cases} \tag{3.9}$$

The set of parameters $(\alpha_0, \alpha_1, ..., \alpha_{n_p}, \beta_0, ..., \beta_{n_p})$ is calibrated during laboratory test with entire SOC interval; hence, the OCV model is tabulated with SOC. With the main aim to further enhance the accuracy of the battery voltage model in

equation (3.4), the second method adds a mathematical model of the hysteresis behaviour of the cell. The analytical hysteresis model is shown in the following equation:

$$\frac{df_{ocv}(SOC)}{dSOC} = \begin{cases} \dfrac{dg_{ch}(SOC)}{dSOC} + \sigma(g_{ch}(SOC) - f_{ocv}(SOC)), & \text{if} \quad \dfrac{dSOC}{dt} \geq 0 \\ \dfrac{dg_{dch}(SOC)}{dSOC} + \sigma(g_{dch}(SOC) - f_{ocv}(SOC)), & \text{if} \quad \dfrac{dSOC}{dt} < 0 \end{cases} \tag{3.10}$$

This model tends to move towards battery OCV, that is, the upper curve ($g_{ch}(\cdot)$) when the cell is charging, the lower ($g_{dch}(\cdot)$) when discharging. In pursuing this objective, the mathematical model determines the derivative of OCV as a function of the direction in which SOC is moving, and on how actual model OCV is far from the target curve. When the time derivative of OCV is positive, the model is gradually moved towards the charging curve g_{ch}, the opposite g_{dch} when the time derivative of OCV is negative. The speed of transition from one curve to the other is determined by the constant σ, which needs to be calibrated based on an appropriate test, as reported in [27]. By observing the equation (3.10), the hysteresis OCV model reaches the target curve more rapidly when σ value is increasing.
The analytical hysteresis model in equation (12) is implemented in the KF correction algorithm (3.5). Then, the OCV model is transformed to the following time-discrete model at step k (considering the state $x_k = SOC_k$):

$$f_{ocv}(x_{k/k-1}) =$$

$$= \begin{cases} \dfrac{g_{ch}(x_{k/k-1}) - g_{ch}(x_{k-1/k-1})}{x_{k/k-1} - x_{k-1/k-1}} + \sigma(g_{ch}(x_{k-1/k-1}) - OCV_{k-1}) \times \\ \times |x_{k/k-1} - x_{k-1/k-1}|, \\ \text{if charging} \\ \\ \dfrac{g_{dch}(x_{k/k-1}) - g_{dch}(x_{k-1/k-1})}{x_{k/k-1} - x_{k-1/k-1}} + \sigma(g_{dch}(x_{k-1/k-1}) - OCV_{k-1}) \times \\ \times |x_{k/k-1} - x_{k-1/k-1}|, \\ \text{if discharging} \end{cases} \tag{3.11}$$

Where $g_{ch}(\cdot)$ and $g_{dch}(\cdot)$ are defined in equation (3.9).
In conclusion, combining the two different model parameter identification methods, KF techniques and OCV models, eight algorithms for SOC estimation have been tested. The flowchart shown in Figure 3.5 summarizes how the different algorithms work to estimate battery SOC. By performing experimental tests, it was verified that differences due to the selected NLKF technique are negligible, in terms of performance and computational cost. From now on, the difference of selection of Kalman filter technique will be neglected when discussing SOC-NLKF. Therefore, the SOC estimation performance of only four algorithms will be evaluated in this section: the SOC-NLKF with tabulated model parameters and the online parameter identification (using the RLSFF method), with or without the hysteresis model. In the next subsection, the performance of the four algorithms will be compared with experimental laboratory tests. First, it is important to define the requirements of the four KF types to run on the simulation tool. SOC-NLKF algorithm with tabulated model parameters requires to obtain the experimental f_{ocv} function and

the eventual speed transition σ for the hysteresis model, and circuit parameters $(R_{int}, R_1, R_2, C_1, C_2)$ in relation with SOC. Therefore, it requires the preliminary execution of experimental laboratory tests.
In the case of SOC-NLKF with online parameter identification method, only f_{ocv} curve calibration is needed, because circuit parameters are recursively identified with the RLSFF method. The RSLFF algorithm is made up of only 3 recursive equations shown in equation (3.3). The reduction in these requirements should be considered as the main advantage because it requires fewer laboratory tests and the absence of a declaration of model parameters (i.e. internal resistance and RC-groups). Using the online method, the battery model is adapted to the battery under test, which can be different from the others due to manufacturing tolerances. Moreover, the online method adapts the model to the actual operating condition of the battery, thus actual SOC, temperature, or aging level. Finally, it requires a reduction of static memory space in the filled-out algorithm.
Regarding measurement instruments, both KF types require voltage and current input data for SOC estimation. In the next sections, laboratory setup and measurement instrument's accuracy will be presented.

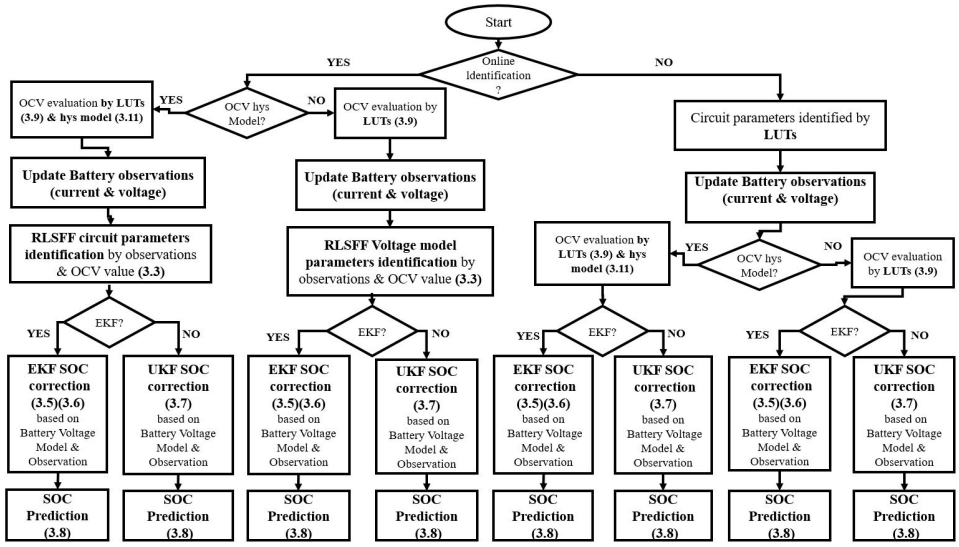

Figure 3.5: SOC estimation based on model-adaptive NLKF approach: eight different algorithms and flowchart.

3.1.3 Test data: battery cell and laboratory setup

In this work, two different LFP cells have been used to validate the SOC estimators algorithm. The first is a nanoscale LFP cell of nominal capacity 4.4 Ah and nominal voltage 3.2 V, exactly the A123 Systems AHR32113 M1 Ultra-B LFP cell. The second is a prismatic China aviation lithium battery (CALB) cell of nominal capacity 72 Ah and nominal voltage 3.2 V. Main specifications of the LFP cells used in this work are presented in Table 3.1; a picture of the cells is shown in Figure 3.6.

Specifications	Nanoscale LFP cell	CALB LFP cell
Nominal capacity	4.4 Ah	72 Ah
Nominal voltage	3.2 V	3.2 V
Specific power	2700 W/kg	2880 W/kg
Specific energy	71 Wh/kg	101 Wh/kg
Energy density	161 Wh/L	167 Wh/L
Cell dimensions	32×110 mm	222×135×29 mm

Table 3.1: Nanoscale and CALB LFP cells specifications.

Figure 3.6: Picture of nanoscale (a) LFP cell and CALB (b) LFP cell used in this section.

The first cell (nanoscale LFP cell) was subjected to tests based on the reference current cycle shown in Figure 3.7: this current profile corresponds to an example of the real usage of the battery on-board hybrid vehicles. The current profile was applied on the nanoscale LFP cell at constant temperature (20°C) and downsized to stay within current limits of the cell. Test was performed in the University of Pisa, and all measurements were acquired with the laboratory test setup shown in Figure 3.8. During the test, input data were acquired every sample time $T = 0.1$ s, using a shunt sensor for current measurement, class 0.5 and full scale 150 A, and DAQ device (model NI 9219) for voltage reading, with a declared accuracy of 0.3 %. The second cell, CALB cell, was monitored while it was installed on a battery pack on-board the real working EV (Isuzu L35), see Figure 3.9. An example of this

battery data-set measurement is shown in Figure 3.10.
Recalling the nanoscale cell, results on SOC estimation obtained by considering two different model's identification methods, with or without the hysteresis model are compared with the real battery SOC obtained by integrating the current profile, measured through high-precision sensors. To show the robustness of the algorithms for SOC estimation, and to define algorithm requirements in terms of sample time and instrument measurement accuracy for preliminary battery calibration and on-line estimation, the following parameters will be modified during the simulation test:

- Initial condition of estimated SOC.
- Additive process noise due to preliminary battery parameters calibration w_k and due to battery SOC observer. These noises are defined as process noises.
- Additive current and voltage measurement noise $n_k = [n_{i,k}, n_{v,k}]$.
- Sample time T.

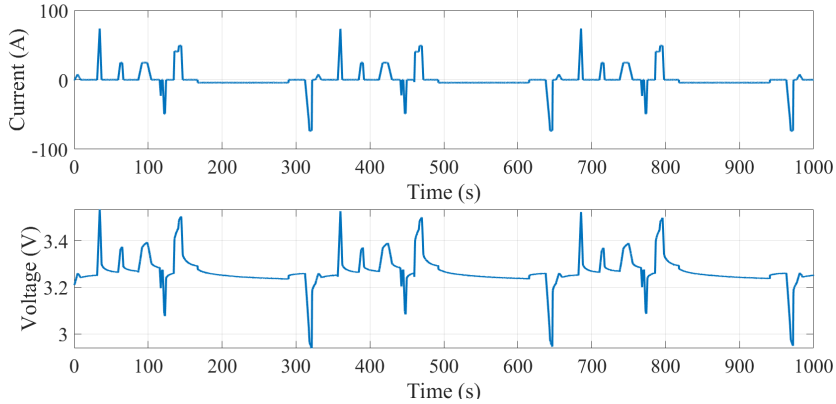

Figure 3.7: Reference cycle test applied to nanoscale LFP cell: current profile (top) and cell voltage (bottom).

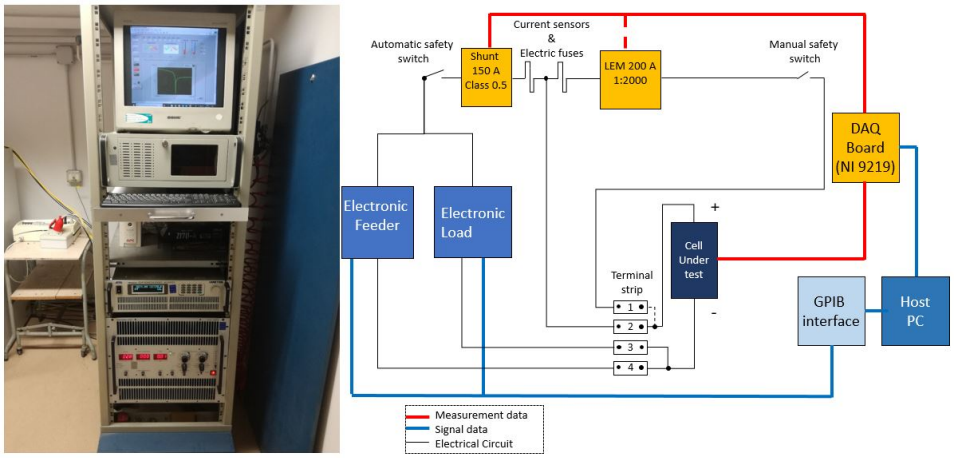

Figure 3.8: Laboratory test and measurement setup, located in the University of Pisa, adopted to perform the current profile shown in Figure 3.7.

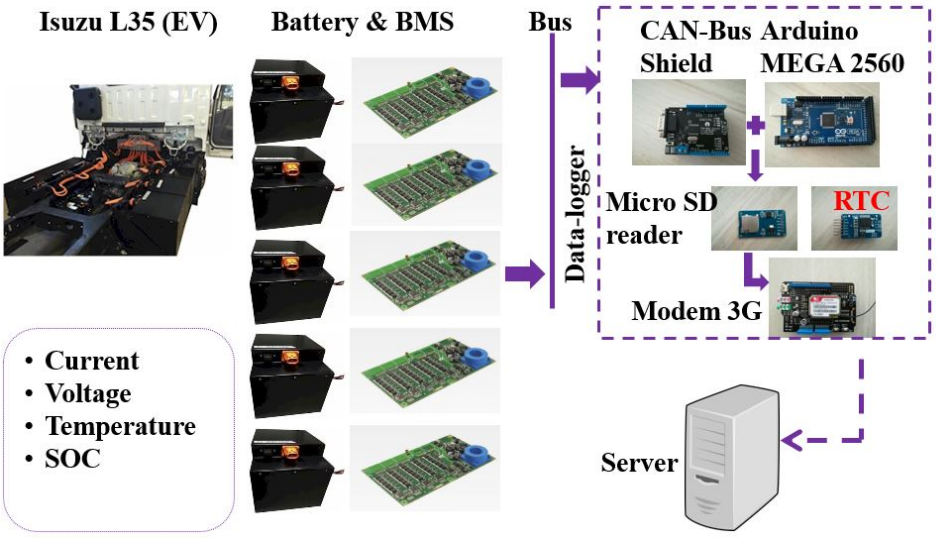

Figure 3.9: Logging CALB cell in the battery pack on-board the ISUZU L35, Master thesis's work [37].

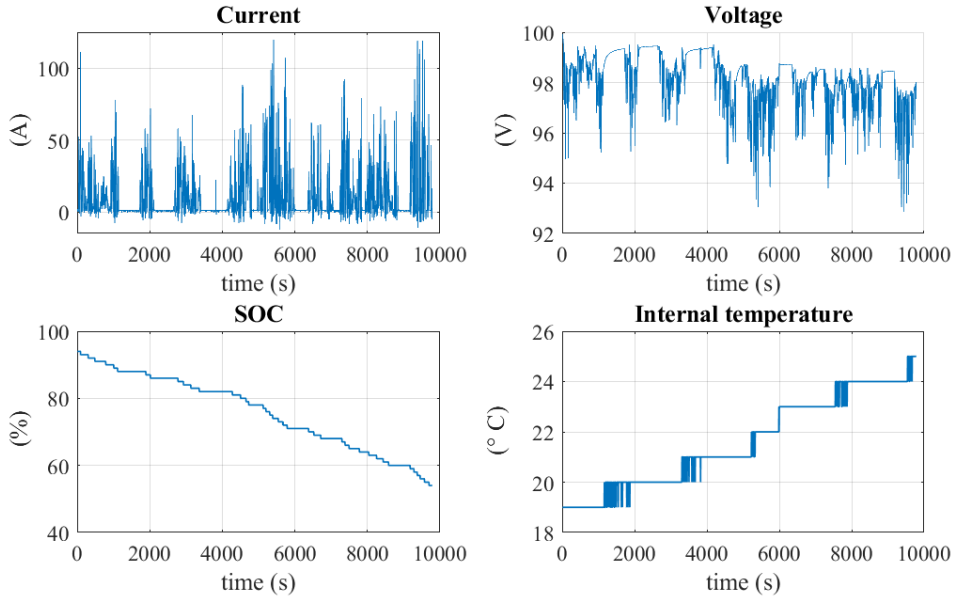

Figure 3.10: Current profile provided by the CALB battery pack, Master thesis's work [37].

3.2 Analysis performance for online parameter identification

The performances of the online parameter identification tool, the RLSFF algorithm (3.3) were analysed in terms of voltage prediction accuracy, based on data-set of battery voltage and current measurement. Simulations were carried out by using Matlab/Simulink software. Different LFP cells and respectively different experimental tests were considered in the simulations.
The single nanoscale LFP cell (4.4 Ah and 3.2 V, Table 3.1) was subjected to cycle test depicted in Figure 3.7 (cycles are repeated until the final time of 16000 s), performed by laboratory setup shown in Figure 3.8. Battery voltage and current measurement were acquired at a sample time of 0.1 s. Figure 3.11 shows the battery voltage estimated from the 2°-order EEC battery model, using an online parametrization (RLSFF) or tabulated parameters. The forgetting factor considered in this work is $\lambda = 0.995$. Note that the evolution of the voltage estimated using the online parameter identification (RLSFF) and battery model with tabulated parameters is similar. The maximum voltage error is 58 mV. Absolute mean and standard deviation (std) voltage errors are 14 and 12 mV, respectively. More details about this test were reported in reference [69].
In another work of this PhD thesis [37], five CALB LFP battery packs (72 Ah and 96 V) installed on a working EV (Figure 3.9) were monitored and RLSFF was validated based on 43 different real daily data-set. Battery current, voltage, SOC and temperature were measured at sample time 5 s. An example of this log is shown in Figure 3.10. Figure 3.12 shows circuit parameters calibrated online by RLSFF. Relative root-mean square voltage prediction error for each battery pack is reported in Table 3.2. Results of parameter identification were satisfac-

tory. By Figure 3.12 it's clear that battery pack's parameters don't evolve in time with equal values, despite the manufacture of five battery packs is the same. The causes are two: BMS master manages the equalization requiring different intensity of current for each battery; moreover batteries are placed in different positions of vehicle, consequently they are exposed under different temperatures. Therefore, the performance of online parameter identification with RLSFF effectiveness is validated in terms of accuracy. Additional considerations could be made regarding the algorithm computational cost. RLSFF algorithm (3.3) is made up of only three recursive matrix equations. Moreover, this algorithm requires a reduction of static memory space in the filled-out algorithm with respect to the tabulated parameter method. Finally, RLSFF avoids to perform some laboratory calibration tests.

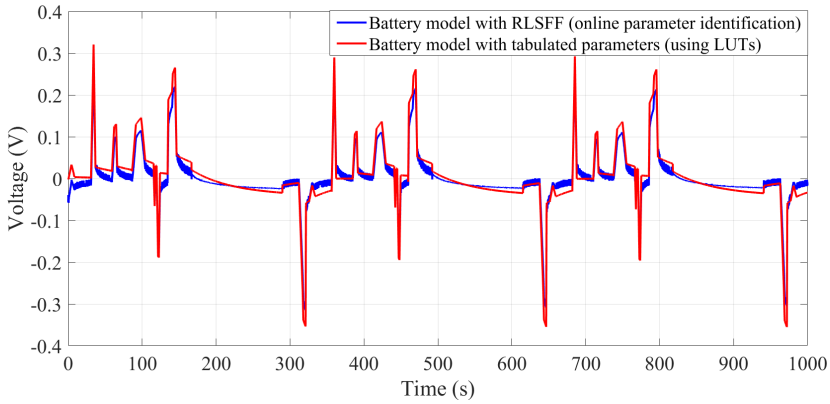

Figure 3.11: Voltage estimated by 4.4 Ah and 3.2 V nanoscale LFP battery model, parameters determined using online identification (RLSFF) or tabulated parameters.

Battery pack n.	**Mean RMSE (%)**	**Std RMSE (%)**
1	0.169	0.058
2	0.175	0.052
3	0.167	0.066
4	0.166	0.053
5	0.169	0.058

Table 3.2: Root mean square error (RMSE) results obtained by RLSFF (relative to 72 Ah, 96 V CALB battery packs)

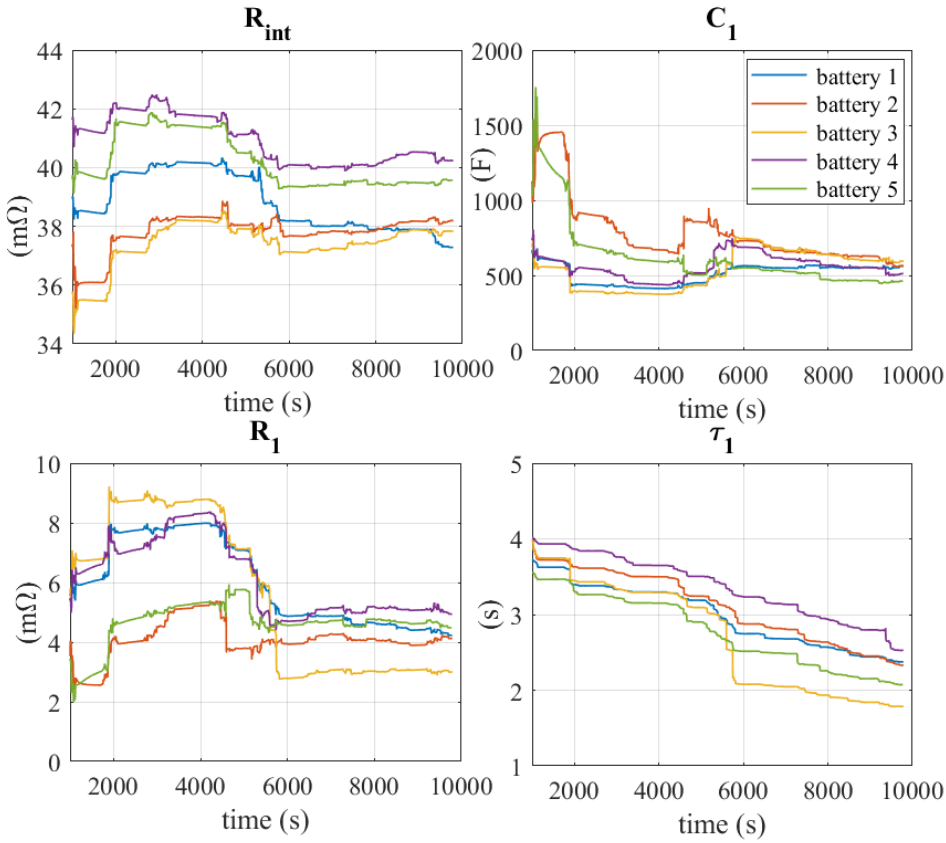

Figure 3.12: Identification of the five CALB battery packs (72 Ah and 96 V) installed on Isuzu L35 referring to data set shown in Figure 3.10.

3.3 Analysis performance for online state of charge prediction

In this section, the effectiveness of the SOC estimator algorithms has been evaluated and described with particular focus on the test performed on a nanoscale LFP cell. Regarding results obtained on the CALB cell and battery pack, please, check the reference [37].

3.3.1 Performance at different initial condition (i.c.) of state of charge

The SOC estimation performance for the different NLKF algorithms shown in Figure 3.5 has been evaluated. Referring to model-based approach shown in Figure 3.1, two main operations compute these algorithms: the first is regarding the update of the battery model circuit parameters, and the second is for SOC estimation using the Kalman approach for non-linear and time-varying systems. Matlab/Simulink simulation platform has been used to implement the different NLKFs, while the estimation of the state evolution has been performed through the acquisition of

current and voltage from the selected reference test cycle shown in Figure 3.7. To evaluate the performance of the algorithms, the test has been repeated many times, until the final time t_{fin} of 16000 s.
The aim is to evaluate the robustness of the algorithms previously described. Different cases of study are analysed. First, results of SOC estimation are compared at different initial conditions of estimated SOC by NLKF, keeping the same tune of the KF parameters. The true initial condition of battery SOC is 64 %. This particular initial condition of battery SOC has been chosen because it is located exactly in the critical flat zone of the OCV-SOC curve when SOC correlation is extremely difficult to achieve. Estimation results by model-adaptive NLKFs with and without the hysteresis model, considering the speed of transition $\sigma = 10$, are shown in Figure 3.13 and Table 3.3. The SOC time convergence, t_{conv}, and information about steady SOC error, $e_{ss,m}$, have been considered the performance indicators in this work for SOC estimation. This last parameter mentioned $e_{ss,m}$, is defined as follows:

$$e_{ss,m} = \frac{1}{t_{fin} - t_{conv}} \int_{t_{conv}}^{t_{fin}} |SOC_{real}(t) - SOC_{estimated}(t)|dt \tag{3.12}$$

The SOC time convergence, t_{conv}, is the time duration for which the absolute error, $|SOC_{real}(t) - SOC_{estimated}(t)|$, falls below the threshold of 5 %. This value can be considered rather high, especially under particular conditions, for example, when the battery pack of an EV is almost completely discharged. For that reason, the trend of the SOC error curve has been analysed, when it comes to lower than 5 %. Results shown in Table 3.3 prove that different SOC-NLKF algorithms have the same trend of the steady response, when the steady SOC error value, $e_{ss,m}$, is in the range [1,2] %. Moreover, the time convergence of each filter is highest whereas the initial condition of the estimated SOC starts at an interval of [10,40] %. This result is due to the approach followed by the Kalman observer. Indeed the SOC estimated is obtained by minimizing its mean square error, based on the actual voltage measurement $y_k = V_{batt,k}$ and by the battery system defined in the state-space in equation (3.4), thus by SOC equation based on the integration of current and by the OCV-SOC curve. As previously mentioned, a significant feature of the LFP cells is the extremely flat OCV-SOC curve in the middle part of the OCV-SOC window, unlike other lithium-based chemistries. This means that small differences in OCV correspond to large differences in SOC. Figure 3.13 shows that KF converges very fast to true SOC value when the initial condition of SOC estimated by NLKF is 90 % instead of 30 %. The OCV-SOC curve shows a much more significant slope in the window range [70,90] %, as noticeable in Figure 3.2 thus the correlation OCV-SOC is easier to achieve.
Therefore, to improve the time convergence of the SOC estimator, it is not only needed to have accurate sensors, but it is necessary enhance battery model in terms of accuracy, adding more features. In this regard, a mathematical OCV hysteresis model was introduced: referring to Figure 3.2, in the first two filters without hysteresis, OCV is represented as a discontinuous function, which moves from the top curve when the cell is charging and to the bottom curve when the cell is discharging. However, through the addition of a hysteresis model, a mathematical function is created, continuously moving between the two curves during charging and discharging operations. As shown in Figure 3.13 and Table 3.3, the inclusion of the hysteresis model has improved the time convergence of the SOC-NLKF algorithms, since the information acquired from OCV is much more accurate. Moreover, it has

been proven that during test simulation, the SOC estimation by NLKF with tabulated parameters never converges with absolute SOC error lower than 1 %. Instead, the inclusion of the hysteresis model allows the filter to converge, coming lower than 1 % with a mean time of 2400 s.

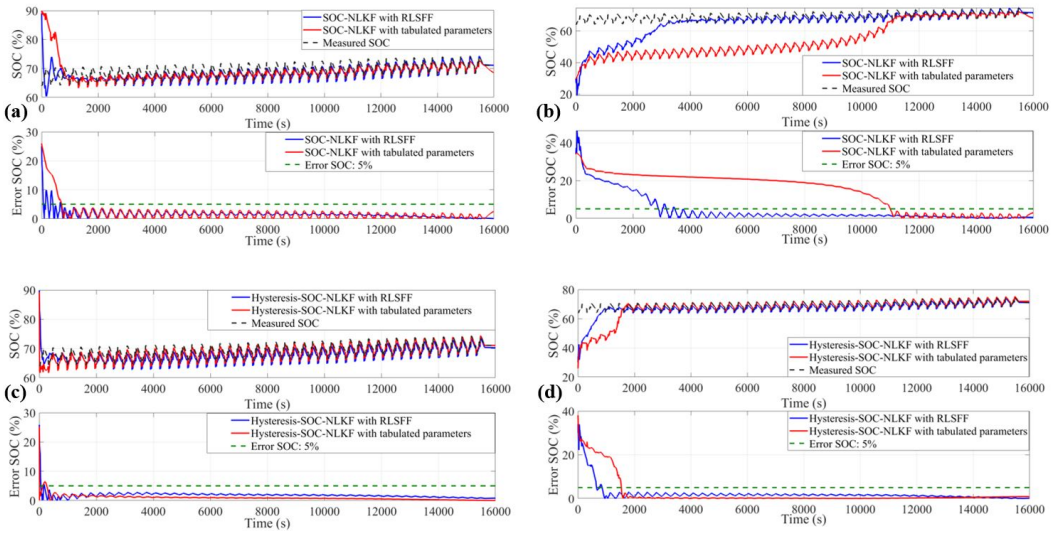

Figure 3.13: SOC estimation results by NLKFs at different SOC initial conditions: comparison between SOC-NLKFs without hysteresis model (a) or with hysteresis model (c), initial SOC estimate of 90%; comparison between SOC-NLKFs without hysteresis model (b) or with hysteresis model (d), initial SOC estimate of 30%.

Estimated SOC i.c.	**SOC-NLKF tabulated parameters**		**SOC-NLKF RLSFF**		**SOC-NLKF tabulated parameters**		**SOC-NLKF RLSFF**	
(%)	t_{conv} (s)	$e_{ss,m}$ (%)	t_{conv} (s)	$e_{ss,m}$ (%)	t_{conv} (s)	$e_{ss,m}$ (%)	t_{conv} (s)	$e_{ss,m}$ (%)
10	11290	1.23	4405	1.24	14897	1.69	6717	1.43
20	11249	1.23	7355	1.24	8083	1.14	935	1.46
30	10995	1.26	3462	1.28	1537	0.28	855	1.37
40	10369	1.31	2464	1.35	570	0.41	641	1.44
50	2833	1.29	2131	1.38	615	0.55	1491	1.56
60	572	1.40	1805	1.40	1033	0.37	908	1.46
70	5	1.43	1489	1.40	267	0.57	516	1.44
80	237	1.35	832	1.40	260	0.84	245	1.30
90	709	1.31	685	1.36	388	0.37	182	1.30
100	713	1.31	715	1.28	713	3.24	997	1.08

Table 3.3: Results of SOC estimation at the different initial conditions (i.c.) of SOC.

3.3.2 Performance at different disturb levels on measurement sensors

To define requirement specifications on sensors, in particular referring to their measurement accuracy, simulations of the same test cycle, shown in Figure 3.7, are performed adding white noise signals $n_k = [n_i, n_v]$ in voltage and current measurements. This is noticeable in the algorithm ideas represented in Figures 3.3 and 3.4. The additive noise signal is defined as a white Gaussian noise, which generates normally distributed random numbers with zero mean and an appropriate std at each time step. These signals have been added on battery voltage $n_{v,k}$ and current sensors $n_{i,k}$ to assign the uncertainties of the measurement instruments. Simulation tests are performed by considering the initial condition of the SOC estimate at 90 % or 30 %, with respect to the exact initial condition of 64 %. The respective sensor's noises considered have been set as white noise signals with zero mean and std of 0, 5 and 10 % related to battery current C-rate and nominal voltage. Results of simulation tests are represented in Table 3.4. Note that the time convergence t_{conv} was signed with the symbol ∞ when SOC estimation did not reach convergence during the test. The results obtained confirm that the estimated SOC by NLKF with the hysteresis model converges to the real SOC value with additive measurement white noise std of 5 %. In particular, adding white noise, it is notable that the NLKF with tabulated parameters converges faster than the other one. This result is due to the model's parameter update which has been perturbed by the noise itself, being recursively estimated by the RLSFF algorithm. Instead, using the tabulated parameters (LUTs), as noticeable in Figure 3.3, the parameters depend only on the estimation performed at the actual SOC.

Estimated SOC i.c.	**Noise std** n_k	**SOC-NLKF tabulated parameters**		**SOC-NLKF RLSFF**		**SOC-NLKF tabulated parameters**		**SOC-NLKF RLSFF**	
(%)	(%)	t_{conv} (s)	$e_{ss,m}$ (%)	t_{conv} (s)	$e_{ss,m}$ (%)	t_{conv} (s)	$e_{ss,m}$ (%)	t_{conv} (s)	$e_{ss,m}$ (%)
30	0	10995	1.26	3462	1.28	1537	0.28	855	1.37
30	5	∞	–	8611	2.56	2854	0.40	3808	3.41
30	10	∞	–	∞	–	∞	–	∞	–
90	0	709	1.31	685	1.36	388	0.37	182	1.30
90	5	684	0.98	5236	3.56	229	0.93	501	1.11
90	10	532	1.24	∞	–	228	0.94	∞	–

Table 3.4: Results of SOC estimation at the different initial conditions (i.c.) of SOC, additive white noise signals with zero mean and appropriate standard deviation (std) in the sensors.

3.3.3 Performance at different process disturb levels

To define requirement specifications of the control unit (A/D conversion, arithmetic operations, etc.), uncertainty of the model and preliminary calibration tests for application of the considered NLKFs, simulations are performed adding white noise signals w_k in the stochastic model (3.4) and in the battery drop voltage model (3.1). This is noticeable in the algorithm ideas represented in Figures 3.3 and 3.4. Simulation tests are performed by considering the initial condition of the SOC estimate at 90 % and 30 % respect to the exact initial condition of 64 %. The process noise considered have been set as white noise with zero mean and std of 0, 5 and 10% respect to the relative models: for stochastic model (3.4) the additive noise w_k is relative to SOC evolution, and voltage evolution concerning drop voltage model (3.1).
Results depicted in Table 3.5 shows that that the SOC-NLKF algorithm with RLSFF type is more robust than SOC-NLKF with tabulated parameters. The addition of the noise process in the case of tabulated parameters primarily indicates the non-perfect accuracy of the measurement instruments. Therefore, LUTs shown in Figure 3.3 should be calibrated with much more accurate sensors, thus allowing the NLKF to correctly estimate the battery SOC. However, by using the RLSFF method for online parameters, circuit parameters are recursively calculated online, thus allowing much better accuracy in evaluating SOC.
Summarizing, focus is dedicated to the evaluation of SOC estimators at different disturbance factor who are present in the real battery. In particular the addition of noise voltage error in measurement acquisition or in battery model parameters definition.
Dependency from temperature has not been explicitly considered. Indeed in the experimental tests it's neglected an evident room temperature variation. However, since temperature is associated with variations of battery parameters, as explained in [36] and [77], performed robustness tests give also indications to the effect of temperature intended as an external disturbance aiming to alter the behavior of observed systems. Therefore, the SOC estimators robustness at different temperatures have been evaluated assuming the variation of battery model parameters. As shown in [36] and [77], the variability of the internal resistance is estimated in the range of the 5-10 % of its nominal value. Hence, the robustness of the SOC estimators has been tested assuming a variation of the battery model parameters. Considering an additive perturbation of 10 % of battery model parameters, it is possible to verify that the estimated SOC tends to experimental one as shown in Figure 3.14 and in Table 3.6.

Estimated SOC i.c.	**Noise std** w_k	**SOC-NLKF tabulated parameters**		**SOC-NLKF RLSFF**		**SOC-NLKF tabulated parameters**		**SOC-NLKF RLSFF**	
(%)	(%)	t_{conv} (s)	$e_{ss,m}$ (%)	t_{conv} (s)	$e_{ss,m}$ (%)	t_{conv} (s)	$e_{ss,m}$ (%)	t_{conv} (s)	$e_{ss,m}$ (%)
30	0	10995	1.26	3462	1.28	1537	0.28	855	1.37
30	5	∞	–	1131	0.43	∞	–	10924	0.99
30	10	∞	–	1093	0.49	∞	–	1594	0.67
90	0	709	1.31	685	1.36	388	0.37	182	1.30
90	5	∞	–	477	0.43	∞	–	1662	0.48
90	10	∞	–	757	0.44	∞	–	359	0.51

Table 3.5: Results of SOC estimation at the different initial conditions (i.c.) of SOC, white noise signals, with zero mean and appropriate standard deviation (std), battery process disturbs in filter's block (LUTs, RLSFF filter and KF).

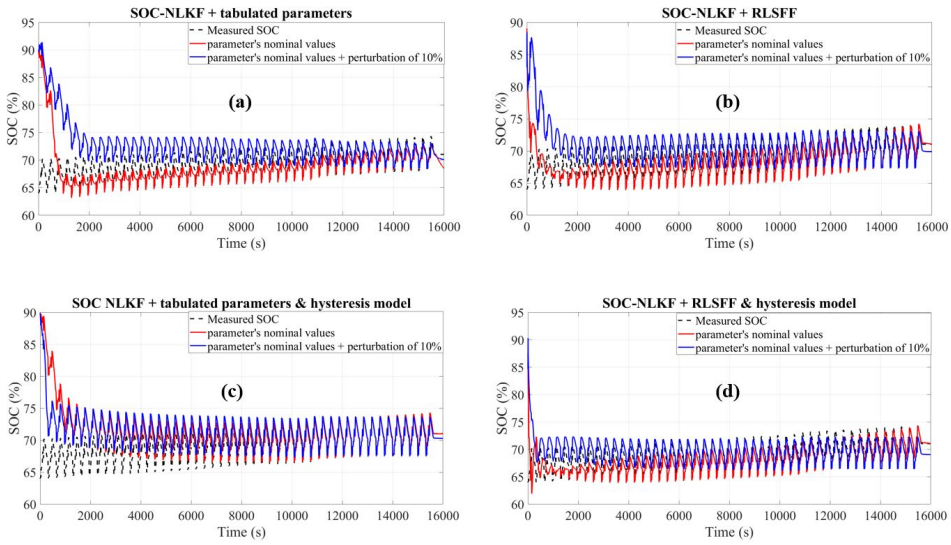

Figure 3.14: SOC estimation results by different estimators, assuming a variety of battery model parameters: (a) SOC-NLKF with tabulated parameters; (b) SOC-NLKF with RLSFF; (c) SOC-NLKF with tabulated parameters and hysteresis model; (d) SOC-NLKF with RLSFF and tabulated parameters.

3.3.4 Performance at different sampling times

One of the most important specifications assigned for any control unit is the sampling-rate. The dynamics of the battery can be well observed with a sample time of 0.1 s. In this section, the effectiveness of SOC-NLKF algorithms is evaluated, always based on the reference cycle test in Figure 3.7, under different sampling times. The results are shown in Table 3.7. In this case, it is clear that the addition of the hysteresis model has mainly improved the evaluation performed by the NLKF, as for initial SOC equal to 30 %.
However, for initial SOC equal to 90 %, evaluations performed by NLKF with

RLSFF with hysteresis model sometimes get worse increasing the sampling time. However, results have shown that the SOC evaluation on average can converge to the real SOC value within a sampling time of about 5 s, whose values can be considered rather consistent for commercially available BMS.

SOC i.c.	**Model param value**	**SOC-NLKF tabulated parameters**		**SOC-NLKF RLSFF**		**SOC-NLKF tabulated parameters**		**SOC-NLKF RLSFF**	
(%)	(%)	t_{conv} (s)	$e_{ss,m}$ (%)	t_{conv} (s)	$e_{ss,m}$ (%)	t_{conv} (s)	$e_{ss,m}$ (%)	t_{conv} (s)	$e_{ss,m}$ (%)
90	Nominal value	709	1.30	375	1.32	1278	1.72	500	1.37
90	Variying 10 % of nominal value	3225	2.05	1628	1.15	1032	1.18	207	1.24

Table 3.6: Results of SOC estimation at 90% of the initial condition (i.c.) of SOC, assuming a variation of battery model parameters (without adding sensor and process disturbs).

Estimated SOC i.c.	**Sample time**	**SOC-NLKF tabulated parameters**		**SOC-NLKF RLSFF**		**SOC-NLKF tabulated parameters**		**SOC-NLKF RLSFF**	
(%)	(s)	t_{conv} (s)	$e_{ss,m}$ (%)	t_{conv} (s)	$e_{ss,m}$ (%)	t_{conv} (s)	$e_{ss,m}$ (%)	t_{conv} (s)	$e_{ss,m}$ (%)
30	0.1	10995	1.26	3462	1.28	1537	0.28	855	1.37
30	0.5	7329	1.44	3099	0.99	1545	0.28	2216	0.52
30	1	11241	3.45	9690	1.25	1633	0.55	3210	3.32
30	5	∞	–	9290	1.82	2185	2.24	8310	2.10
30	10	∞	–	∞	–	10860	2.59	10530	2.06
90	0.1	709	1.31	685	1.36	388	0.37	182	1.30
90	0.5	4094	1.04	1362	0.83	241	0.60	742	0.64
90	1	9294	1.77	1392	2.09	271	0.98	1771	1.44
90	5	∞	–	3285	3.00	1985	3.21	6385	2.49
90	10	∞	–	11470	3.32	4200	3.45	∞	–

Table 3.7: Results of SOC estimation at the different initial conditions (i.c.) of SOC, different sampling times (without adding sensor and process disturbs).

3.3.5 SOC-NLKF algorithms conclusion

Estimation results obtained by different SOC-NLKF algorithms proposed in this work have been shown in this section. Results put in evidence the huge difficulties for SOC evaluation of the LFP cell arising from its characteristics, in particular from its extremely flat OCV-SOC curve, which requires NLKF to estimate the SOC having an accurate battery model. Results have shown that time convergence does not vary significantly related to the initial condition of estimated SOC. Algorithms correct the SOC value based on the voltage measure and, in particular, on the OCV-SOC curve. Especially in the flat area of this curve, it is difficult to find a close relationship between the OCV and SOC, combined with its hysteresis effect. This aspect can be mitigated by the introduction of the hysteresis property inside the battery model, to reduce the NLKF time convergence. This is very clear by observing simulation results where additional disturb factors are considered noise, showing that the addition of the hysteresis model improves KF performance.
Finally, the two filters equipped with the hysteresis model (tabulated parameters or online calibration tools, such as RLSFF method) are similar in terms of performance. However, RLSFF has proved much more flexibility, since it requires fewer calibration data, typically not available from the manufacturer and obtainable only through ad-hoc experimental tests. Moreover, RLSFF method, since it identifies and updates the battery model every step time, adapts the model to the real battery, which can be different to the others due to manufacturing. In addition, RLSFF requires less static memory than the tabulated parameter's method.
A part of this work was presented in the EEEIC International Conference on Environment and Electrical Engineering in the year 2018, in Palermo [37]. Then, this work was extended for a publication in a Journal papers. Finally, this work was published by Journal of Systems and Control Engineering in the year 2020 [69].

Chapter 4

Real-time battery state of health diagnosis using electrochemical impedance spectroscopy fast test

The final chapter of this PhD thesis presents a new diagnostic method aimed at detecting battery SOH using fast impedance measurements. Key factor is the application of a broadband current signal excitation on the battery; for the application here presented, a pseudo-random binary sequence (PRBS) excitation is adopted. Hence, a low-cost hardware prototype for PRBS excitation was developed. By current and voltage measurements, a frequency-domain nonparametric identification is carried out in the post-processing phase. To demonstrate the functionalities of the methodology proposed, the EIG cells at different SOHs, due to their past history (check Tables 2.3 and 2.6) have been subjected to the spectroscopy (EIS) test. Finally, impedance measurements have been processed: the key step being the clustering of impedance data (represented in Nyquist diagram) in different rectangular areas, which are related to actual SOH. The performed experimental test results showed the possibility to determine frequency points in which the impedance measurements dramatically change due to different cell SOH; as a consequence, these peculiar frequencies can be adopted as reference for cluster separation. According to the results presented in this section, the proposed method is sufficiently accurate and is a promising solution for embedded diagnostic of battery SOH thanks to its simplicity and speed. The remainder of this chapter is structured as follows. Section 4.1 describes the proposed method including requirements, indicators, and excitation signal characteristics. Sections 4.2 and 4.3 describe the low-cost hardware for programmable PRBS excitation and the EIS laboratory test setup. Sections 4.4 and 4.5 include the results obtained by aged cells testing and the data processing procedure. This part of PhD activity led to publish some conference's paper: Ref. [65] describes the details about the use of PRBS as signal excitation to perform fast and reliable EIS test. Ref. [72] presents the low-cost PRBS generator prototype. Ref. [73] shows the impedance estimation results obtained for the EIG cells at different SOHs. Modeling battery as EEC with

constant phase element components (check Figure 2.31), many circuit parameters showed interesting trends linearly comparable to the decreasing of battery SOH. the real-time SOH diagnostic methodology, discussed in this chapter, is published in Journal of Energy Storage [74].

4.1 General principle for nonparametric identification

4.1.1 System requirements

To perform impedance measurements based on EIS test, the battery system under test must be assumed and validated as LTI dynamic system. The linearity property can be assumed if the system is submitted to a small current excitation. However, a very small current perturbation causes noisy voltage response. Hence, it's important to select an appropriate signal excitation: it must not be too large because it would induce a non-linear response of the system, and not too small because it would induce noisy responses. The time-invariant property can be assumed if the parameters, which define the battery system, are not changing with time. The main causes for time-variance in the battery system are the variations of temperature, SOC, current excitation (in terms of amplitude and sign), and finally aging. Moreover, if the battery voltage is in a transient state and has not reached its steady state, the system is considered as time-variant. The effects of time-variance in EIS measurements are noticeable in low frequency and are shown in [112][113]. Hence, to avoid impedance errors related to time-variant system behavior, sufficiently long rest time is required before the EIS test start. Moreover, influence factors, especially temperature, must be stable during the test. If the LTI assumptions are validated during the EIS test, battery impedance can be represented by the discrete-Fourier transform (DFT):

$$Z(k) = \sum_{n=0}^{N-1} z[n] e^{-j\frac{2\pi}{N}kn} \tag{4.1}$$

Where $z[n]$ denotes the impedance impulse response in the time step $n = 0, ..., N-1$. The variable $k \in [-1/2, 1/2]$ denotes the normalized frequency. Given the following assumptions:

- Battery system is bounded-input bounded-output (BIBO) stable
- Current signal excitation, used for the EIS test, is a periodic signal or a signal realization of a stationary stochastic process

If the assumptions are validated, the steady voltage response is a signal realization of a stationary stochastic process [32]. In conclusion, the impedance transfer function estimate Z corresponds to the ratio between the two following spectral estimates:

$$Z(k) = \frac{\Phi_{vi}(k)}{\Phi_{ii}(k)} \tag{4.2}$$

$\Phi_{ii}(k)$ denotes the battery current input power spectral density (PSD), and $\Phi_{vi}(k)$ is the cross-PSD (CPSD) of the battery voltage-current signal, computed by the

voltage and current DFTs $V(k)$, and $I(k)$:

$$\begin{aligned} \Phi_{vi}(k) &= aV(k)I^*(k) \\ \Phi_{ii}(k) &= aI(k)I^*(k) \end{aligned} \tag{4.3}$$

Where a is a normalization factor, * denotes complex conjugation.

4.1.2 Quality indicators

The control of accuracy of impedance measurements based on EIS test is fundamental to have a reliable monitoring of the change of electrochemical properties of the battery and, in this case, a reliable diagnostic of its SOH. The validity of EIS measurements can be evaluated by using different methods discussed in the literature [112]-[117]. As mentioned, the battery system's LTI property must be validated, and, given a current input, the observed output voltage response must not be noisy. One of the most common methods to check the conservation of LTI property is the Kramers-Kronig relation validity test [112][113]. The Kramers-Kronig relation dictates that real and imaginary parts are interdependent, presented in the Kramers-Kronig (KK) transform integrals [112], for a LTI and causal system. An interesting KK test algorithm is employed to validate the EIS measurements and it is presented in [113]. The drawback of this method is the high computational effort. An alternative approach is the monitoring of the ordinary coherence value in frequency. Given the spectral estimates $\Phi_{ii}(k)$, $\Phi_{vv}(k)$ $\Phi_{vi}(k)$, ordinary coherence function [114][115] at the normalized frequency k is defined as:

$$\gamma_{vi}^2 = \frac{|\Phi_{vi}(k)|^2}{\Phi_{ii}(k)\Phi_{vv}(k)} \tag{4.4}$$

From the inequality $|\Phi_{vi}(k)|^2 < \Phi_{ii}(k)\Phi_{vv}(k)$ for each frequency k [115], it follows that the ordinary coherence is bounded between 0 and 1. This quality indicator can be viewed as the correlation coefficient between the input and output sequences for every k: if the current input is linearly related to the voltage output, the ordinary coherence $\gamma_{vi}^2 = 1$; if the input is completely unrelated with output, $\gamma_{vi}^2 = 0$; if the coherence is greater than 0 and less than 1, the input-output may be in part linearly related, but also real system may contain other inputs, otherwise measurements acquired may be noisy. Indeed the noise could be estimated by the knowledge of system's ordinary coherence: noise PSD Φ_{mm} is estimated by the coherence in [115] and evaluated according to the following equation:

$$\Phi_{mm}(k) = (1 - \gamma_{vi}^2(k))\Phi_{vv}(k) \tag{4.5}$$

According to (4.5), the ordinary coherence is a useful indicator to evaluate the output signal-to-noise ratio (SNR) reproduced by the system analyzed:

$$SNR(k) = \frac{\gamma_{vi}^2(k)}{(1 - \gamma_{vi}^2(k))} \tag{4.6}$$

In conclusion, when $\gamma_{vi}^2(k) \to 1$, input and output are strong correlated and $SNR \to \infty$. In this case, the influence of the noise in the output signal is negligible, and the LTI model's assumption for the system analyzed is totally justified.

When $\gamma^2_{vi}(k) \to 0$, input and output are unrelated and $SNR \to 0$. In this case, output signal is strongly dominated by the influence of noise, hence, the LTI model's assumption is not justified.
Another interesting property of the ordinary coherence is that it is closely related to estimation errors obtained when identifying the battery system. This is usually used to compute confidence limits for different spectral estimators [32].

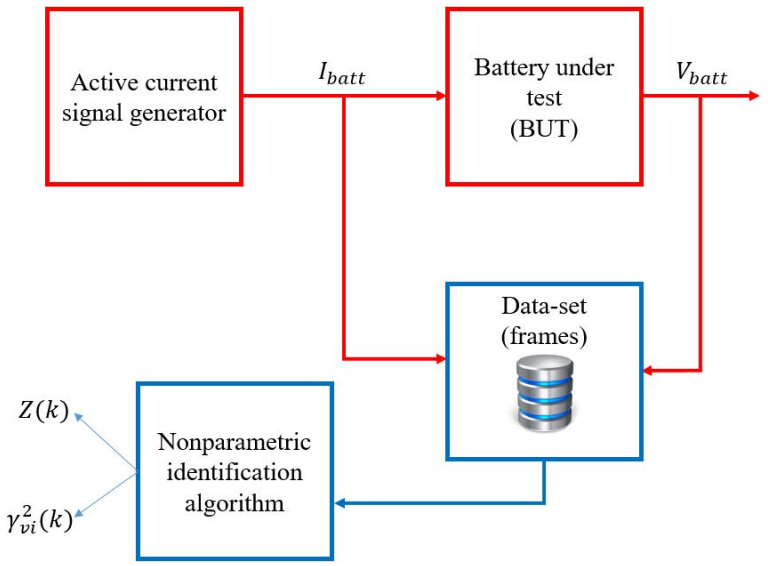

Figure 4.1: Active EIS test method: red acquired measurements and blue computed data-set.

4.1.3 Excitation signal classes

The general principle of a nonparametric identification is explained by the block diagram shown in Figure 4.1. Exciting the battery cell in current, and measuring battery voltage, data are saved in several frames of same data length. Then, a spectral density identification algorithm in frequency domain, e.g. Welch estimator [116], is employed to estimate $\Phi_{ii}(k)$, $\Phi_{vv}(k)$, $\Phi_{vi}(k)$. Finally, impedance estimation and the respective ordinary coherence are evaluated by using (4.2) and (4.4).
As mentioned in the introduction, broadband input signals are used for system identification in a wide frequency range, reducing test time. Three different classes of broadband signals have been considered in literature [32][115]:

- **Random signals:** filtered Gaussian white noise signals.
- **Transient signals**: pulse or burst signals.
- **Periodic signals**: multi-sine, pseudo-random signals.

The white noise presents a flat PSD over all frequencies; however, its signal generation requires a complex hardware realization. Moreover, it suffers from leakage problem [63], hence a probability of a highly reduced SNR at some randomly located frequencies.

Transient signals are used for fast system identification and they show a simple hardware implementation. However, they present a high crest-factor [32], inducing to high energy consumption during impedance estimation. Periodic signals represent the most interesting class to perform active spectroscopy test. Indeed, periodic signals exhibit a low crest factor [32][114]. In this way, an accurate impedance estimation can be performed with low energy consumption. Finally, the spectral content of periodic signals can be optimized to prevent harmonic distortions due to leakage problem [115]. One of the most popular periodic signals used in active EIS is the multi-sine signal. This signal is a sum of sine waves which frequency corresponds to the desired discrete set of frequencies measured, with random phase. The multi-sine excitation approach offers more accurate EIS measurements, as demonstrated in [62]. Pseudo-random sequences (PRS) family is an attractive alternative, due to their low complexity, reduced test time, and good accuracy. However PRS excitation leads to slightly less accurate results than multi-sine excitation. Despite this, the generation of multi-sine, i.e. sine waves with different frequency or multisine signals requires advanced electronic generators; instead for pseudo-random family only a shift-register of n-memories is required. For more details, check the next section.

4.1.4 Pseudo Random Binary Sequence (PRBS)

PRBS is a discrete-time periodic signal that switches between two logic levels. Therefore, it is a square wave signal. One of the biggest advantages of this signal is the simply hardware implementation. Indeed PRBS is generated considering a closed-loop shift register configuration of m memories in series, requiring a very simple hardware implementation: the block system is depicted in Figure 4.2. Denoted by the output variable u_t, PRBS is generated by referring to the following equation:

$$u_t = \text{rem}(a_1 u_{t-1} + a_2 u_{t-2} + ... + a_m u_{t-m}, 2) \tag{4.7}$$

Where $\text{rem}(x, 2)$ is the modulo-2 addition on x [32], and a_i is the i-gain factor that takes integer values 0,1, for $i = 1, 2, ..., m$. The vector of past inputs $[u_{t-1}, u_{t-2}, ..., u_{t-m}]$ can only assume 2^m different values. Thus, the input signal u_t is periodic with a period of at most 2^m. In [32] it's proven that PRBS signal can have a maximum period of $M = 2^m - 1$ using an appropriate combination of gain factors vectors $[a_1, a_2, ..., a_m]$. Considering that block memories of shift register are initialized as proposed in [32], PRBS has properties similar to those of a white noise signal in the frequency domain. This is a clear advantage since it's possible to excite the system over a wide bandwidth, accelerating testing procedures. Indeed, an interesting property of PRBS is represented by its auto-covariance function:

$$\tilde{R}_u(\tau) = \frac{1}{M} \sum_{t}^{M} u(t+\tau)u(t) = \begin{cases} A^2 & \tau = 0, \pm M, \pm 2M, ... \\ -\dfrac{A^2}{M} & \text{else} \end{cases} \tag{4.8}$$

It's noticeable that if the period of the PRBS M is bigger, the function is more near that white noise auto-covariance. Equation (4.8) doesn't denote exactly the auto-covariance function of PRBS signal, because its mean value is not exactly zero. In [32] the spectrum expression of PRBS of amplitude A is in according to

the following equation, where ω corresponds to its angular frequency:

$$\Phi_{uu}(\omega) = \frac{2\pi A}{M} \sum_{i=1}^{M-1} \delta(\omega - \frac{2\pi i}{M}) \tag{4.9}$$

Where δ is the Dirac delta function. By (4.9), in the angular frequency region $[-\pi, \pi]$ there will be $M-1$ frequency peaks. Therefore, considering M value bigger, so increasing the number of the shift registers m, the PSD of PRBS signal is flatter and it is similar to the PSD of white noise signal. This deduction is confirmed by simulating PRBS signal at different number of shift registers and extracting its PSD, as shown in Figure 4.3 and demonstrated in my previous work [65].
In this thesis, the number $m = 10$ of registers, hence a period of $M = 1023$ samples, is chosen for the PRBS generator used for the EIS test. Therefore, the PRBS with a period of $M = 1023$ samples has a band-limited flat PSD, as demonstrated in Figure 4.3. In [114] it is demonstrated that the PRBS presents an almost flat spectrum over the frequency band $[f_c/m, f_c]$. The parameter f_c denote the clock frequency at which the input PRBS u_t is synchronized. Considering $m = 10$ in this work, over one frequency decade is observed. It's recommended that the choice of a sampling frequency f_s should be ten times the maximum frequency band. This last consideration is advisable for system identification in the frequency domain [32][114].

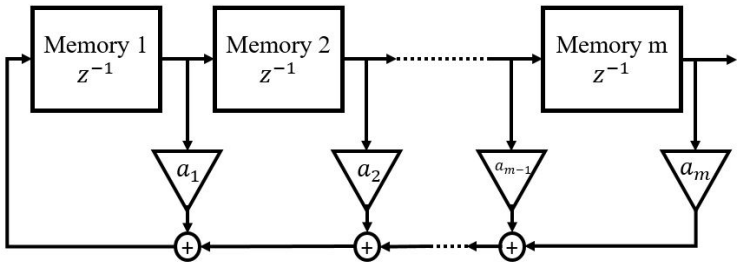

Figure 4.2: PRBS generator's circuit.

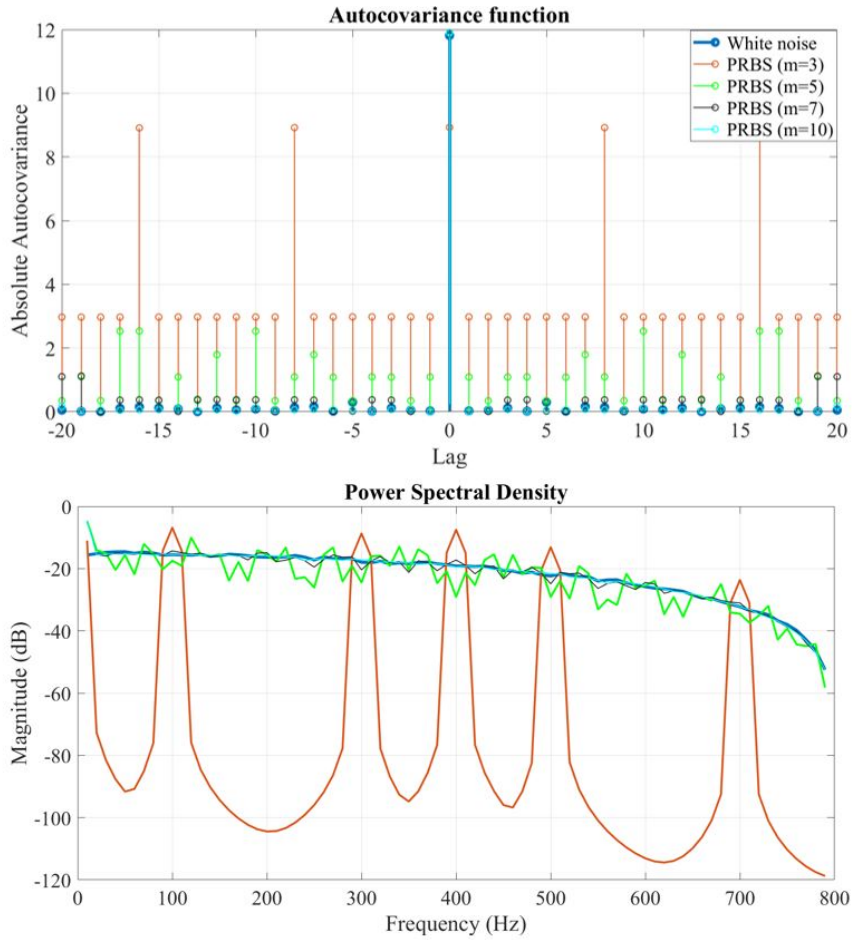

Figure 4.3: Autocovariance (top) and PSD (bottom) function of PRBS signal using different number of shift registers. Simulation performed in Matlab/Simulink.

4.2 Development of a low-cost hardware for fast EIS test

In order to perform fast and reliable spectroscopy test, in discharging phase, with low energy consumption to the battery, an innovative electronic PRBS generator was realized in this PhD thesis, made up of a low-cost hardware. The core of the proposed prototype consists of the use of a Texas Instrument development board that can be programmed in code composer studio environment or using Matlab/Simulink target compiler, downloading the add-on library "Embedded Coder Support Package for Texas Instrument". The system proposed can generate PRBS at different sample periods, clock frequencies and current amplitudes. To check the accuracy of impedance measurements, a second power circuit composed of passive components is inserted in parallel. Switching the PRBS generation in this second circuit, impedance measurements are validated experimentally by comparing reference and experimental impedance data. This prototype was presented at the

MELECON 2020 international conference [72]. Moreover, the prototype, proposed in this section, won the award of 3^{rd} edition of the SSE Challenge Engineering for Industry 4.0 (2019).

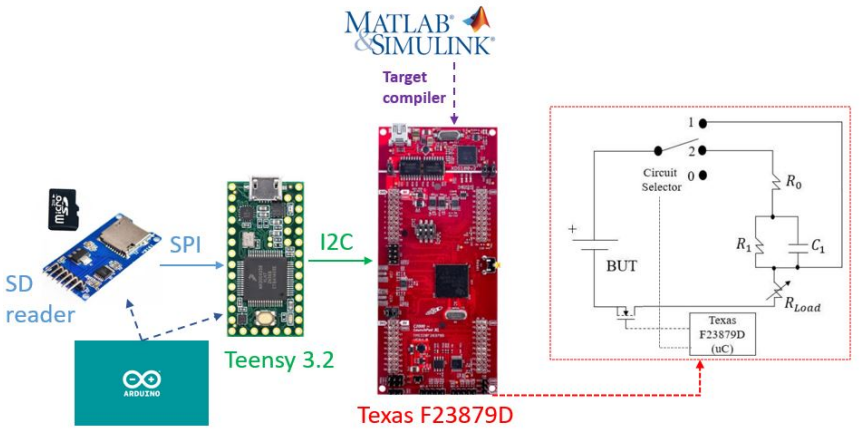

Figure 4.4: Block scheme of the PRBS generator.

4.2.1 General description

Figure 4.4 shows an implementation scheme of the proposed PRBS generator: all the spectroscopy tests are managed using a Texas instrument (TI) development board of the "Delfino" series: exactly the LAUNCHXL-F28379D. This development board belongs to the 32 bit microcontroller family. The microprocessor is the TMS320F28379D: a 200 Mhz of clock frequency, dual core, 1 MB of flash memory, several I/O ports including 16-12 bit ADCs and 12-bit DACs, which are configurable as hardware interrupts, PWM ports and as some peripherals communicating with other devices in I2C, SPI, UART and CAN [118]. This development board was used in the University of Florence, in past, for motor drives [119], but, considering available memory and computational resources, it was extensively used also for hardware in the loop testing [120] thanks to good DSP performances. In this work, the tasks which TI board should satisfy are the following:

- **Control the PRBS generation:** Battery under test (BUT) is connected to the power circuit shown in Figure 4.4. The periodic PRBS signal data was first stored in an external micro SD card. The same SD card uploads the PRBS data to the TI board, which generates the corresponding PRBS voltage signal to the transistor, shown in Figure 4.4, which turns ON and OFF the power circuit. The interface between SD card reader and TI board is performed through the Teensy 3.2 board: a development board with a 72 MHz microprocessor, which is easily programmed through the Arduino IDE. Respect to the prototype presented in [72], the PRBS generator is now directly implemented in the TI board. Since PRBS can be generated by a $m = 10$ memories in series in a configuration of shift register, as shown in Figure 4.2, its implementation in Simulink or in code composer studio becomes trivial. The variable load resistance R_{load} is connected to the battery

under test. This resistance is inserted in order to select the desired current amplitude of discharging PRBS generator.

- **Control the different circuit tests:** TI board also controls the circuit selector, which is made up of a relay system, in order to have the possibility to conduct two different tests by switching manually. Turning the circuit selector in 0, power circuits are open. If the circuit is selected in 1, EIS test is performed on the BUT; else, if the circuit is selected in 2, a reference sample impedance is inserted in series with the previous circuit. This last circuit will be used to validate impedance measurements and check the instrument accuracy, shown in the next section. A third parallel circuit was considered in the prototype, in which battery has a continuous discharge by inserting a second load resistance. But this option is inherent to this work.

Once the device is programmed, it can be used safely also avoiding any additional communication with the host PC, since the device is provided of a control panel. The control panel assures a known controllable and safe behaviour of the testing equipment through the usage of command button and led for state feedback. The control panel and the main components of the prototype are depicted in the Figure 4.5 and in Table 4.1.

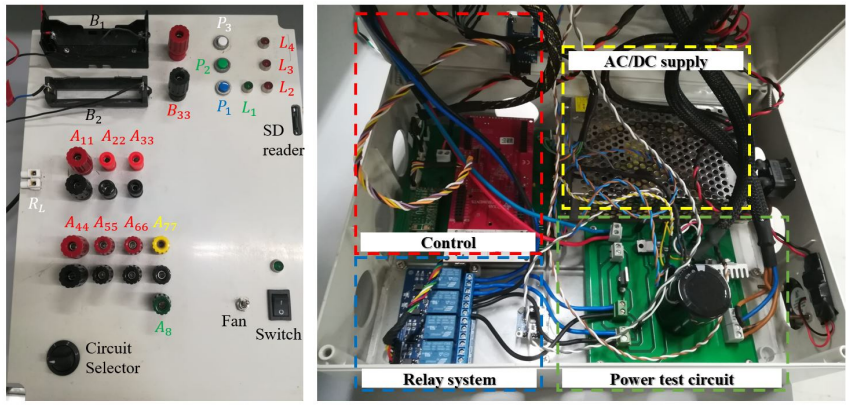

Figure 4.5: PRBS generator prototype: (top) control panel, (bottom) Internal structure.

4.2.2 Embedded code for current PRBS generation

The embedded code for TI board, which represents the core of the PRBS generator prototype, was designed in order to satisfy the following statements depicted in the flow-chart, shown in Figure 4.6. As mentioned previously, TI development board series can be directly programmed using Matlab-Simulink through a supported target compiler, which automatically generates C code, and actives the general purpose I/O (GPIO) ports and peripherals. This thanks to the use of the add-on library called "Embedded Coder support package for Texas Instrument C2000 processors" [121]. In this work, TI board was programmed in Simulink: the main file is represented in Figure 4.7, by following the statements shown in Figure 4.6. TI board receives the PRBS data by the SD card and it generates the same PRBS

signal with voltage level of 0, 3.3 V. The communication between SD-card and TI board is well illustrated in Figure 4.4. PRBS data is saved in a text file with extension .Dat in the SD card. Teensy device, which represents the interface between the SD-card and the TI board, communicates with SD-card through the SPI protocol. In this case Teensy master, programmed with Arduino IDE requires to the SD-card slave the text file by using the library SD.h. TI board, configured as master, requires to the slave Teensy device, with appropriate address (0x08) the PRBS data, by using the I2C protocol and the library Wire.h of Arduino IDE. In particular, TI board, through the use of "C28xI2C Receive" requires 9 Bytes the address overcited, then, Teensy slave answer to Master's request and it sends the 9 Bytes by recalling the function Wire.OnRequest(). The information represents the hour (1 Byte), minute (1 Byte) and second (1 Byte) of data sent, the PRBS data (4 Byte) and the respective dimension (2 Byte). All the tests are realized by using "Enabled subsystems" which are managed by the GPIO connected to the button represented in the control panel (P1, P2, P3). PRBS generation is enabled by pushing the button P2. When PRBS data, which is sent by I2C port, is completely saved in a target memory, an event is generated. This event enables the generation of data sequence on the DAC port (Low as 0 and High as 4095). This code gives the possibility to the prototype to perform PRBS generation in the stand-alone mode.

Name	Action
Led1	Battery discharge
Led2	Temporized waiting between tests
Led3	PRBS generation (blinking in the first 10 s, EIS test starts after 10 s)
Led4	Error on SD card
P1	Start CC discharge test
P2	Start PRBS test
P3	SD card data refresh
A11	Battery voltage
A22	Drain-source transistor voltage
A33	Second load resistance for CC discharge test
A44	Resistance voltage R_{Load}
A55	Sample impedance voltage Z_{sample}
A66	Drop voltage on $Z_{sample} + R_{Load}$
A77	PRBS generation
A8	TI trigger line
B1	26650 cylindrical cell
B2	181650 cylindrical cell
B33	Different cell's design type
RL	Load resistance R_{Load}

Table 4.1: Brief description of the laboratory equipment used

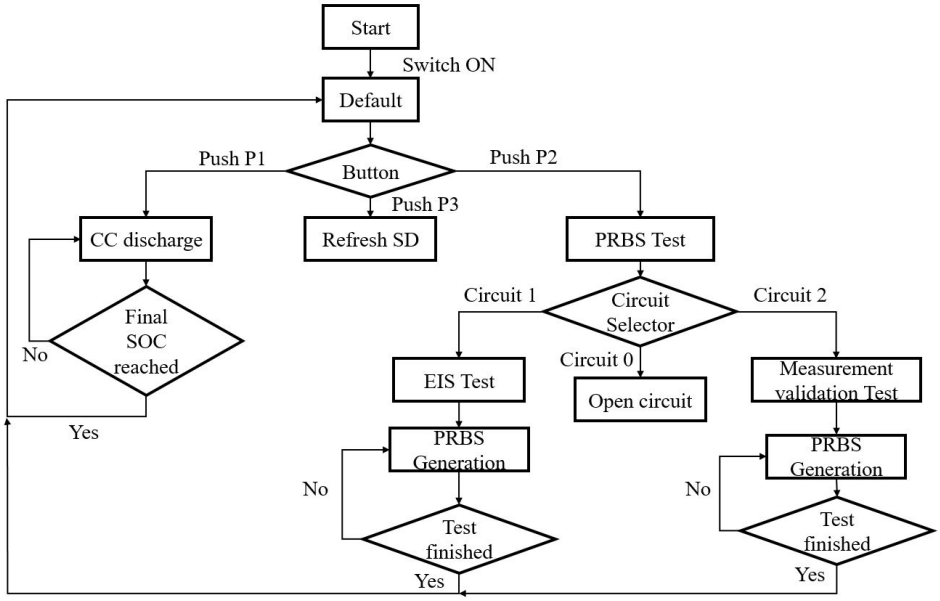

Figure 4.6: Tasks managed by TI microcontroller in the PRBS generator prototype: flow-chart.

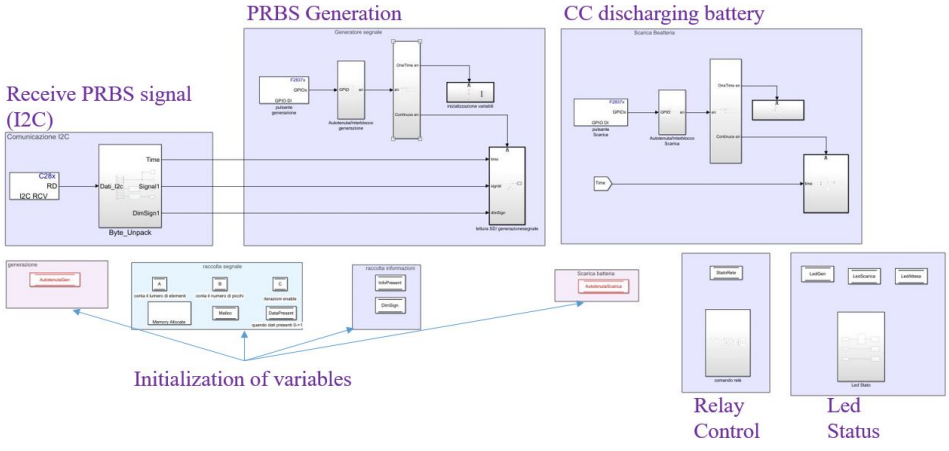

Figure 4.7: Embedded code deployed to TI board by using Simulink.

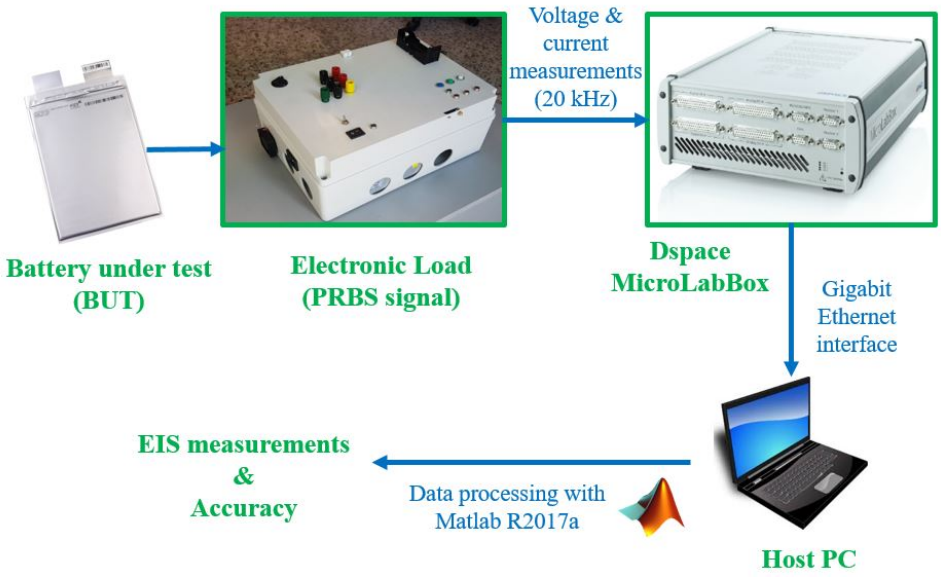

Figure 4.8: Laboratory EIS test setup for cell system on the right, electronic circuit of PRBS current generator on the left.

4.3 Battery EIS test setup and validation results

4.3.1 Laboratory setup and test procedure

The scheme of the proposed laboratory EIS test setup for battery cell system is depicted in Figure 4.8. Testing procedure, for system identification in the frequency domain, is depicted in the block scheme of Figure 4.1. In this case, EIS test consists of exciting the battery in current with the periodic PRBS signal, using the PRBS generator device, discussed in the previous section. During the EIS test, battery voltage and current are measured and acquired by the dSPACE MicroLabBox at a sampling frequency of 20 kHz, which is ten times the maximum EIS frequency band of interest for SOH diagnosis. In order to check that EIS test is not affected by external factors, room and battery surface temperature are measured, with a sample time of 1 s. When the EIS tests are finished, voltage and current data are processed to evaluate impedance (4.2) and coherence (4.4), following the approach explained as following.

The charged battery (SOC=100%) is subjected to different EIS tests. Research works [38]-[55] investigated the battery SOH changes by observing impedance data in the frequency range approximately from mHz to kHz. In this work, battery impedance is evaluated in the frequency band [4,1600] Hz. In this specific range, research works [50]-[55] depicted that SOH characterizes the change of impedance curve, such as ohmic, charge-transfer, and SEI resistance's parameter. Moreover, fast EIS tests can be carried out in this range. As mentioned, the PRBS, with $m = 10$ registers, has a flat spectrum in about one-decade frequency, based on the clock frequency f_c. Since the band of interest is [4,1600] Hz, the battery impedance spectrum will be estimated by taking three consecutive PRBS tests at different clock frequencies into consideration: 50, 500, and 4000 Hz. More details

about PRBS are illustrated in Table 4.2.
Tests are repeated considering various SOC and amplitude levels of PRBS current (C-rate), described in Table 4.3.
The experimental test protocol is illustrated in Figure 4.9. Tests are performed starting from the highest SOC to the lower ones. Assuming that all EIS tests performed require less than 1% of battery SOC consumed, the battery is discharged at the rate of discharge of C/2 until it losses the remaining energy that is needed to reach the next desired SOC level. After a rest time of 1 h, to allow the battery voltage to reach its steady-state, EIS tests are carried out again. The experimental test is finished when the EIS tests are performed on the battery at the end of the discharge (about 2%). Based on battery voltage and current measurements, with a sample time of 20 kHz, battery impedance is evaluated in the frequency range [4,1600] Hz: 21 linearly spaced frequency points are extracted for every PRBS test at different clock frequency, as shown in Table 4.9. The guideline for appropriate bandwidth measured, by using the PRBS, is given in [114] equalling to $0.4f_c$. By results shown in Figure 4.11, this constraint was maintained for the 4 kHz PRBS in this work, whereas the same constraint was relaxed considering the 50 and 500 Hz PRBS excitation.
After each EIS test, voltage and current measurements data are processed: the respective PSD and CPSD are computed by applying the Welch periodograms [116]: voltage and current measurement signals are split into disjointed L_f frames of length N_f. Then, the voltage and current Fast Fourier transforms of every frame are computed according to (4.1), and multiplied by using the Hamming window function. Hence the PSD and CPSD are computed according to (4.3), finally, the Welch periodogram estimator evaluates the PSD and CPSD computing the following mean value:

$$\begin{aligned}
\Phi_{ii}(k) &= \frac{a}{L_f}\sum_{j=1}^{L_f}\Phi_{ii,w,j}(k) \\
\Phi_{vv}(k) &= \frac{a}{L_f}\sum_{j=1}^{L_f}\Phi_{vv,w,j}(k) \\
\Phi_{vi}(k) &= \frac{a}{L_f}\sum_{j=1}^{L_f}\Phi_{vi,w,j}(k)
\end{aligned} \tag{4.10}$$

Once the PSDs have been computed, impedance values are estimated according to (4.2). The estimation accuracy is evaluated by the calculation of ordinary coherence, in according to (4.4). The global structure of impedance estimation algorithm is summarized in the Figure 4.10.

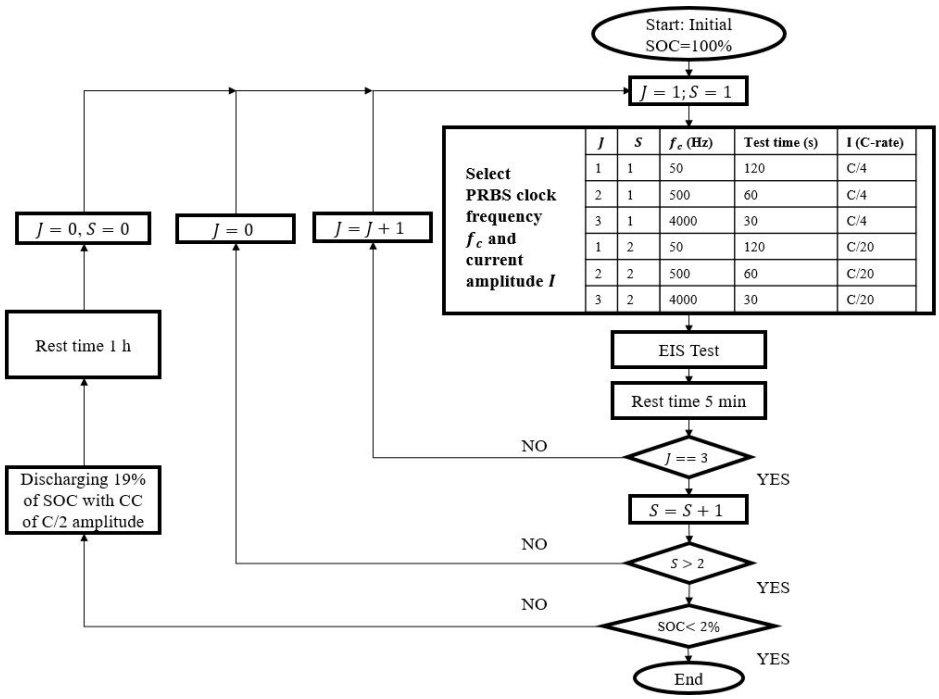

Figure 4.9: Structure of the EIS test procedure.

PRBS clock frequency (Hz)	**Period time (s)**	**Test duration time (s)**	**Number of impedance measurements**	**Frequency resolution (Hz)**	**Frequency band (Hz)**
50	20.6	125	21	1.4	[4,40]
500	2.6	60	21	13.25	[53,400]
4000	0.256	10	21	82.50	[450,1600]

Table 4.2: Impedance measurement specification processed after EIS test

Parameters change	**Values time (s)**	**Number of test repetition**
PRBS clock freq. f_c	[50,500,4000] Hz	3
Discharging current C-rate	[C/3,C/4,C/5,C/6,C/20,C/25]	3
Battery SOC	[100,80,60,40,20,2]%	3

Table 4.3: EIS Test specifications performed on each single cell (about 3000 tests)

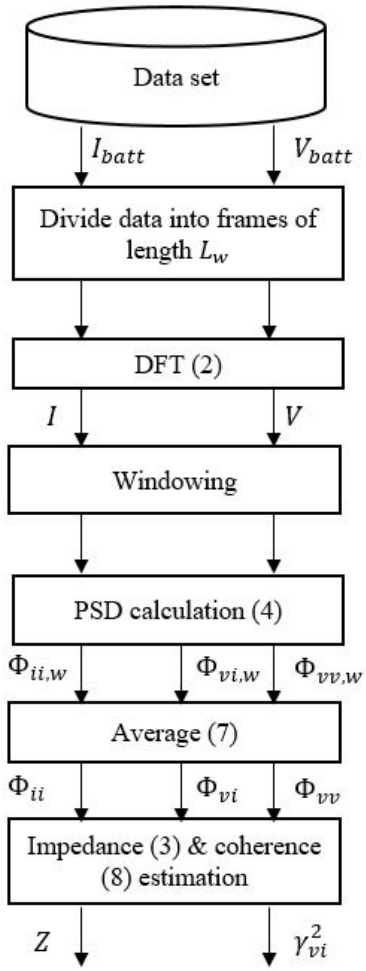

Figure 4.10: Structure of the impedance and coherence estimation after EIS test.

4.3.2 Validation of battery impedance estimate

As mentioned in the previous section, the accuracy of EIS measurements is validated considering the electrical equivalent circuit given in Figure 4.4, switching the circuit selector in 2. Referring to Figure 4.4, the circuit configuration, composed by the passive circuit elements R_0, R_1, R_2 defines the reference sample impedance. The circuit parameters are selected to describe a portion of a semi-circle. The resistance $R_0 = 1\ \Omega\ \pm 5\%$ is in series with RC group in parallel, composed by $R_1 = 50$ mΩ $\pm 5\%$ and $C_1 = 0.01$ F $\pm 20\%$, considering a parasitic resistance $R_p = 10$ mΩ $\pm 5\%$ in series to capacitive element, given by the manufacturer. The battery under test is the 20 Ah EIG pouch cell presented in Chapter 2 and mentioned before. For each PRBS signal at a different clock frequency, impedance measurements are performed at various current amplitudes and different SOCs, shown in Table 4.3. This leads to a large number of EIS tests, in which impedance and coherence are computed. Impedance estimate results are compared with the theoretical impedance in

the frequency range of [4,1600] Hz. The results demonstrated that measurements of sample impedance at different SOCs are very similar. Therefore, in this PhD thesis it will neglect this difference when discussing the validation of the sample impedance estimation. The corresponding estimated coherence, at different PRBS input signal, is depicted in Figure 4.11, whereas the estimated sample impedance is depicted in Figure 4.12. The estimated ordinary coherence is close to 1 all over the frequency band. Therefore, it's inferable by results obtained in Figure 4.11 that the battery under test can be considered as LTI system, hence sample impedance can be well estimated. The results shown in Figure 4.12 demonstrate that the real and imaginary part of the sample impedance measurement of the laboratory test setup's accuracy slightly decreases when the clock frequency of the PRBS signal is increasing, especially during the test with a clock frequency $f_c = 4$ kHz. This is noticeable also observing the coherence estimated in Figure 4.11. Finally, the results of measured sample impedance had shown a well-known bias estimation error of 5%, which is corrected for this work. A similar bias estimation error is obtained in [117].

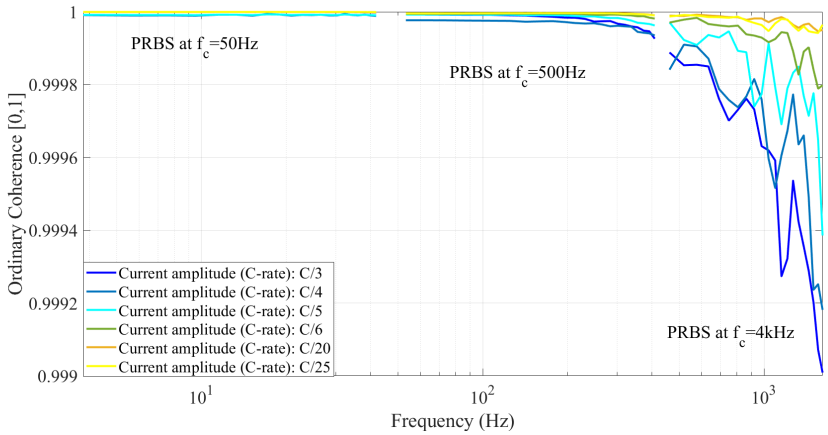

Figure 4.11: Ordinary coherence obtained during EIS test validation (estimation of sample impedance). Battery under test is at 60 % of SOC.

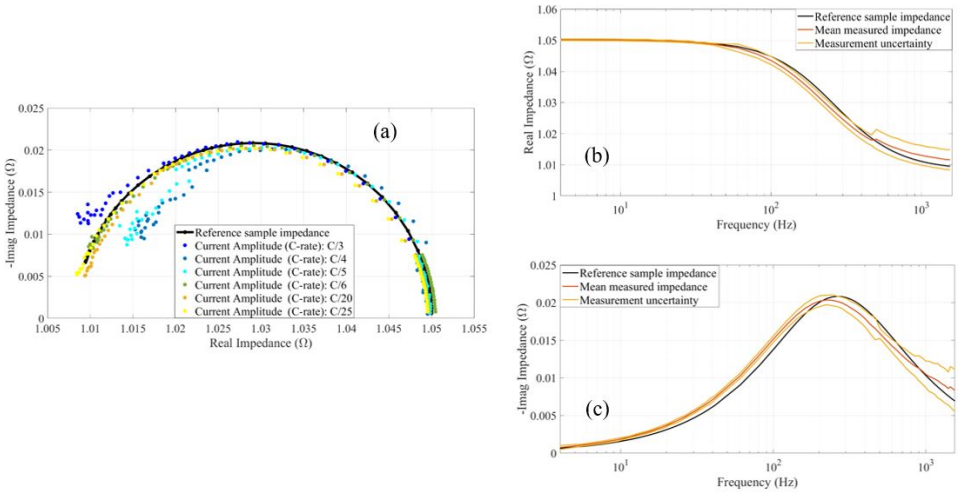

Figure 4.12: EIS test validation results: comparison between reference sample impedance curve and experimental measurements performed at different current C-Rate. (a) Nyquist plot, (b) Real impedance and (c) Imaginary impedance vs frequency. Battery under test is at 60 % of SOC.

4.3.3 Impedance measurements results obtained on the beginning of life EIG cell

The battery impedance estimation is performed considering the equivalent circuit given in Figure 4.8, switching the circuit selector in 1. In this section, the EIG cell at the beginning of life (SOH=100%) is under test. EIS results are depicted in Figure 4.13.
It's clear that all the battery impedance measurements are about in the interval of 2 mΩ, in the real part, and 0.5 mΩ, in the imaginary part. These intervals are shorter than the sample impedance measurements in the previous experiment. Therefore, the external noise sources could strongly affect the EIS measurements, decreasing the ordinary coherence. As just mentioned, noise contributions can be minimized by increasing the excitation power when an improved coherence is reached, as shown in Figure 4.14. The battery impedance curves estimated and given in Figure 4.13 (top) show a slight difference when changing the current discharging amplitude. Instead, results given in Figure 4.13 (bottom) show that there is a drastic change of impedance curve when the battery is at the end of discharge, confirmed also in [50][53].

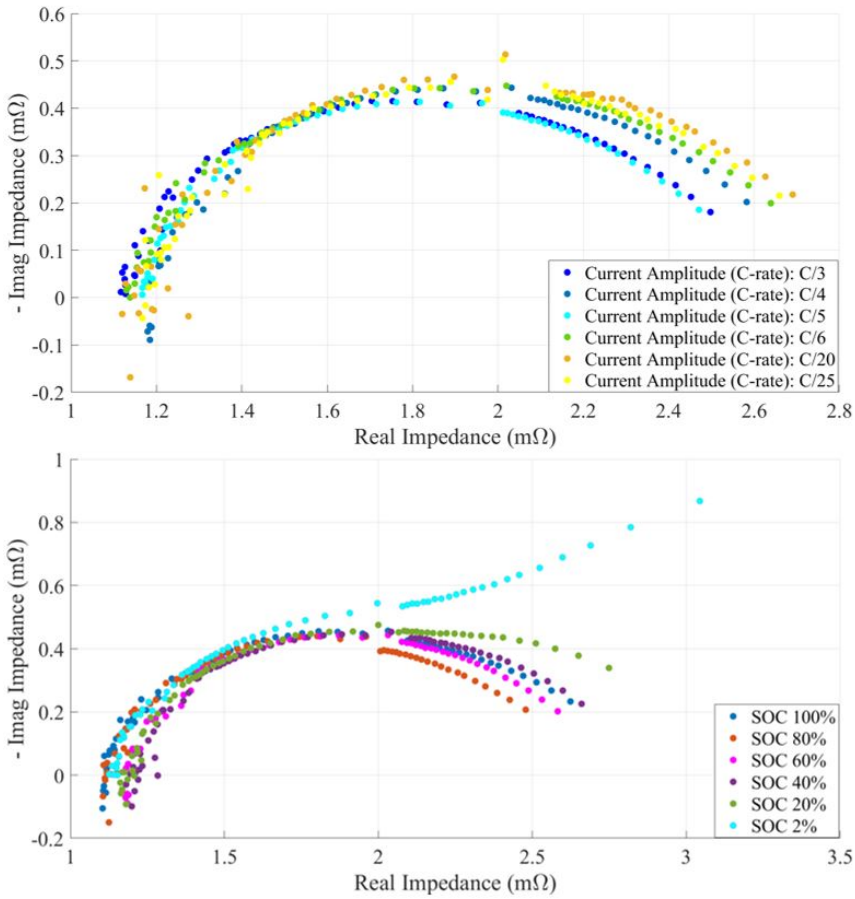

Figure 4.13: Impedance measurements on the beginning of life EIG cell by using current PRBS excitation at different (a) current amplitudes (fixed SOC 60%) and (b) SOCs (fixed current amplitude C/4)

4.4 Battery state of health (SOH) diagnosis based on impedance data

In order to detect battery SOH based on impedance data, in frequency domain, five cells, of the same manufacturer, were tested. In this PhD thesis, the 20 Ah EIG cells [95] were under EIS test. EIG cell's specifications were depicted in Tables 2.1 and 2.2. One of the five cells under test is fresh and therefore considered as at the beginning of life. The other four cells have been cycled until they reached EOL for automotive application, and beyond. The history of the EOL cells was represented in Section 2, in the references [96][97] and in Figure 2.8. In this work, EIG cells was subjected under capacity test and results obtained were shown in Table 2.6. Considering that battery SOH is defined by the variation of battery capacity compared to its ideal condition, in this case, 20 Ah, the five cells, which will be under EIS test, has the following SOH:

- Cell #0: SOH=100%;
- Cell #3: SOH=80%;
- Cell #4: SOH=85%;
- Cell #5: SOH=60%;
- Cell #8: SOH=50%;

4.4.1 Battery impedance data set

The laboratory setup, shown in Figure 4.8, was used to perform EIS in the frequency band [4,1600] Hz, using the PRBS signal excitation in current at three different clock frequencies. For each PRBS test, 21 impedance measurements are extracted for each different clock frequency PRBS in the band specified in Table 4.2. To detect if there is a robust correlation between impedance information and SOH, battery impedance is estimated at various operating conditions. According to Table 4.3, EIS is executed at six different battery SOCs, and two different PRBS discharging current amplitudes, exactly at C-rate C/4, and C/20. To test the laboratory setup's repeatability, tests were repeated three times. Summing up, a large number of EIS experiments are performed for each cell, collecting a large number of impedance measurements. Room and battery surface temperature measurements acquired, during EIS tests, reported the following values:

- Room temperature: mean value of 22°C and a maximum and minimum value of 23.5°C and 20°C.
- Battery surface temperature: mean value of 22°C and a maximum and minimum value of 27°C and 20°C.

Results of the repeatability test had shown a very negligible variation of battery impedance estimation. Therefore, the mean impedance value will be shown in the next sections, when discussing of EIS data-set and data clustering. Finally, the data-set of each cell under test is composed of 756 impedance measurements in the defined frequency band. Concerning a single frequency investigated, the data-set is composed of 12 impedance measurements, at various SOCs, and rate

of discharge. Results obtained by ordinary coherence for EOL cells are shown in Figure 4.14. It's inferable that there is a slight increase in ordinary coherence with SOH decreasing. A complete view of the impedance points extracted for every cell is depicted in Figure 4.15. It's noticeable, as mentioned in the literature, the shift on the right of the impedance curve, which means an increase of the real part of battery impedance. It means an increment of the ohmic resistance, a fact in accordance with other literature observations [38]-[40]. Moreover, the increase of the semi-ellipses arcs with aging is noticeable in Figure 4.15. It means an increment of the charge transfer resistance [54] and the SEI resistance [55] with aging. Figure 4.15 denotes that the impedance curve of the new cell is an order of amplitude different respect to the EOL cells. Moreover, the new cell is completely disjointed with the EOL cell impedance curves. Therefore, using the EIS test, it is simple to distinguish a new cell from the EOL cell by performed measurements of impedance.

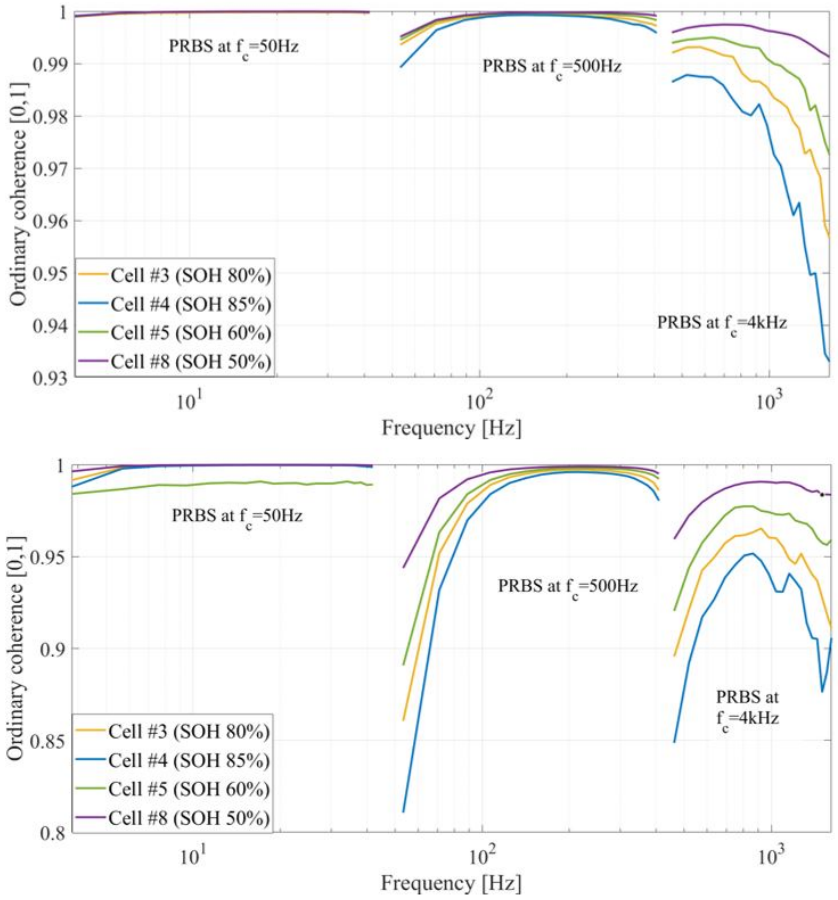

Figure 4.14: Mean ordinary coherence estimated during EIS test for cells at different SOHs by using the excitation PRBS with discharging current amplitude of (top) C/4 and (bottom) C/20

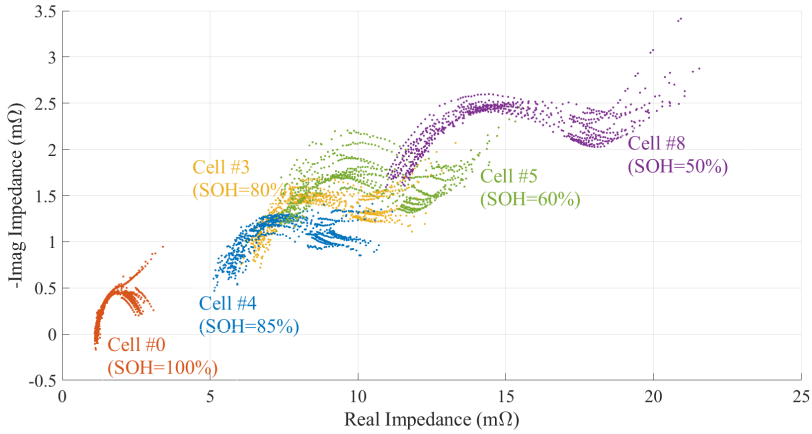

Figure 4.15: Battery impedance measurement data-set in the frequency band [4,1600] Hz, at various SOCs and PRBS discharging current amplitudes

4.4.2 Data clustering

Diagnosis and identification of the battery SOH are performed by using the EIS test. The question remains as to whether there are frequency points in which battery impedance is evaluated in a well-disjointed range of measurement, carried out at various operating conditions. In this work, the battery operating conditions included in the data-set are the variation of battery SOC, the amplitude of the discharge excitation current, and SOH. It's noticeable by Figure 4.15 that, in some frequency points, there is the possibility to cluster disjointed area of impedance measurements in the Nyquist diagram. An example is shown in Figure 4.16, considering the frequency measurement of 88.8 Hz. For every frequency, all the SOH area clusters are defined in the Nyquist diagram enclosing the 12 impedance measurements, by using rectangle geometry. Every rectangle's edge is defined by the maximum and the minimum value of the real and imaginary part of impedance measured, adding or subtracting an external factor:

$$\sigma(j\omega) = G_0[(\sigma_{real,dataset} + j\sigma_{imag,dataset}) + (\sigma_{real,instrument} + j\sigma_{imag,instrument})] \tag{4.11}$$

The value of the external factor corresponds to the sum of the following addends:

- The maximum variation (std) observed by the impedance measurements in all the single frequency clusters $(\sigma_{real,dataset} + j\sigma_{imag,dataset})$
- The uncertainty of the laboratory setup shown in Figure 4.8, relative to the diameter of the reference sample impedance $(\sigma_{real,instrument} + j\sigma_{imag,instrument})$.

The gain factor $G_0 = 0.5$ is considered in (4.11). Every rectangle's edge is obtained by experimental impedance data acquired during EIS tests. As previously mentioned, these tests are performed with a room temperature around [20,24]°C. Possible future development of impedance data collection is to perform EIS tests at higher and lower temperatures, observing if it is necessary to extend the SOH cluster's area.

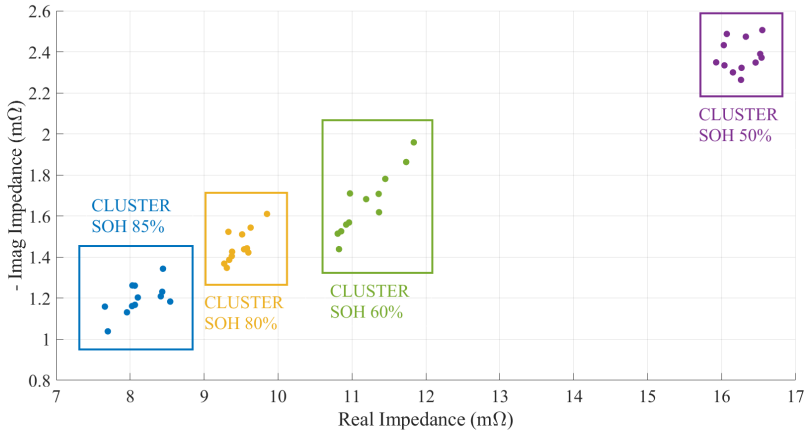

Figure 4.16: Battery impedance measurement data clustering at frequency 88.8 Hz

4.5 Results

4.5.1 Detection of SOH frequencies

In Section 4.3, it has been demonstrated that battery impedance can be fast measured. This action is realized by using the low-cost PRBS generator shown in Figure 4.5 and laboratory test setup shown in Figure 4.8. A large number of EIS experiments are performed on four EOL cells and described in Section 4.4. By clustering the impedance measurements in rectangular areas, we can detect the SOH frequencies. In these frequencies the SOH area clusters are disjointed, hence, they are candidates as reliable SOH indicators. As noticeable in Figure 4.16, the SOH clusters are disjointed if and only if there is no intersection between real-axis or between imaginary-axes of rectangles. The EIS measurements were carried out at different battery operating conditions, hence SOC variations [0,100]% and PRBS current C-rate amplitudes variations (C/4, C/20). The SOH clusters are defined for each frequency measured and cited in Table 4.3. The results obtained have demonstrated that it is not possible to highlight a SOH frequency in which the imaginary-axes of SOH clusters are disjointed and real-axes not. Indeed, as demonstrated by some research work in literature [38][40], the real impedance measurement is usually exploited to detect battery aging defined. The total number of SOH frequencies detected is 3 than 61 frequencies measured, in the band [4,1600] Hz. The SOH frequencies and the corresponding SOH clusters are shown in Table 4.4 and Figure 4.17. It's inferable that there is a noticeable variation of battery impedance measurement at different SOH in the three frequencies measured in the band [53.8,88.8] Hz, by using the 500 Hz PRBS. In this first result, all the EIS experiments were considered. In the next section, new SOH frequency bands are detected by filtering experimental data.

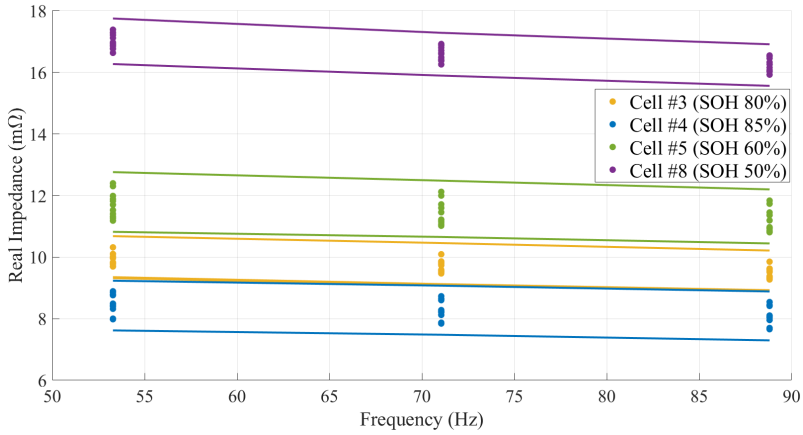

Figure 4.17: Detection of the SOH frequencies, illustrating the real impedance measurements for the different aged cells enclosed by disjointed area clusters.

4.5.2 Detection of SOH frequencies by filtering data

SOH cluster's areas change when filtering the EIS experiment. Hence, the number of SOH frequencies detected could be changed. The analysis of the clusters is carried out by considering 4 different types of EIS experiment filtering:

- **Case (a):** EIS experiments in the SOC interval [20÷80]% (impedance measurements at extreme of SOC values are less reliable).
- **Case (b):** EIS experiments with PRBS current of discharge amplitude of C/20 (response with low currents).
- **Case (c):**: EIS experiments with PRBS current of discharge amplitude of C/4 (response with high currents).
- **Case (d):** EIS experiments in the SOC interval [20÷80]%, with PRBS current of discharge amplitude of C/4 (best condition, high current, reliable SOC values).

The SOH frequencies are detected by filtering data, according to the four different case studies, and are shown in Table 4.4. The corresponding SOH clusters obtained in the SOH frequencies are shown in Figure 4.18. Results obtained in the case (a) confirm the detection of the same SOH frequency band observed in the previous analysis. Moreover, a new frequency band is detected: [4,24] Hz, measured by using the 50 Hz PRBS. These last results confirm that, as cited in the literature [40], and shown in Figure 4.13, impedance measurements drastically change their value when the EIS test is performed at the extreme of battery SOC. Hence, removing these data, impedance measurements are closes to them. Referring to the case (b), the SOH frequency band becomes larger ([54,125] Hz) than the case (a). Nevertheless, the SOH frequency band [4,24] Hz disappears due to the consideration of the impedance measurements at the extreme of SOC.
Generally, the impedances measured in the cases (a) and (b) are not very close to them. Indeed the power spectral of PRBS excitation signal with C/20 current amplitude is low. Considering this case, it's noticeable that voltage output observed is

more affected by noise, decreasing the coherence spectra results, as shown in Figure 4.14. Hence impedance measurements are less reliable. This deduction is confirmed by the case (c): increasing the power of the PRBS excitation signal until C/4, the impedance measurements in the SOH frequencies, are very close to them, as shown in Figure 4.18. It's noticeable that all frequencies measured by using 50 Hz and 500 Hz PRBS become a good indicator of battery SOH. Moreover, the new SOH frequency band [461,922] Hz extracted by the 4 kHz PRBS is detected. Finally, results obtained in the case (d) demonstrate that all the frequency measured become as SOH frequencies. This last case, considering only the impedance measurements at the SOC in [20÷80]% and high current excitation, could be an acceptable constraint for EIS measurements in real-time applications. Usually, battery packs are used with a reduced DOD (not 100%), prolonging their lifetime. Moreover, all the EIS tests consumed less than 1% of battery SOC. As it is well observable from Figure 8-10, the clustering of the impedance measurements allows us to determine the SOH directly. The experimental EIS tests allowed to define each SOH cluster region in an appropriate range of impedance measurement (real or imaginary part). For every single SOH frequency detected, the SOH clusters are disjointed between them. Hence, it's possible to assess SOH with low computational efforts by performing the fast EIS test in one of the SOH frequency bands detected.

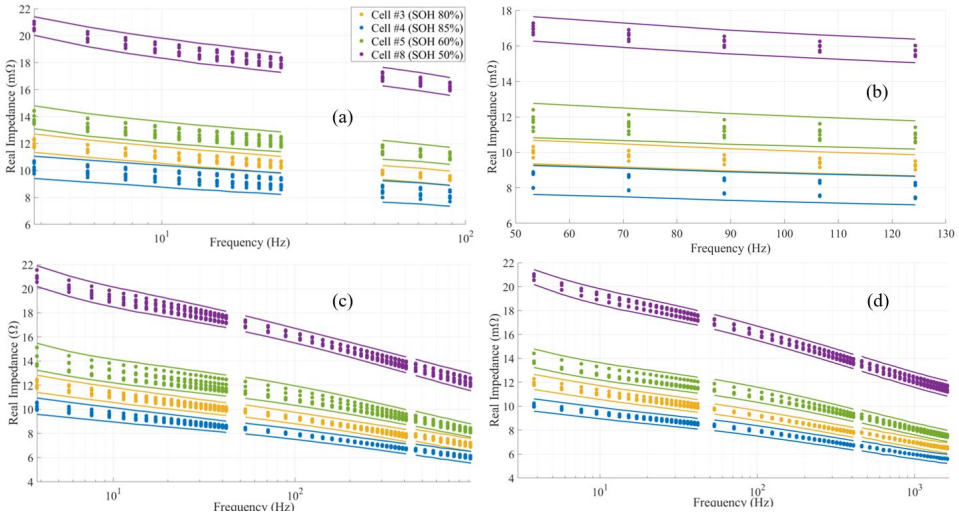

Figure 4.18: Detection of the SOH frequencies, filtering data: (a) SOC in [20÷80]%; (b) fixed C-rate C/20; (c) fixed C-rate C/4; (d) SOC in [20÷80]% and fixed C-rate C/4

Impedance data-set	**50 Hz PRBS**		**500 Hz PRBS**		**4 kHz PRBS**	
	Frequency band (Hz)	SOH frequency band (Hz)	Frequency band (Hz)	SOH frequency band (Hz)	Frequency band (Hz)	SOH frequency band (Hz)
SOC [0,100]% with PRBS amplitude of C/4,C/20 (36 impedances)	[4,40]	/	[53,400]	[53,89]	[450,1600]	/
SOC [20,80]% with PRBS amplitude of C/4,C/20 (24 impedances)	[4,40]	[4,24]	[53,400]	[53,89]	[450,1600]	/
SOC [0,100]% with PRBS amplitude of C/20 (18 impedances)	[4,40]	/	[53,400]	[53,125]	[450,1600]	/
SOC [0,100]% with PRBS amplitude of C/4 (18 impedances)	[4,40]	[4,40]	[53,400]	[53,400]	[450,1600]	/ [450,922]
SOC [0,100]% with PRBS amplitude of C/4,C/20 (12 impedances)	[4,40]	[4,40]	[53,400]	[53,400]	[450,1600]	[450,1600]

Table 4.4: Detection of the SOH frequencies considering different battery impedance data set.

Chapter 5

Conclusion and Outlook

5.1 Conclusion

The object of this PhD work was the evaluation of all those techniques that can contribute to a more efficient and sustainable industrial use of batteries. The issue of this research involves several fields. First of all the modeling and the analysis of the electrical short and long term time behavior of a lithium battery including aging phenomena. The second aspect is the individuation and the development of new methodologies to estimate battery state of charge (SOC) in a short term time and state of health (SOH) over longer time horizons.
In this research I started from the definition of electrical battery models updated to the latest state of the art: firstly by introducing hysteresis models to represent battery voltage behaviors (Chapter 2 and 3); secondly by introducing electrical models, in the frequency domain, made up by fractional-order circuits (Section 2.4); finally, by defining a performance model of automotive EOL battery, ready for a second use in less demanding applications, such as stationary applications (Chapter 2). In literature, there is a lack of reliable and accurate second life battery model. The second life battery model was build in Simulink and validated by experimental tests. This performance model will be useful to the automotive companies and research departments to assess the applicability of second-life batteries from BEV into stationary applications.
Regarding the second topic of this PhD thesis, the development of new methodologies to predict battery SOC and SOH, analysis, design, and results obtained are shown in Chapter 3 and 4. Concerning the first one, this PhD work has compared different types of algorithms for SOC estimation, based on Kalman filtering (KF) techniques, different definitions of modeling, and parametrizations of the battery. The robustness of proposed algorithms is investigated exhaustively by introducing additive measurement errors or troubles related to implementation, such as reduced sampling frequency, and uncertain or wrong initialization of estimated SOC. In this way, it's possible to give a complete overview of the consequences in terms of performances and robustness of different estimation techniques. Between the proposed algorithms aligned with the most recent state of art, the SOC estimator based on KF with recursive least square with forgetting factor (RLSFF) and the addition of hysteresis model represents a novel methodology. The hysteresis property included in the voltage model helps the battery model to find a robust voltage

estimate, fundamental to obtain an accurate SOC estimate. By experimental tests, it's noticeable that the introduction of the hysteresis property inside the battery model reduces the KF time convergence. Also considering the response to noise, results on SOC estimation have shown that the addition of the hysteresis model improves KF performance. Finally, the RLSFF has demonstrated reduced SOC estimation time convergence and much more flexibility. Indeed RLSFF technique requires fewer calibration data, typically not available from the manufacturer and obtainable only through ad hoc experimental tests. Besides, it also requires a reduction of memory than offline methods.
The last contribution of this PhD thesis was the development of a battery SOH diagnosis addressed for embedded systems and industrial applications. It was demonstrated that the EIS technique is a powerful method to investigate the SOH of lithium batteries. The proposed methodology aims at detecting battery SOH using fast impedance measurements by EIS tests. The chosen excitation signal plays a key role in defining the complexity and consequently the industrial applicability of the proposed EIS test. The PBRS excitation signal has proven to be a good solution for possible industrial applications, thanks to its simplicity in hardware and software implementation. Experimental tests have verified that it's possible to generate the PRBS signal with relatively cheap hardware to perform accurate impedance measurements of the battery. In literature, EIS tests are typically performed with more expensive and specialized facilities. Finally, EIS tests are performed on EOL automotive cells. Results confirm the existence of specific frequency bands candidate as a reliable and robust indicator of the SOH, depending on several operating conditions of the battery. Clustering impedance measurements in SOH regions allowed to detect these frequencies and correlate SOH with cell impedance with low computational efforts.
All the approaches proposed and the results obtained have been specifically evaluated in terms of real-time applicability on low-cost hardware in ways that make a profitable industrial implementation possible. In particular, this work has been recognized as an important contribution to the OBELICS project that financed my work.

5.2 Outlook

The second-life battery model presented in Chapter 2 could be used to investigate their applicability to real industrial applications. In particular, it's important to understand if second-life batteries give in output a final credit value in terms of economic and environmental impact with respect to the use of a beginning of life lithium or lead-acid battery. Preliminary work is reported in [98] and in [102]. Regarding the proposed SOH diagnostic method, one of the possible future development is the implementation of impedance data post-processing in one of the CPU cores of the TI board. Moreover, this methodology could be embedded in the state-of-art battery charging systems. The idea consists of performing EIS tests during the CC charging on the battery. The EIS test duration time would be only 1 minute. Charging excitation signal is the 500 Hz PRBS of current level [I_{const},$I_{const} - I_{PRBS}$]. In this way, during every battery charging event, there is the possibility to monitor battery SOH without energy consumption and the addition of cheap hardware components. Preliminary work is reported in [122], where the EIS test, characterized by PRBS excitation technique, is implemented on-board of a wireless charging system for BEVs.

Bibliography

[1] European Commission. White Paper: European Transport Policy for 2010: Time to Decide; Technical Report; European Commission: Luxemburg, 2001.

[2] Aneke, M., & Wang, M. (2016). Energy storage technologies and real life applications–A state of the art review. Applied Energy, 179, 350-377.

[3] Wolfram, P., & Lutsey, N. (2016). Electric vehicles: Literature review of technology costs and carbon emissions. The International Council on Clean Transportation: Washington, DC, USA, 1-23.

[4] Lebedeva, N., Di Persio, F., & Boon-Brett, L. (2016). Lithium ion battery value chain and related opportunities for Europe. European Commission, Petten.

[5] Berckmans, G., Messagie, M., Smekens, J., Omar, N., Vanhaverbeke, L., & Van Mierlo, J. (2017). Cost projection of state of the art lithium-ion batteries for electric vehicles up to 2030. Energies, 10(9), 1314.

[6] Blomgren, G. E. (2016). The development and future of lithium ion batteries. Journal of The Electrochemical Society, 164(1), A5019.

[7] Luo, X., Wang, J., Dooner, M., & Clarke, J. (2015). Overview of current development in electrical energy storage technologies and the application potential in power system operation. Applied energy, 137, 511-536.

[8] Crabtree, G., Kocs, E., & Trahey, L. (2015). The energy-storage frontier: Lithium-ion batteries and beyond. Mrs Bulletin, 40(12), 1067-1078.

[9] Omar, N., Monem, M. A., Firouz, Y., Salminen, J., Smekens, J., Hegazy, O., ... & Van Mierlo, J. (2014). Lithium iron phosphate based battery–assessment of the aging parameters and development of cycle life model. Applied Energy, 113, 1575-1585.

[10] Neubauer, J., & Pesaran, A. (2011). The ability of battery second use strategies to impact plug-in electric vehicle prices and serve utility energy storage applications. Journal of Power Sources, 196(23), 10351-10358.

[11] Martinez-Laserna, E., Gandiaga, I., Sarasketa-Zabala, E., Badeda, J., Stroe, D. I., Swierczynski, M., & Goikoetxea, A. (2018). Battery second life: Hype, hope or reality? A critical review of the state of the art. Renewable and Sustainable Energy Reviews, 93, 701-718.

[12] Figgener, J., Stenzel, P., Kairies, K. P., Linßen, J., Haberschusz, D., Wessels, O., ... & Sauer, D. U. (2020). The development of stationary battery storage systems in Germany–A market review. Journal of Energy Storage, 29, 1011534.

[13] Bobba, S., Podias, A., Di Persio, F., Messagie, M., Tecchio, P., Cusenza, M. A., ... & Pfrang, A. (2018). Sustainability Assessment of Second Life Application of Automotive Batteries (SASLAB). JRC Exploratory Research (2016-2017 Final report).

[14] Xu, G. L., Wang, Q., Fang, J. C., Xu, Y. F., Li, J. T., Huang, L., & Sun, S. G. (2014). Tuning the structure and property of nanostructured cathode materials of lithium ion and lithium sulfur batteries. Journal of Materials Chemistry A, 2(47), 19941-19962.

[15] Battery University website. [Online]. Available: https://batteryuniversity.com/

[16] Budde-Meiwes, H., Drillkens, J., Lunz, B., Muennix, J., Rothgang, S., Kowal, J., & Sauer, D. U. (2013). A review of current automotive battery technology and future prospects. Proceedings of the Institution of Mechanical Engineers, Part D: Journal of Automobile Engineering, 227(5), 761-776.

[17] Obelics, Deliverable D7.2 "Evaluation of international standards for lithium-ion batteries", (2018), Available: https://obelics.eu/downloads/.

[18] Obelics, Deliverable D7.5 "Optimization of OBELICS test procedures", (2018), Available: https://obelics.eu/downloads/.

[19] Ruiz, V., Pfrang, A., Kriston, A., Omar, N., Van den Bossche, P., & Boon-Brett, L. (2018). A review of international abuse testing standards and regulations for lithium ion batteries in electric and hybrid electric vehicles. Renewable and Sustainable Energy Reviews, 81, 1427-1452.

[20] Li, K., Wei, F., Tseng, K. J., & Soong, B. H. (2017). A practical lithium-ion battery model for state of energy and voltage responses prediction incorporating temperature and ageing effects. IEEE Transactions on Industrial Electronics, 65(8), 6696-6708.

[21] Ceraolo, M., Giglioli, R., Lutzemberger, G., Langroudi, M. M., Poli, D., Andrenacci, N., & Pasquali, M. (2018, June). Experimental analysis of NMC lithium cells aging for second life applications. In 2018 IEEE International Conference on Environment and Electrical Engineering and 2018 IEEE Industrial and Commercial Power Systems Europe (EEEIC/I&CPS Europe) (pp. 1-6). IEEE.

[22] Waag, W., Fleischer, C., & Sauer, D. U. (2014). Critical review of the methods for monitoring of lithium-ion batteries in electric and hybrid vehicles. Journal of Power Sources, 258, 321-339.

[23] Berecibar, M., Gandiaga, I., Villarreal, I., Omar, N., Van Mierlo, J., & Van den Bossche, P. (2016). Critical review of state of health estimation methods of Li-ion batteries for real applications. Renewable and Sustainable Energy Reviews, 56, 572-587.

[24] Xiong, R., Cao, J., Yu, Q., He, H., & Sun, F. (2017). Critical review on the battery state of charge estimation methods for electric vehicles. Ieee Access, 6, 1832-1843.

[25] Groenewald, J., Grandjean, T., & Marco, J. (2017). Accelerated energy capacity measurement of lithium-ion cells to support future circular economy strategies for electric vehicles. Renewable and Sustainable Energy Reviews, 69, 98-111.

[26] Brand, M., Gläser, S., Geder, J., Menacher, S., Obpacher, S., Jossen, A., & Quinger, D. (2013). Electrical safety of commercial Li-ion cells based on NMC and NCA technology compared to LFP technology. World Electric Vehicle Journal, 6(3), 572-580.

[27] Huria, T., Ludovici, G., & Lutzemberger, G. (2014). State of charge estimation of high power lithium iron phosphate cells. Journal of Power Sources, 249, 92-102.

[28] Ceraolo, M., Lutzemberger, G., Poli, D., & Scarpelli, C. (2020). Luenberger-based State-Of-Charge evaluation and experimental validation with lithium cells. Journal of Energy Storage, 30, 101534.

[29] Kim, I. S. (2006). The novel state of charge estimation method for lithium battery using sliding mode observer. Journal of Power Sources, 163(1), 584-590.

[30] He, H., Xiong, R., Zhang, X., Sun, F., & Fan, J. (2011). State-of-charge estimation of the lithium-ion battery using an adaptive extended Kalman filter based on an improved Thevenin model. IEEE Transactions on Vehicular Technology, 60(4), 1461-1469.

[31] Sun, F., Hu, X., Zou, Y., & Li, S. (2011). Adaptive unscented Kalman filtering for state of charge estimation of a lithium-ion battery for electric vehicles. Energy, 36(5), 3531-3540.

[32] Ljung, L. System Identification, Theory for the User. Prentice Hall, Englewood Cliffs, N. J., 1987.

[33] Zhang, C., Li, K., Deng, J., & Song, S. (2016). Improved Realtime State-of-Charge Estimation of LiFePO4 Battery Based on a Novel Thermoelectric Model. IEEE Transactions on Industrial Electronics, 64(1), 654-663.

[34] Zhang, X., Wu, J., & Kang, G. (2016, August). SOC estimation of Lithium battery by UKF algorithm based on dynamic parameter model. In 2016 13th International Conference on Ubiquitous Robots and Ambient Intelligence (URAI) (pp. 945-950). IEEE.

[35] Hasan, A., Skriver, M., & Johansen, T. A. (2018). eXogenous Kalman Filter for Lithium-Ion Batteries State-of-Charge Estimation in Electric Vehicles. arXiv preprint arXiv:1810.09014.

[36] De Sutter, L., Nikolian, A., Timmermans, J. M., Omar, N., & Van Mierlo, J. (2018). Online Multi Chemistry SoC Estimation Technique Using Data Driven Battery Model Parameter Estimation. World Electric Vehicle Journal, 9(2), 16.

[37] Locorotondo, E., Pugi, L., Berzi, L., Pierini, M., & Lutzemberger, G. (2018, June). Online identification of Thevenin equivalent circuit model parameters and estimation State of Charge of Lithium-Ion batteries. In 2018 IEEE International Conference on Environment and Electrical Engineering and 2018 IEEE Industrial and Commercial Power Systems Europe (EEEIC/I&CPS Europe) (pp. 1-6). IEEE.

[38] Tröltzsch, U., Kanoun, O., & Tränkler, H. R. (2006). Characterizing aging effects of lithium ion batteries by impedance spectroscopy. Electrochimica acta, 51(8-9), 1664-1672.

[39] Raijmakers, L. H. J., Danilov, D. L., Van Lammeren, J. P. M., Lammers, M. J. G., & Notten, P. H. L. (2014). Sensorless battery temperature measurements based on electrochemical impedance spectroscopy. Journal of Power Sources, 247, 539-544.

[40] Waag, W., Käbitz, S., & Sauer, D. U. (2013). Experimental investigation of the lithium-ion battery impedance characteristic at various conditions and aging states and its influence on the application. Applied energy, 102, 885-897.

[41] Nguyen, T. T., Tran, V. L., & Choi, W. (2014, June). Development of the intelligent charger with battery State-Of-Health estimation using online impedance spectroscopy. In 2014 IEEE 23rd International Symposium on Industrial Electronics (ISIE) (pp. 454-458). IEEE.

[42] Stroe, D. I., Knap, V., Swierczynski, M., & Schaltz, E. (2018). Electrochemical impedance spectroscopy-based electric circuit modeling of lithium–sulfur batteries during a discharging state. IEEE Transactions on Industry Applications, 55(1), 631-637.

[43] Yang, H., Yoshio, M., Isono, K., & Kuramoto, R. (2002). Improvement of commercial activated carbon and its application in electric double layer capacitors. Electrochemical and Solid State Letters, 5(6), A141.

[44] Escalante-García, I. L., Wainright, J. S., Thompson, L. T., & Savinell, R. F. (2014). Performance of a non-aqueous vanadium acetylacetonate prototype redox flow battery: examination of separators and capacity decay. Journal of The Electrochemical Society, 162(3), A363.

[45] Darowicki, K., Janicka, E., Mielniczek, M., Zielinski, A., Gawel, L., Mitzel, J., & Hunger, J. (2019). The influence of dynamic load changes on temporary impedance in hydrogen fuel cells, selection and validation of the electrical equivalent circuit. Applied Energy, 251, 113396.

[46] F. Berthier, J.P Diard, R. Michel, "Distinguishability of equivalent circuits containing CPEs: Part I. Theoretical part." Journal of Electroanalytical Chemistry, 510(1-2), 1-11, 2001.

[47] Andre, D., Meiler, M., Steiner, K., Wimmer, C., Soczka-Guth, T., & Sauer, D. U. (2011). Characterization of high-power lithium-ion batteries by electrochemical impedance spectroscopy. I. Experimental investigation. Journal of Power Sources, 196(12), 5334-5341.

[48] Andre, D., Meiler, M., Steiner, K., Walz, H., Soczka-Guth, T., & Sauer, D. U. (2011). Characterization of high-power lithium-ion batteries by electrochemical impedance spectroscopy. II: Modelling. Journal of Power Sources, 196(12), 5349-5356.

[49] Stroe, D. I., Swierczynski, M., Stan, A. I., Knap, V., Teodorescu, R., & Andreasen, S. J. (2014, September). Diagnosis of lithium-ion batteries state-of-health based on electrochemical impedance spectroscopy technique. In 2014 IEEE Energy Conversion Congress and Exposition (ECCE) (pp. 4576-4582). IEEE

[50] Galeotti, M., Cinà, L., Giammanco, C., Cordiner, S., & Di Carlo, A. (2015). Performance analysis and SOH (state of health) evaluation of lithium polymer batteries through electrochemical impedance spectroscopy. Energy, 89, 678-686.

[51] Lyu, C., Zhang, T., Luo, W., Wei, G., Ma, B., & Wang, L. (2019, June). SOH Estimation of Lithium-ion Batteries Based on Fast Time Domain Impedance Spectroscopy. In 2019 14th IEEE Conference on Industrial Electronics and Applications (ICIEA) (pp. 2142-2147). IEEE.

[52] De Sutter, L., Firouz, Y., De Hoog, J., Omar, N., & Van Mierlo, J. (2019). Battery aging assessment and parametric study of lithium-ion batteries by means of a fractional differential model. Electrochimica Acta, 305, 24-36.

[53] Olofsson, Y., Groot, J., Katrašnik, T., & Tavčar, G. (2014, December). Impedance spectroscopy characterisation of automotive NMC/graphite Li-ion cells aged with realistic PHEV load profile. In 2014 IEEE International Electric Vehicle Conference (IEVC) (pp. 1-6). IEEE.

[54] Wang, X., Wei, X., & Dai, H. (2019). Estimation of state of health of lithium-ion batteries based on charge transfer resistance considering different temperature and state of charge. Journal of Energy Storage, 21, 618-631.

[55] Xiong, R., Tian, J., Mu, H., & Wang, C. (2017). A systematic model-based degradation behavior recognition and health monitoring method for lithium-ion batteries. Applied Energy, 207, 372-383.

[56] Yang, D.; Wang, Y.; Pan, R.; Chen, R.; Chen, Z. A Neural Network Based State-of-Health Estimation of Lithium-ion Battery in Electric Vehicles. Energy Procedia 2017, 105, 2059–2064.

[57] Klass, V., Behm, M., & Lindbergh, G. (2014). A support vector machine-based state-of-health estimation method for lithium-ion batteries under electric vehicle operation. Journal of Power Sources, 270, 262-272.

[58] Khaleghi, S., Firouz, Y., Van Mierlo, J., & Van den Bossche, P. (2019). Developing a real-time data-driven battery health diagnosis method, using time and frequency domain condition indicators. Applied Energy, 255, 113813.

[59] Eddahech, A., Briat, O., & Vinassa, J. M. (2015). Performance comparison of four lithium–ion battery technologies under calendar aging. Energy, 84, 542-550.

[60] Love, C. T., Virji, M. B., Rocheleau, R. E., & Swider-Lyons, K. E. (2014). State-of-health monitoring of 18650 4S packs with a single-point impedance diagnostic. Journal of Power Sources, 266, 512-519.

[61] Christophersen, J. P., Morrison, J., Morrison, W., & Motloch, C. (2012). Rapid impedance spectrum measurements for state-of-health assessment of energy storage devices. SAE International Journal of Passenger Cars-Electronic and Electrical Systems, 5(2012-01-0657), 246-256.

[62] Haußmann, P., & Melbert, J. (2017). Optimized mixed-domain signal synthesis for broadband impedance spectroscopy measurements on lithium ion cells for automotive applications. Journal of Sensors and Sensor Systems, 6(1), 65.

[63] Relan, R., Firouz, Y., Timmermans, J. M., & Schoukens, J. (2016). Data-driven nonlinear identification of Li-ion battery based on a frequency domain nonparametric analysis. IEEE Transactions on Control Systems Technology, 25(5), 1825-1832.

[64] Sihvo, J., Stroe, D. I., Messo, T., & Roinila, T. (2019). Fast Approach for Battery Impedance Identification Using Pseudo-Random Sequence Signals. IEEE Transactions on Power Electronics, 35(3), 2548-2557.

[65] Locorotondo, E., Scavuzzo, S., Pugi, L., Ferraris, A., Berzi, L., Airale, A., ... & Carello, M. (2019, June). Electrochemical Impedance Spectroscopy of Li-Ion battery on-board the Electric Vehicles based on Fast nonparametric identification method. In 2019 IEEE International Conference on Environment and Electrical Engineering and 2019 IEEE Industrial and Commercial Power Systems Europe (EEEIC/I&CPS Europe) (pp. 1-6). IEEE.

[66] Al Nazer, R., Cattin, V., Granjon, P., Montaru, M., & Ranieri, M. (2013). Broadband identification of battery electrical impedance for HEVs. IEEE transactions on vehicular technology, 62(7), 2896-2905.

[67] Piret, H., Granjon, P., Guillet, N., & Cattin, V. (2016). Tracking of electrochemical impedance of batteries. Journal of Power Sources, 312, 60-69.

[68] Howey, D. A., Mitcheson, P. D., Yufit, V., Offer, G. J., & Brandon, N. P. (2013). Online measurement of battery impedance using motor controller excitation. IEEE transactions on vehicular technology, 63(6), 2557-2566.

[69] Locorotondo, E., Lutzemberger, G., & Pugi, L. (2020). State-of-charge estimation based on model-adaptive Kalman filters. Proceedings of the Institution of Mechanical Engineers, Part I: Journal of Systems and Control Engineering, 0959651820965406.

[70] Locorotondo, E., Cultrera, V., Pugi, L., Berzi, L., Pasquali, M., Andrenacci, N., ... & Pierini, M. (2020, June). Electrical lithium battery performance model for second life applications. In 2020 IEEE International Conference on Environment and Electrical Engineering and 2020 IEEE Industrial and Commercial Power Systems Europe (EEEIC/I&CPS Europe) (pp. 1-6). IEEE.

[71] Locorotondc, E., Pugi, L., Berzi, L., Pierini, M., Scavuzzc, S., Ferraris, A., ... & Carello, M. (2019, September). Modeling and simulation of Constant Phase Element for battery Electrochemical Impedance Spectroscopy. In 2019 IEEE 5th International forum on Research and Technology for Society and Industry (RTSI) (pp. 225-230). IEEE.

[72] Serni, T., Locorotondo, E., Pugi, L., Berzi, L., Pierini, M., & Cultrera, V. (2020, June). A Low Cost Programmable Hardware for Online Spectroscopy of Lithium Batteries. In 2020 IEEE 20th Mediterranean Electrotechnical Conference (MELECON) (pp. 57-62). IEEE.

[73] Locorotondo, E., Cultrera, V., Pugi, L., Berzi, L., Pasquali, M., Andrenacci, N., ... & Pierini, M. (2020, June). Impedance spectroscopy characterization of lithium batteries with different ages in second life application. In 2020 IEEE International Conference on Environment and Electrical Engineering and 2020 IEEE Industrial and Commercial Power Systems Europe (EEEIC/I&CPS Europe) (pp. 1-6). IEEE.

[74] Locorotondo, E., Cultrera, V., Pugi, L., Berzi, L., Pierini, M., & Lutzemberger, G. (2021). Development of a battery real-time state of health diagnosis based on fast impedance measurements. Journal of Energy Storage, 38, 102566.

[75] Jongerden, M. R., & Haverkort, B. R. (2009). Which battery model to use?. IET software, 3(6), 445-457.

[76] Wang, Y., Tian, J., Sun, Z., Wang, L., Xu, R., Li, M., & Chen, Z. (2020). A comprehensive review of battery modeling and state estimation approaches for advanced battery management systems. Renewable and Sustainable Energy Reviews, 131, 110015.

[77] Huria, T., Ceraolo, M., Gazzarri, J., & Jackey, R. (2012, March). High fidelity electrical model with thermal dependence for characterization and simulation of high power lithium battery cells. In 2012 IEEE International Electric Vehicle Conference (pp. 1-8). IEEE.

[78] Firouz, Y., Goutam, S., Soult, M. C., Mohammadi, A., Van Mierlo, J., & Van den Bossche, P. (2020). Block-oriented system identification for nonlinear modeling of all-solid-state Li-ion battery technology. Journal of Energy Storage, 28, 101184.

[79] Wang Y, Yang D, Zhang X, et al. Probability based remaining capacity estimation using data-driven and neural network model. J Power Sources 2016;315: 199–208.

[80] Wei J, Dong G, Chen Z. Remaining useful life prediction and state of health diagnosis for lithium-ion batteries using particle filter and support vector regression. IEEE Trans Ind Electron 2017;65(7):5634–43.

[81] Doyle, M., Fuller, T. F., & Newman, J. (1993). Modeling of galvanostatic charge and discharge of the lithium/polymer/insertion cell. Journal of the Electrochemical society, 140(6), 1526.

[82] Ahmed, R., El Sayed, M., Arasaratnam, I., Tjong, J., & Habibi, S. (2014). Reduced-order electrochemical model parameters identification and soc estimation for healthy and aged li-ion batteries part i: Parameterization model development for healthy batteries. IEEE journal of emerging and selected topics in power electronics, 2(3), 659-677.

[83] Song, X., Lu, Y., Wang, F., Zhao, X., & Chen, H. (2020). A coupled electro-chemo-mechanical model for all-solid-state thin film Li-ion batteries: The effects of bending on battery performances. Journal of Power Sources, 452, 227803.

[84] Mele, I., Pačnik, I., Zelič, K., Moškon, J., & Katrašnik, T. (2020). Advanced Porous Electrode Modelling Framework Based on More Consistent Virtual Representation of the Electrode Topology. Journal of The Electrochemical Society, 167(6), 060531.

[85] Cittanti, D., Ferraris, A., Airale, A., Fiorot, S., Scavuzzo, S., & Carello, M. (2017, June). Modeling Li-ion batteries for automotive application: A trade-off between accuracy and complexity. In 2017 International Conference of Electrical and Electronic Technologies for Automotive (pp. 1-8). IEEE.

[86] Baronti, F., Fantechi, G., Leonardi, E., Roncella, R., & Saletti, R. (2010, November). Enhanced model for Lithium-Polymer cells including temperature effects. In IECON 2010-36th Annual Conference on IEEE Industrial Electronics Society (pp. 2329-2333). IEEE.

[87] Saw, L. H., Ye, Y., & Tay, A. A. O. (2014). Electro-thermal characterization of Lithium Iron Phosphate cell with equivalent circuit modeling. Energy conversion and management, 87, 367-377.

[88] Hariharan, K. S., & Kumar, V. S. (2013). A nonlinear equivalent circuit model for lithium ion cells. Journal of power sources, 222, 210-217.

[89] Ceraolo, M., Lutzemberger, G., Poli, D., & Scarpelli, C. (2019, June). Model parameters evaluation for NMC cells. In 2019 IEEE International Conference on Environment and Electrical Engineering and 2019 IEEE Industrial and Commercial Power Systems Europe (EEEIC/I&CPS Europe) (pp. 1-6). IEEE.

[90] Zhang, C., Allafi, W., Dinh, Q., Ascencio, P., & Marco, J. (2018). Online estimation of battery equivalent circuit model parameters and state of charge using decoupled least squares technique. Energy, 142, 678-688.

[91] Liu, K., Li, K., Yang, Z., Zhang, C., & Deng, J. (2017). An advanced Lithium-ion battery optimal charging strategy based on a coupled thermoelectric model. Electrochimica Acta, 225, 330-344.

[92] Karnopp, D. C., Margolis, D. L., & Rosenberg, R. C. (2012). System dynamics: modeling, simulation, and control of mechatronic systems. John Wiley & Sons.

[93] Lin, C., Tang, A., & Wang, W. (2015). A review of SOH estimation methods in Lithium-ion batteries for electric vehicle applications. Energy Procedia, 75, 1920-1925.

[94] Patel, D. D., Tredeau, F. P., & Salameh, Z. M. (2010, September). Temperature effects on fast charging large format prismatic lithium iron phosphate cells. In 2010 IEEE Vehicle Power and Propulsion Conference (pp. 1-4). IEEE.

[95] EIG battery official site, www.eigbattery.com

[96] Andrenacci, N., & Sglavo, V. (2017). Stato dell'arte dei modelli di invecchiamento per le celle litio-ione. Applicazione al caso di studio delle celle NMC invecchiate in ENEA. Report RDS/PAR2016/

[97] Pasquali, M., Vellucci, F. (2018). Validazione sperimentale delle procedure per la valutazione dello stato di salute delle batterie. Report RdS/PAR2018/098/

[98] Obelics, Deliverable D7.9 "Analysis of second life battery market, performances/aging and applications", (2020), under review.

[99] Renga, D., Hassan, H. A. H., Meo, M., & Nuaymi, L. (2018). Energy management and base station on/off switching in green mobile networks for offering ancillary services. IEEE Transactions on Green Communications and Networking, 2(3), 868-880.

[100] Krauss, R., Brante, G., Rayel, O. K., Souza, R. D., Onireti, O., & Imran, M. A. (2018). Energy Efficiency of Multiple Antenna Cellular Networks Considering a Realistic Power Consumption Model. IEEE Transactions on Green Communications and Networking, 3(1), 1-10.

[101] "Home - Terna spa". https://www.terna.it/it (consulted in April 15, 2020).

[102] Berzi, L., Cultrera, V., Delogu, M., Dolfi, M., Locorotondo, E., Del Pero, F., ... & Tanturli, A. (2020, June). A model for system integration of second life battery, renewable energy generation and mobile network station. In 2020 IEEE International Conference on Environment and Electrical Engineering and 2020 IEEE Industrial and Commercial Power Systems Europe (EEEIC/I&CPS Europe) (pp. 1-6). IEEE.

[103] Zou, C., Zhang, L., Hu, X., Wang, Z., Wik, T., & Pecht, M. (2018). A review of fractional-order techniques applied to lithium-ion batteries, lead-acid batteries, and supercapacitors. Journal of Power Sources, 390, 286-296.

[104] Cheng, C. S., Chung, H. S. H., & Lau, R. W. H. (2017, March). Time-domain modeling of constant phase element for simulation of lithium batteries under arbitrary charging and discharging current profiles. In 2017 IEEE Applied Power Electronics Conference and Exposition (APEC) (pp. 985-992). IEEE.

[105] Cheng, C. S., Chung, H. S. H., Lau, R. W. H., & Hong, K. Y. W. (2018). Time-Domain Modeling of Constant Phase Elements for Simulation of Lithium Battery Behavior. IEEE Transactions on Power Electronics, 34(8), 7573-7587.

[106] Groot, J. (2012). State-of-health estimation of li-ion batteries: Cycle life test methods.

[107] Al-Nazer, R., Cattin, V., Granjon, P., & Montaru, M. (2012, June). A new optimization algorithm for a Li-Ion battery equivalent electrical circuit identification.

[108] Randles, J. E. B. (1947). Kinetics of rapid electrode reactions. Discussions of the faraday society, 1, 11-19.

[109] Schoenleber, M., & Ivers-Tiffée, E. (2015). Approximability of impedance spectra by RC elements and implications for impedance analysis. Electrochemistry Communications, 58, 15-19.

[110] Li, K., Wei, F., Tseng, K. J., & Soong, B. H. (2017). A practical lithium-ion battery model for state of energy and voltage responses prediction incorporating temperature and ageing effects. IEEE Transactions on Industrial Electronics, 65(8), 6696-6708.

[111] Julier, S. J., & Uhlmann, J. K. (2004). Unscented filtering and nonlinear estimation. Proceedings of the IEEE, 92(3), 401-422.

[112] Boukamp, B. A. (1995). A linear Kronig-Kramers transform test for immittance data validation. Journal of the electrochemical society, 142(6), 1885-1894.

[113] Schönleber, M., Klotz, D., & Ivers-Tiffée, E. (2014). A method for improving the robustness of linear Kramers-Kronig validity tests. Electrochimica Acta, 131, 20-27.

[114] Pintelon, R., & Schoukens, J. (2012). System identification: a frequency domain approach. John Wiley & Sons.

[115] J. Silva and N. Maia, "Modal Analysis and Testing", Applied Science, Vol. 363, 1999.

[116] Welch, P. (1967). The use of fast Fourier transform for the estimation of power spectra: a method based on time averaging over short, modified periodograms. IEEE Transactions on audio and electroacoustics, 15(2), 70-73.

[117] Al Nazer, R., Cattin, V., Granjon, P., Montaru, M., Ranieri, M., & Heiries, V. (2013). Classical EIS and square pattern signals comparison based on a well-known reference impedance. World Electric Vehicle Journal, 6(3), 800-806.

[118] Texas Instrument LAUNCHXL-F28379D Overview User's Guide SPRUI77C–August 2016–Revised March 2019 availabel on line at TI official site http://www.ti.com/lit/ug/sprui77c/sprui77c.pdf

[119] Pugi, L., Grasso, E., & Fabbri, S. (2018, June). Enhanced Back EMF Sensorless Control for Permanent Magnet Synchronous Motors. In 2018 IEEE International Conference on Environment and Electrical Engineering and 2018 IEEE Industrial and Commercial Power Systems Europe (EEEIC/I&CPS Europe) (pp. 1-6). IEEE.

[120] Pugi, L., Galardi, E., Carcasci, C., & Lucchesi, N. (2017). Hardware in-the-loop testing of bypass valve actuation system: Design and validation of a simplified real time model. Proceedings of the Institution of Mechanical Engineers, Part E: Journal of Process Mechanical Engineering, 231(2), 212-235.

[121] "Embedded coder support package for Texas instruments", URL: https://it.mathworks.com/matlabcentral/fileexchange/43096-embedded-coder-support-package-for-texas-instruments-c2000-processors

[122] Locorotondo, E.; Corti, F.; Pugi, L.; Berzi, L.; Reatti, A.; Lutzemberger, G. Design of a Wireless Charging System for Online Battery Spectroscopy. Energies 2021, 14, 218.